Studying Lipid-Protein Interaction Using Proteinacous Supported Lipid Bilayers from Cell Membranes

A Dissertation

Presented to the Faculty of the Graduate School

of Cornell University

In Partial Fulfillment of the Requirements for the Degree of

Doctor of Philosophy

by

Chih-Yun Hsia

January 2017

Studying Lipid-Protein Interaction Using Proteinacous Supported Lipid Bilayers from Cell Membranes

Chih-Yun Hsia, Ph. D.

Cornell University 2017

Membrane proteins play important roles in cell biology and thus it is crucial to develop methods to access their functional information for further applications such as drug discovery screening or disease prevention. In order to study membrane species in their natural structure and functions, we introduce platforms using supported lipid bilayers (SLB) to house these targeted species. SLBs not only mimic natural cell membrane environments but also allow heterogeneous bilayer patterning. It is known that the cell membrane is not merely composed of a well-mixed single lipid phase, but has distinct lipid micro-domains of co-existing phases, lipid raft and liquid-disorder phase, and this feature has been suggested to play a key role in regulating several cellular activities, as some proteins have been shown to exhibit different activity levels depending on specific lipid interactions.

Therefore, we aim to determine the preference of membrane proteins with lipid raft phases, and understand the influence of lipid environment on regulating protein activity level, revealing important mechanisms of membrane proteins function in cells. Toward this goal, we first patterned two-phase coexistent SLBs inside a microfluidic to mimic membrane heterogeneities and quantify partition kinetics of membrane-bound species in this platform (Chapter 2). To further extend the platform to study membrane

protein behavior, we then developed a novel strategy to incorporate membrane proteins in SLBs without exposing them to harsh detergent to retain their native structure and functionality. In this dissertation, I will present our advances on using mammalian cell blebs (Chapter 3) and bacterial outer membrane vesicles (Chapter 4) as an intermediate to delivery membrane proteins into a SLB. A detailed characterization of bilayer properties and membrane protein functionalities will also be covered in these chapters. Finally, in Chapter 5 I will provide a broader view of how our work could be useful to study and identify the regulatory lipid-protein interactions, which is a pressing issue for a better understanding of a wide range of biological processes.

BIOGRAPHICAL SKETCH

Chih-Yun (Angela) Hsia grew up in Taipei, Taiwan. Angela joined Chemical Engineering from National Taiwan University in August 2006. After receiving her B.S degree in June 2010, she further went on to pursue a Ph.D degree at Department of Chemical and Biomolecular Engineering at Cornell University in Prof. Susan Daniel's group. Throughout her Ph.D study at Cornell, she focuses on developing an in vitro platform that mimics real cell membrane environment to study lipid-protein interactions.

I would like to dedicate this dissertation to my family, colleagues and friends for their support and help throughout these six years.

ACKNOWLEDGMENTS

First and foremost I would like to thank my supervisor, Prof. Susan Daniel and my special committees Prof. Matthew DeLisa and Prof. Barbara Baird for their guidance and assistance through my Ph.D process. I also greatly appreciate my colleagues and friends for their support and friendships: Ling Chao, Deirdre Costello, Chun-Ti Chang, Mark Richards, Donald Lee, Hung-Lun Hsu, Rohit Singh, James Xia, Han-Yuan Liu and Chelsea Hu. I thank my parents and sister for always being there for me in my life. None of these would ever be possible without them. Lastly, special thanks to Vikram Thapar for keeping me grounded throughout the time at Cornell. Grants and funding are acknowledged at the end of each chapter.

TABLE OF CONTENTS

LIST OF FIGURES

LIST OF TABLES

CHAPTER 1

LITERATURE REVIEW –TRADITIONAL AND EMERGING TECHNIQUES FOR STUDYING LIPID PROTEIN INTERACTIONS

1.1 The Cell Membrane and Lipid-Protein Interactions

The cell membrane is a fundamental biological barrier enclosing the cell cytoplasm and nucleus with the purpose of regulating the interaction between the cell and the outside environment. This membrane is comprised of a bilayer of amphipathic lipid molecules and proteins arranged to shield their hydrophobic parts from the aqueous surroundings. The membrane proteins are embedded within the lipid bilayer solvent and take part in many critical functions including transport, signaling and recognition between the cell and its environment. Not surprisingly then, over 60% of drugs on the market target membrane species[1,2]. Improving the understanding of membrane protein structure, function and dynamics is highly desired to allow for the design of more effective drugs and treatment methods[3–8]. It has recently become appreciated that not only is the protein interaction with the drug important for altering its activity or function, but that the level of modulation, or even the final biological outcome, may be coupled to the lipid interactions the protein makes with the surrounding membrane[9,10]. Beyond drug discovery, understanding of such interactions may prove critical in other biotechnology applications where membrane proteins are key elements, for example in biosensing[11], tissue engineering[12], biofilm formation[13], and so on.

An important manifestation of these interactions is the way lipids and proteins tend to separate into micro-domains through direct association among themselves instead of distributing uniformly as a homogeneous, two-dimensional fluidic environment. Micro-domains

compartmentalize distinct kinds of lipids and membrane proteins and are an important paradigm of cell membrane organization. One notable, but still enigmatic, type of micro-domain that results from phase separation is the lipid raft, which is enriched in cholesterol and sphingolipids relative to the surrounding phospholipid-rich membrane[14]. Specific kinds of proteins and glycolipids are enriched in rafts, while others are excluded. It is hypothesized that raft domains play a key role in regulating the functions of membrane proteins and their biological activities through selective partitioning of species into and out of rafts.

While phase segregation in model membranes was postulated as early as the 1980's[15,16], direct detection of lipid rafts in cell membranes has proven elusive partly because of their small scale and dynamic nature. However, there is a wealth of evidence supporting their existence. Here we provide a brief synopsis, but for a thorough review see Lingwood and Simons[17]. Detergent resistant membrane (DRM) fractionation assays isolate membrane fractions that are enriched in cholesterol, sphingomyelin, and raft-associating species[18]. Surface labeling with antibodies or toxins binding to raft-associated proteins is used to tag raft membrane domains[19]. Single particle tracking methods[20,21] detect changes in protein diffusion, which indicates the presence of more viscous raft domains. Finally, plasma membrane vesicles devoid of cytoskeletal proteins have been shown to readily undergo phase separation into large, observable raft-like and fluid-like domains[22,23]. In parallel to these techniques, recent advances in spectroscopy[24] and super-resolution imaging[25,26], such as photoactivation localization microscopy (PALM)[27], stochastic optical reconstruction microscopy (STORM)[28], and stimulated emission depletion (STED) fluorescence microscopy[29,30] have revealed dynamic, nanoscale lipid raft assemblies in living cells. Some membrane-bound species show a preference to associate with certain lipid phases in the cell membrane. Glycolipids[31], GPI-linked lipids[32] and certain proteins[33]

tend to associate with lipid rafts. Other membrane constituents, a specific example being transferrin receptor, tend to avoid lipid rafts and reside in more disordered phases enriched with phospholipids[34,35]. Studies have shown that co-existent liquid-ordered and liquid-disordered lipid phases can exist in model membrane systems[36–41], but controlling the location of these phases has been a challenge. As the lipid raft hypothesis has gained acceptance, the number of hypotheses for the mediation of cell processes through lipid-protein interactions involving rafts has increased.

Although membrane protein interactions within their local membrane environment are critical to their functions, they are not easy to probe because traditional protein characterization techniques may disrupt the native lipid-protein interaction in the cell or artifactually change the native associations. For example, detergents used in DRM fractionation can coalesce rafts and could kinetically trap non-raft species in them during this process. DRMs are also dependent on choice of detergent as different detergents may cause changes in clustering and fraction compositions[42]. Surface labeling of cells requires antibodies or toxins to bind to specific species, often crosslinking them and causing artifactual enrichment[41]. An alternative is to label fixed cells, but membrane organization and lipid-protein associations of dead cells are not necessarily indicative of live conditions[43,44]. Isotope labeling methods have some utility[45], but can only be applied to cultured cells, are expensive, and still require isolation methods to identify residents.

Therefore, to expand our current knowledge of how membrane proteins function and are regulated, a variety of techniques including novel membrane platforms are needed to improve characterization of lipid-protein interactions and minimize possible artifacts.

1.2 The Principles of lipid-protein interactions

Lipid species interacting with membrane proteins can be classified into two categories: annular lipids and non-annular lipids.4 Annular lipids solvate membrane proteins by forming a shell around their surfaces (Fig. 1A), while non-annular lipids are found buried within protein helices (or protein complex subunits) forming lipid–protein complexes (Fig. 1B). The critical differences between annular and non-annular lipids are their degrees of affinity for, and their residence times with, membrane proteins. Annular lipids exhibit lower affinity to membrane proteins compared to non-annular lipids and possess the motional freedom to exchange with the bulk environment; in contrast, non-annular lipids are more restricted from exchanging with the surrounding lipids and may bind directly to specific sites on membrane proteins. The following sub-section will expand on the principles of annular and non- annular lipid–protein interactions and provide biological examples of each type.

1.2.1 Annular lipid–protein interactions.

The effects of annular lipids on membrane protein structure and their functions are mainly ruled by the following interaction principles[9]: (1) The degree of hydrophobic matching between membrane protein core and the surrounding lipid acyl chains. (2) The structure and charge distribution of lipid headgroups and protein amino acid residues located near the lipid–water interface. To avoid exposing the hydrophobic domain of membrane proteins to aqueous solution, the hydrophobic thicknesses of lipid bilayers and proteins must match. Mismatching results in the distortion of protein structures, which can influence their functions. One well-known example is the mechanosensitive channel of large conductance (MscL) from *Escherichia coli*. Hydrophobic matching is controlled by a shift in bilayer thickness (via acyl chain length), which results in a distinct MscL conformational change and its gating function: a thin bilayer

favors channel opening while thick bilayer favors a closed structure.35 Another important effect of hydrophobic matching is to sort/cluster membrane proteins into specific domains. Hydrophobic matching between SNARE protein transmembrane domains and surrounding bilayers is mediated by cholesterol and is believed to cluster SNARE proteins into thicker raft domains[36]. The headgroup region of annular lipids also has important influence on membrane protein conformation and activity. Hydrogen bonding and charge–charge interaction between the specific amino acids of proteins and lipid headgroups can largely affect the structure of the protein. A clear case is in rhodopsin photoactivation[46]. Phosphatidylethanolamine lipids (PEs) were found to interact tightly with rhodopsin and promote the formation of MII, a major intermediate of the rhodopsin photocycle. One of the possible mechanisms to explain the observation is the formation of hydrogen bonds between the PE headgroups and Glu-134, which is exposed upon MII formation.38 Other studies also detected "hotspots" on membrane proteins for binding by anionic lipids due to their electrostatic interactions[4,39]. An example is the characterization of a subset of annular lipids around ABC transporters[47], where negatively charged phosphatidylglycerol lipids (PGs) were demonstrated to exhibit higher affinity toward TmrAB dimer than zwitterionic PEs.

1.2.2 Non-annular lipid–protein interactions.

Lipids exerting higher affinity to specific binding sites on protein trans- membrane domains are referred to as non-annular lipids. These lipids may be integrated within the protein core structure, especially between protein subunits. Due to their high-affinity binding to membrane proteins, non-annular lipids can be resolved in membrane protein crystal structures by high-resolution crystallography, and many examples of non-annular lipid–protein interactions have been

reviewed in literature[48,49]. Non-annular lipids serve diverse purposes in modulating protein structure and function on cell membranes. For instance, lipids can act as co-factors for membrane proteins to function, and a typical example is the potassium channel KcsA[50]. Anionic phospholipids, such as PGs, were found to bind at the monomer–monomer interface in the KcsA homotetramer. It is believed that the interaction of PGs with the non-annular binding sites of KcsA helps the packing of KcsA structure and supports its conducting state. Another well-known function of non-annular lipids is their allosteric effect in regulating membrane protein activities. For example, binding between cholesterol and many G-protein- coupled receptor (GPCR) allosteric sites were found to be critical to GPCRs biological pathways, such as the full activation of the oxytocin receptor[51] and the ligand binding and G-protein coupling of serotonin1A receptor[52]. A second example of regulation comes from protein interaction with the acyl tails, in particular, the influence of the flexibility of chain conformations. These have been shown to mediate annular lipid/protein interactions, such as between polyunsaturated lipids and GPCRs.46–48 Finally, non-annular lipid–protein interactions have been suggested to play a role in targeting proteins to distinct lipid domains. For example, binding between the metabotropic glutamate receptor (a type of GPCR found in Drosophila melanogaster) and cholesterol was shown to target the receptor to lipid rafts.49 In another example, binding of amyloid precursor protein (APP) and cholesterol has been suggested to promote localization of APP in lipid rafts, and the association of APP to lipid rafts is believed to be essential to the progression of Alzheimer's disease.

A primary objective of raft investigations is often to determine which species are targeted to raft domains and how species are targeted to raft domains. Specific structures of membrane species have been found to dictate their raft-association preferences[53]. For instance, it was found

that differences in the structure of glycophosphatidylinositide (GPI) anchors could be correlated to the differences in raft-association of GPI-linked proteins[34]. Diaz-Rohrer et al. further explored this concept[54]. They devised an array of protein constructs based around a single pass protein, trLAT, with variations in transmembrane domain lengths and sequences as well as number of palmitoylation sites. By observing the trafficking behavior of these fluorescent fusion protein constructs in cell membranes and the raft partitioning behavior in model giant unilamellar vesicles, they proposed a unique raft pathway whereby raft-associated proteins are recycled to the plasma membrane. It is important to note that the labeling strategies used in experiments can potentially influence the interactions between lipids and proteins and the dynamics and stability of membrane domains, so careful controls must be performed to understand and minimize the effects of labels used. For instance, antibody labeling can crosslink species and cause of stabilization of domains[21].

Another objective of raft investigations is to determine how raft environments can affect protein function. Many of these studies use disruption of rafts in live cells to evaluate their influence on protein function, that is, to observe differences in protein function before and after raft disruption. Rafts can be disrupted by either removal of cholesterol using cyclodextrins or using knockouts of sphingolipid biosynthesis enzymes. Depletion of cholesterol by cyclodextrin has been shown to reduce levels of raft marker proteins in detergent resistant membrane fractions. Disruption methods also revealed stimulation of signaling through the tyrosine phosphorylation and Ras-ERK pathways, promoting the idea that raft-association regulates protein activity (particularly LCK) in these cascades[55]. Although cyclodextrins are useful tools to deplete cholesterol, their mechanisms of action are still unclear and may promote raft formation instead of eliminating them[56], may remove cholesterol from raft and non-raft domains at different

rates, and, at high enough concentrations, may extract other molecules including phospholipids from the membrane[57].

In another study of cell migration induced through the CXCR4/CXCL12 pathway, sphingomyelin was shown to play an important role. By knocking out sphinogmyelin synthases, it was concluded that sphingomyelin acts as a selective regulator of GPCR signaling; low sphingomyelin concentration in rafts leads to an increase in CXCR4 levels in rafts and increased dimerization, both correlating to increased cell migration[58]. Although the strategy of genetically deleting an individual enzyme targets the lipid-protein interaction directly, it is important to note that there will also be changes in all lipids "downstream" of that enzyme in the pathway, which can also impact other potentially related cellular functions.

A third objective of raft investigations is to characterize the dynamics of biomolecules partitioning into and out of rafts within the membrane plane. Biomolecules move laterally within the lipid bilayer by Brownian diffusion[59]. With the advent of single molecule microscopy techniques to track individual proteins embedded in cell plasma membranes, it has been revealed that protein diffusion is strongly influenced by partitioning into raft domains as well as by interactions with other membrane species, particularly those immobilized by the cytoskeleton. Such studies have highlighted the interplay between cytoskeleton and lipid rafts in guiding cellular control of membrane species distribution[60]. Because of the tight coupling between rafts and the cytoskeleton, separating the impact of these two structures in whole cells is difficult[61,62].

Several models for the complex diffusion of membrane proteins among domains and cytoskeletal corrals have been developed and evaluated using single molecule tracking (SMT) techniques in cells. Kusumi's hop-diffusion compartmentalization model claims that molecular "fences" formed by cytoskeletal elements and bound membrane protein "pickets" help to

organize the plasma membrane into patches with free diffusion within a confinement patch, and occasional hops between patches[63,64]. Weigel et al. analyzed Kv2.1 protein tracking, with GFP and quantum dot labeling, to determine the diffusion process is non-random such that certain regions of the membrane are more likely to be sampled by the membrane protein and proposed a model of a random walk on a fractal[65]. By disrupting actin with depolymerization drugs, they were able to see random diffusion, indicating Kv2.1 binding to actin plays a key role in its diffusional behavior. In another SMT study, Türkcan et al. used a Bayesian inference scheme to characterize hopping events of ε-toxin receptor (labeled with fluorescent nanoparticles) between raft domains, where they found that hopping between raft domains was limited by the proximity of adjacent domains[66]. After destabilization of rafts with sphingomyelinase or cholesterol oxidase, diffusivity of ε-toxin receptor increases and confinement decreases, indicating the influence of rafts on ε-toxin receptor diffusion.

While SMT studies have provided a wealth of new knowledge about protein behavior in cell membranes, it is important to recognize that not all protein clustering and domain formation involves lipid rafts. Other domains can form as a result of protein-protein interactions without typical raft constituents[67,68]. All of this work suggests a complex interplay of lipid-protein and protein-protein driving forces for lateral membrane organization. Decoupling this complexity to conclusively identify and distinguish protein-protein from lipid-protein interactions and characterize their mechanisms of action is an impetus to use reduced models of membranes in model membrane platforms.

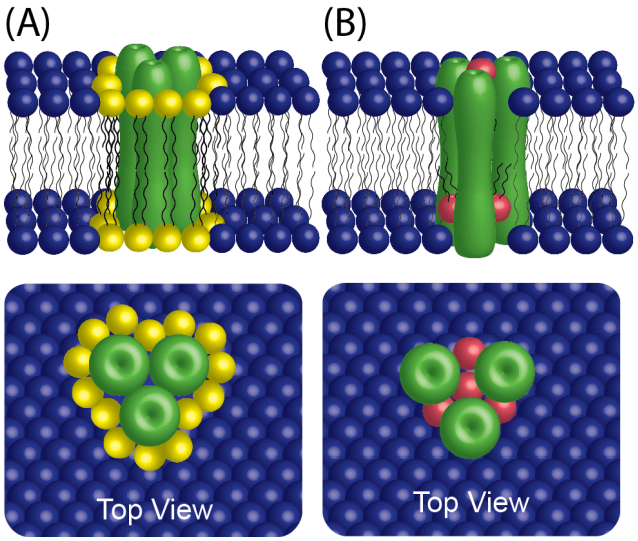

Figure 1.1. Annular vs. Non-Annular lipid protein interaction. (A) Annular lipid arrangement (yellow) around a protein complex (green). (B) Non-annular lipids (pink) arranged within a multi-subunit protein complex. The surrounding lipids (in blue) represent non-raft membranes enriched in phospholipids.

1.3 Approaches for identifying and characterizing lipid-protein interactions

1.3.1 Structural characterization of protein-lipid complexes/interfaces

Membrane protein structures, and particularly lipid–protein interaction sites, provide significant insights into how lipid–protein interactions might impact function. Among structural characterization tools, crystallization is the standard method that analyzes lipid–protein complex structures with atomic level resolution. X-ray crystallography (XRC) has been used extensively for defining the structure of three-dimensional lipid–protein complexes and recognizing lipid–protein binding sites (recently reviewed in Shi, 2014).[69] For example, cholesterol has been observed in crystal structures of the b2-adrenergic receptor by using XRC.[70,71] However, to achieve high-resolution structural information, high quality protein–lipid complex crystals are needed, which makes crystallization a critical step for successful XRC performance. The traditional method (*in surfo* method) to crystallize protein–lipid complexes requires the use of

surfactants (detergents) to solubilize protein–lipid complexes from the native bilayer environment and form detergent–protein–lipid micelles. Membrane proteins may be denatured during this process and lipids bound to the protein–lipid assembles may be replaced by detergent molecules. As an alternative, *in meso* methods have been developed in the past decade to overcome this limitation (recently reviewed in Caffrey et al., 2012)[72]. The *in meso* methods crystallize protein–lipid assembles in lipidic mesophases, which preserves assembled protein–lipid structures and reflects more realistic lipid–protein interactions. This method has been especially useful in determining structures for G protein- coupled receptors, with 55 distinct GPCR structures crystallized and resolved by the in meso method[73]. Two-dimensional electron crystallography resolves 2D protein crystal structures in lipid bilayers, where proteins are purified, reconstituted and crystallized in a lipid bilayer environment (recently reviewed in Wisedchaisri et al., 2011)[74]. The resolution achieved by electron crystallography is now comparable with XRC. For example, a 1.9 ˚ A resolution structure was successfully determined for aquaporin and its annular lipids[75]. In addition, electron crystallography has been able to reveal membrane protein structures that were not solved by 3D XRC. For example, the conformational change resulting from ligand binding to cyclic nucleotide-modulated potassium channel, MloK1, was recently reported using 2D electron crystallography[76]. With both techniques now having comparable resolutions, a distinct advantage of electron crystallography over XRC is the lower amounts of proteins required, which is critical for membrane proteins with typical low yields due to expression limitations and purification processes[77]. Although crystallization is a powerful method of resolving lipid–protein complex structure, membrane proteins do not readily crystallize, consequently few protein–lipid complexes have been solved. As of February 2015, membrane proteins (1604 entries, retrieved from

http://blanco.biomol.uci.edu/ mpstruc/) only account for 1–2% of all the protein structures (99147 entries) released in the protein data bank (PDB)[78]. As an alternative approach, nuclear magnetic resonance (NMR) can be used to obtain protein–lipid structural information, but with molecular-scale resolution. NMR has rapidly improved from the traditional solution NMR, which was limited to small molecules (<40 kDa) in solution, to solid-state NMR. Solid-state NMR has the ability to examine macromolecule structure (>100 kDa), such as purified proteins reconstituted into lipid bilayers. Thus NMR is now routinely used to determine lipid–protein complex structures (reviewed in Tycko, 2001 and Huster, 2014)[79,80]. For example, the non-annular binding sites of the potassium channel KcsA and anionic phospholipids were also well-characterized by solid- state NMR[50], corroborating results of the previous X-ray crystallography study[81]. Despite the ability to resolve structures with high resolution, the structural characterization tools stated above cannot often capture the fast dynamics of lipid–protein interactions. For instance, annular lipids are highly dynamic and interact with the surrounding bulk lipid bilayer at the rate of 10^{-7} s^{-1}.[82] Moreover, the complexity of lipid–protein environment makes it challenging to study lipid–protein interactions with high time resolution. Other techniques like electron paramagnetic reso- nance (EPR) spectroscopy and 2D infrared (2DIR) spectroscopy can better capture the dynamics of lipid–protein interactions (recently reviewed in Smith, 2012)[83]. EPR has the potential to probe protein–lipid interfaces with high sensitivity and fast timescales (nanosecond to microsecond). This temporal resolution permits characterization of the dynamics of the annular lipid shell surrounding membrane proteins and thus the residence time of lipid–protein complexes[84]. Speed and sensitivity are also advantages of 2D IR spectroscopy. By probing electronic and vibrational dynamics at the time scale of femtosecond to picosecond,[85] researchers are able to measure the strength of lipid–protein interactions and define

the orientation and conformation of proteins in lipid bilayers.[86,87] Besides probing specific interactions at the molecular level, the characterization of structural motifs of lipid–protein complexes, such as between proteins and lipid raft domains, can provide insight on biological function. Structural characterization of raft lipids (sphingolipids and cholesterol) bound to proteins has provided significant insights on: (1) how these proteins may be targeted to rafts, and (2) how their conformation, function, and interactions with other species are influenced by interaction with raft lipids. For example, evidence supports that influenza virus proteins (hemagglutinin, neuraminidase, M2) associate with lipid rafts of host cells as a way to organize prior to budding to form viral progeny.[88] Both crystallographic and NMR studies have clarified the M2 protein structure and its cholesterol-binding domains.[89,90] From these studies, M2 protein is believed to be raft-anchored through its binding with cholesterol and localizes at the edge of the bud zone to carry out a crucial role in mediating the particle scission process.[91]

In summary, structural characterization tools receive much attention owing to their capacity to determine lipid–protein complex structure with high resolution, detect the dynamics of lipid–protein interactions, and probe the role of lipid rafts son protein conformation and function. However, these techniques are low throughput and the sample preparation techniques are often difficult and can give rise to artifacts. To develop a more complete picture, cell-based studies are also needed to complement structural information.

1.3.2 Cell-Based Techniques to Study Lipid-Protein Interactions and Raft Function

A primary objective of raft investigations is often to determine which species are targeted to raft domains and how species are targeted to raft domains. Specific structures of membrane species have been found to dictate their raft-association preferences[53]. For instance, it was found

that differences in the structure of glycophosphatidylinositide (GPI) anchors could be correlated to the differences in raft-association of GPI-linked proteins[34]. Diaz-Rohrer et al. further explored this concept[54]. They devised an array of protein constructs based around a single pass protein, trLAT, with variations in transmembrane domain lengths and sequences as well as number of palmitoylation sites. By observing the trafficking behavior of these fluorescent fusion protein constructs in cell membranes and the raft partitioning behavior in model giant unilamellar vesicles, they proposed a unique raft pathway whereby raft-associated proteins are recycled to the plasma membrane. It is important to note that the labeling strategies used in experiments can potentially influence the interactions between lipids and proteins and the dynamics and stability of membrane domains, so careful controls must be performed to understand and minimize the effects of labels used. For instance, antibody labeling can crosslink species and cause of stabilization of domains[21].

Another objective of raft investigations is to determine how raft environments can affect protein function. Many of these studies use disruption of rafts in live cells to evaluate their influence on protein function, that is, to observe differences in protein function before and after raft disruption. Rafts can be disrupted by either removal of cholesterol using cyclodextrins or using knockouts of sphingolipid biosynthesis enzymes. Depletion of cholesterol by cyclodextrin has been shown to reduce levels of raft marker proteins in detergent resistant membrane fractions. Disruption methods also revealed stimulation of signaling through the tyrosine phosphorylation and Ras-ERK pathways, promoting the idea that raft-association regulates protein activity (particularly LCK) in these cascades[55]. Although cyclodextrins are useful tools to deplete cholesterol, their mechanisms of action are still unclear and may promote raft formation instead of eliminating them[56], may remove cholesterol from raft and non-raft domains at different

rates, and, at high enough concentrations, may extract other molecules including phospholipids from the membrane[57].

In another study of cell migration induced through the CXCR4/CXCL12 pathway, sphingomyelin was shown to play an important role. By knocking out sphinogmyelin synthases, it was concluded that sphingomyelin acts as a selective regulator of GPCR signaling; low sphingomyelin concentration in rafts leads to an increase in CXCR4 levels in rafts and increased dimerization, both correlating to increased cell migration[58]. Although the strategy of genetically deleting an individual enzyme targets the lipid-protein interaction directly, it is important to note that there will also be changes in all lipids "downstream" of that enzyme in the pathway, which can also impact other potentially related cellular functions.

A third objective of raft investigations is to characterize the dynamics of biomolecules partitioning into and out of rafts within the membrane plane. Biomolecules move laterally within the lipid bilayer by Brownian diffusion[59]. With the advent of single molecule microscopy techniques to track individual proteins embedded in cell plasma membranes, it has been revealed that protein diffusion is strongly influenced by partitioning into raft domains as well as by interactions with other membrane species, particularly those immobilized by the cytoskeleton. Such studies have highlighted the interplay between cytoskeleton and lipid rafts in guiding cellular control of membrane species distribution[60]. Because of the tight coupling between rafts and the cytoskeleton, separating the impact of these two structures in whole cells is difficult[61,62].

Several models for the complex diffusion of membrane proteins among domains and cytoskeletal corrals have been developed and evaluated using single molecule tracking (SMT) techniques in cells. Kusumi's hop-diffusion compartmentalization model claims that molecular "fences" formed by cytoskeletal elements and bound membrane protein "pickets" help to

organize the plasma membrane into patches with free diffusion within a confinement patch, and occasional hops between patches[63,64]. Weigel et al. analyzed Kv2.1 protein tracking, with GFP and quantum dot labeling, to determine the diffusion process is non-random such that certain regions of the membrane are more likely to be sampled by the membrane protein and proposed a model of a random walk on a fractal[65]. By disrupting actin with depolymerization drugs, they were able to see random diffusion, indicating Kv2.1 binding to actin plays a key role in its diffusional behavior. In another SMT study, Türkcan et al. used a Bayesian inference scheme to characterize hopping events of ε-toxin receptor (labeled with fluorescent nanoparticles) between raft domains, where they found that hopping between raft domains was limited by the proximity of adjacent domains[66]. After destabilization of rafts with sphingomyelinase or cholesterol oxidase, diffusivity of ε-toxin receptor increases and confinement decreases, indicating the influence of rafts on ε-toxin receptor diffusion.

While SMT studies have provided a wealth of new knowledge about protein behavior in cell membranes, it is important to recognize that not all protein clustering and domain formation involves lipid rafts. Other domains can form as a result of protein-protein interactions without typical raft constituents[67,68]. All of this work suggests a complex interplay of lipid-protein and protein-protein driving forces for lateral membrane organization. Decoupling this complexity to conclusively identify and distinguish protein-protein from lipid-protein interactions and characterize their mechanisms of action is an impetus to use reduced models of membranes in model membrane platforms.

1.3.3 Traditional and emerging model membrane techniques to study lipid rafts.

Model membrane methods for probing membrane protein activity in lipid environments aim to bridge the approaches of traditional proteomics and cell-based assays. Cellular processes

are entangled and individual factor effects are difficult to isolate. This cell complexity is the motivation for the development and use of biomimetic membrane strategies to model and deconstruct cell membrane processes. Model systems are simplified and tunable, helping to visualize organization and dynamics of membrane species and assay activities of individual components, oftentimes using many of the aforementioned microscopy techniques. In the minimal model approach, these systems contain known lipid and protein components and can be used to isolate and assay behavior of individual species. At the other end of the spectrum, incorporation of cell extracts, including cell membrane-derived vesicles (blebs), combines the beneficial techniques for imaging and assaying model membrane systems with the increased complexity and biological relevance of species studied. The two most commonly used model membrane systems that will be reviewed here are vesicles and solid supported lipid bilayers (SLBs). Less common systems, such as nanodiscs, fluorinated surfactants, and amphiphols are reviewed by Popot[92].

1.3.3.1 Vesicle-Based Model Membrane Studies

Giant unilamellar vesicles (GUVs) and giant plasma membrane vesicles (GPMVs) are the major vesicle-based model membrane systems. A range of biomolecule complexity can be spanned by these systems from simple, few-component lipid GUVs, to reconstituted proteoliposomes[93], to cell-extracted GPMVs[94]. GUVs are reconstituted lipid systems formed from minimal components. These reconstituted vesicle systems have been crucial for the characterization of phase behavior of lipid mixtures and phase segregation of probes and membrane protein components[54,95–100]. GUVs were used to show that cross-linking of GM_1 glycolipids in membranes led to large-scale membrane phase separation[101], for example.

GPMVs formed from cell plasma membranes contain native lipids and proteins and therefore capture more biological complexity than GUVs. GPMVs generally display a single lipid phase until temperatures are lowered below the critical point where two phases form and protein partitioning occurs[95,102]. These studies reveal that the cell membrane is near a miscibility critical point. Thus perturbations, such as local composition fluctuations, can cause changes in miscibility and may serve as a means to control raft formation and protein partitioning in the cell membrane. Levental et al. showed that GPMVs of various preparations contained a variety of phases with different properties and compositions reflecting complexity of domains that are possible in cells[103].

Vesicle systems are advantageous because they can easily incorporate mobile integral membrane proteins[104,105]. Because of their spherical geometry, vesicles contain an isolated lumen making them great systems for also evaluating function of transport proteins like ion channels[106–108]. Vesicle systems have been used to study protein function in presence of specific lipids and ligands. Two particular studies generated GUVs with a wide variety of lipid compositions to determine which species can alter protein function. In the first study, β-secretase or BACE, a membrane spanning protease, was shown to have its activity most strongly affected by anionic lipids, but also to some extent by glycosphingolipids and cholesterol[109]. The enhancement of activity by classical raft lipids fits the idea that BACE activity is enhanced in rafts where it is able to interact with its substrate, the amyloid precursor protein[110]. In a second study, the activity of placental alkaline phosphatase (PLAP), a GPI-linked protein, was shown to decrease in the presence of cholesterol and lipid rafts[111]. Since PLAP, like many GPI proteins, is known to be associated with rafts[112], this response follows a repressive regulation of activity in the presence of rafts, as has also been observed for some other GPI proteins[113].

Because vesicles have a fragile, three-dimensional structure, many surface techniques cannot be used and quantitative imaging often requires confocal or other more sophisticated techniques. In these systems, phase separation and protein partitioning occur at the same time, so the kinetics of protein partitioning cannot be monitored easily; usually these systems are used to monitor distributions at equilibrium conditions. However, phase separation in vesicles cannot be spatially controlled, so labels are needed to indicate phase and protein locations.

1.3.3.2 Supported Lipid Bilayer-Based Model Membrane Studies

Supported lipid bilayers consist of a solid surface onto which a lipid bilayer is adsorbed typically via a vesicle fusion[114] or Langmuir–Blodgett–Schaeffer transfer technique[115]. The SLB provides a chemically tunable, planar platform that is compatible with a vast array of surface characterization tools, such as total internal reflection fuorescence microscopy (TIRFM),[116] atomic force microscopy (AFM),[117] quartz crystal microbalance (QCM),[118,119] and surface plasmon resonance (SPR),[120–122] among many others. Like vesicle systems, SLBs span the full range of complexity from simple lipid-only platforms to the complex chemistries of cell plasma membrane bilayers.

One drawback of SLB systems is the close proximity of the bilayer to the support that effectively reduces the diffusion of membrane species,[123–125] relative to free-standing or vesicle bilayers. This drawback becomes more pronounced when attempting to reconstitute fully functional mobile membrane proteins in SLBs. In a typical phosphatidylcholine (PC) SLB on glass there is a ~1 nm water gap between the bottom leaflet and the glass surface[126] that is too small to accommodate most soluble domains of membrane proteins, which can extend up to 10 nm.[127] Strong interaction with the solid support often leads to immobilization of membrane

proteins. To solve these problems, various bilayer cushioning or tethering strategies have been proposed that extend the distance between the bilayer and the support.[128–131] One particular strategy that is relatively easy to incorporate and shows improved membrane protein mobility is the double cushion strategy.[132,133] The first cushion is created by adsorbing a passivating layer of proteins (typically bovine serum albumin) to the glass support to reduce non-specific binding. The second cushion is composed of polyethylene glycol (PEG) polymer functionalized lipids interspersed in the bilayer.[134–136] The extension length of the polymer cushion can be controlled by selecting the PEG chain length and the concentration in the bilayer.[137,138] Unfortunately, although cushioning and tethering techniques show improvement over uncushioned systems, many of these strategies still result in less than half of proteins showing any significant mobility, necessitating further investigations of cushioning and fluidization of membrane proteins by these polymers and integrating what is learned into next generation spacing strategies. In particular, it is unclear if the PEG polymers can provide a uniformly cushioned bilayer that can protect the incorporated membrane proteins or if cushioned and uncushioned domains will form.[132,139] An additional concern is that at high grafting densities, PEG cushioning can provide a steric barrier preventing access for ligands to the membrane proteins.[140–142] Because of these limitations, most SLB investigations have been restricted to peripheral proteins, small self-inserting proteins, or proteins without domains that extend towards the support. The flat geometry of a SLB favors using quantitative techniques to characterize important aspects of lipid–protein and protein–protein interactions. For instance, a SLB-based single molecule tracking study tracked 17 different peripheral protein–lipid complexes to find that the drag effects on peripheral membrane proteins depended strongly on bound lipids and extent of penetration of protein domains into the bilayer.[143] Another study used high-speed AFM to track OmpF protein trimers in a supported

lipid bilayer at sub-500 ms resolution.[144] With this method it was possible to determine the orientation of trimers and show that interactions between proteins are crucial to the formation of slow, stable assemblies. Deverall used SMT in a tethered SLB to study effects of obstacles on bacteriorhodopsin protein diffusion.[125] Tethers consisted of individual lipids attached to underlying polymer, effectively immobilizing lipid molecules in the bilayer. The impact of tether density on protein diffusion was investigated, showing similarities to the observed effect of the cytoskeleton in cells on protein diffusion, and followed a model of obstructed diffusion. While these studies show that SLBs are promising mimics for cell membranes, two major challenges are associated with extending their usefulness to studying myriad membrane proteins: (1) incorporating membrane proteins into the SLBs with their native cell membrane lipid associations, and (2) minimizing interactions between the extramembranous regions of the proteins and the underlying glass support. In this thesis, we have developed an alternative method that tackles these issues, that is to deliver membrane proteins to the supported bilayer platform via 1) mammalian cell blebs fusion or 2) bacterial outer membrane vesicles (OMVs) fusion. Detailed descriptions of the procedures of developing such platforms are presented in Chapter 3 and Chapter 4.

1.3.3.3. Measuring biomolecule partitioning in model membrane systems.

Existing methods to probe raft partitioning in intact cells (DRMs and cholesterol depletion with cyclodextrins) described above are fraught with complications and possible artifacts. Additionally, many methods, including GUV partitioning studies[145] are equilibrium measurements and cannot provide information regarding the dynamics of partitioning. The standard approach for studying rafts in GUVs and SLBs has been to use the canonical raft

mixture, a composition of lipids that will spontaneously separate into raft-like ordered and non-raft disordered lipid phases,[146–148] e.g., point 0 on the tie line in Fig. 1.2A. This approach results in random distribution of phases in the bilayer and requires tags to locate phases (Fig. 1.2B). Due to the nature of how GUVs are formed, once phase separation occurs, species have already distributed between the phases so kinetic information about the partitioning process cannot be obtained. To circumvent some of these complications, we designed a SLB platform to investigate raft partitioning of membrane species that takes advantage of the unique ability to selectively pattern SLBs.

1.3.3.4. Emergence of patterned SLBs to model raft partitioning.

An advantage of supported lipid bilayers is that they can be patterned to create arrays of bilayer domains of varied composition or separate bilayers into distinct isolated patches.[149–151] The four main patterning techniques are polymer mold based stamping or blotting,[152–154] polymer dry lift-off stenciling,[155,156] UV-photopatterning[151] and laminar flow patterning.[157–159] To generate different geometries of liquid-ordered/liquid-disordered bilayers, we have used the blotting method (Fig. 1.2C) and laminar flow patterning (Fig. 1.2D). These patterned bilayers serve as model raft membranes that can be used to study the partitioning of biomolecules to/from these domains. Our lab focuses on using laminar flow patterning to develop two-phase coexistent SLBs in microfluidic channel, which we have successfully used to quantify partitioning kinetics of membrane glycolipids. The study will be presented in Chapter 2.

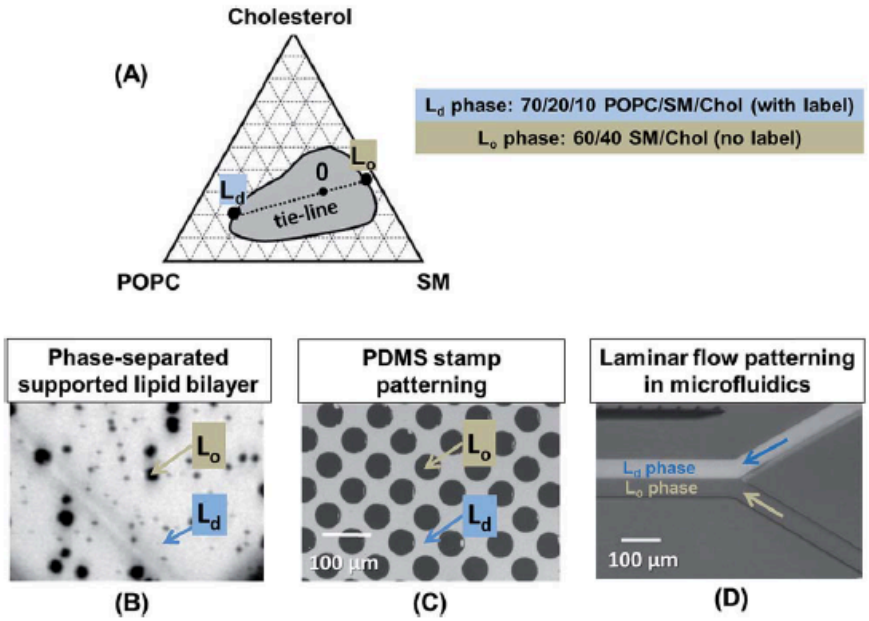

Fig. 1.2 (A) Ternary phase diagram for the 1-palmitoyl-2-oleoyl-snglycero-3-phosphocholine POPC, sphingomyelin (SM), and cholesterol system. The gray area represents the two-phase coexistence zone. The tie line (dashed) runs through point 0, which spontaneously phase separates into two phases, each given by the compositions at the end of the tie line and denoted as ld (liquid-disordered) and lo (liquid-ordered). (B) A lipid mixture of composition 0 phase separates into a random pattern after formed into a supported bilayer. Both position and size of the domains are variable. (C) Patterning a SLB using PDMS stamping where two separate lipid phases are used (each at the ends of the tie line) to create regularly patterned domains of lo phase within the continuous ld phase. (D) Patterning a SLB using laminar flow in a microfluidic device results in a striped pattern of lo/ld phases along the channel.

1.3.3.5. Capturing more complexity of the plasma membrane in model systems.

It is important to be mindful that model systems do not represent the full complexity of the cell membrane, and strive to strike a balance between simplicity and necessary complexity. One important and sometimes overlooked aspect is membrane asymmetry. While model systems typically employ symmetric bilayers, i.e. bilayers with the same compositions of lipids in each leaflet, the cell plasma membrane is asymmetric and traditional cholesterol and sphingolipid enriched rafts are only believed to exist in the extracellular leaflet.[148,160] Signal transduction across leaflets through registration of domains is a topic of considerable interest in the community.[161–163] Asymmetric leaflets can be constructed in SLBs by using a Langmuir–Blodgett and Langmuir–Schaefer transfer process with different compositions in each leaflet. When a sufficiently long enough polymer tether was used between the lower leaflet and the glass,

domain registration would occur since the influence of the substrate could be minimized.[164] Interestingly, compositions that would not normally phase separate can be induced to form registered domains by raft-like domains in the other leaflet. Applying asymmetric raft model membranes to protein partitioning, Hussain et al. investigated integrin partitioning. 156 Integrin partitioning into rafts was detected by colocalization with NBD probes, and exhibited a partitioning preference for asymmetric rafts but not symmetric rafs.[165] This behavior could be due to differences in hydrophobic thickness between asymmetric and symmetric raft domains. This work highlights the need to consider the importance of asymmetry in these SLB systems to better mimic the true cellular physiology. However, care must be taken when working with asymmetric bilayers in model systems as the lipids can flip–flop between leaflets with a half-time of ~15 h,[161] but may be much shorter in the presence of proteins,[166] or small defects (holes) in planar bilayers,[167] or at temperatures approaching the lipid transition temperature.[168] Another key aspect of cell membranes often overlooked in model systems are the supporting structures adjacent to the cell membrane, like the cytoskeleton and glycocalyx, and the roles they may play on domain formation. Moving toward this direction, patterned glycans were used to influence phase separation in supported bilayers.[169] In this work glycans were patterned on supports uniformly or patch-wise (heterogeneously) upon which multi-component lipid vesicles fused to form supported bilayers. Depending on the underlying glycan pattern (and temperature of the system) multiple lipid phases can form within the SLB. This work highlights the need to not only understand the influence of the components within the membrane on phase separation and raft formation, but also the effect of the glycocalyx and extracellular parts on membrane organization.

1.5 ACKNOWLEDGEMENTS

This chapter was published as “A review of traditional and emerging methods to characterize lipid-protein interactions in biological membranes” in Analytical Methods[170]. Chih-Yun Hsia and Mark J. Richards were co-first authors with co-author Susan Daniel. We thank the National Science Foundation ((EEC-0824381, CBET-1149452, CBET-1263701) for supporting some of the work presented in this chapter. Some of the work presented herein was performed at the Cornell NanoScale Facility, which is supported by the NSF (ECS-0335765).

CHAPTER 2

DEVELOPMENT OF TWO-PHASE PATTERED SUPPORTED LIPID BILAYERS TO STUDY BIOMOLECULES PARTITIONING AND TRANSPORT BEHAVIORS

2.1 INTRODUCTION

Membrane proteins and glycolipids are targets for therapeutic development[1], but processing membrane-bound species while maintaining intact structural information, proper orientation, and necessary lipid associations remains a large bottleneck to characterizing and understanding their structure-function behavior[171,172]. The problem stems from the requirement of protecting the hydrophobic regions from water during processing. Many purification strategies use denaturing chemicals or conditions to remove species from the membrane and then use techniques developed mainly for soluble species to isolate them[173,174]. This approach can cause denaturation (in the case of proteins), disrupt orientational order necessary for binding to soluble species, and interrupt critical lipid associations (e.g. lipid microdomains) that are important for function[175,176]. Therefore, additional steps are required to restore the native, active structures and lipid associations. New strategies for separating membrane species in a native-like environment (i.e., a lipid bilayer) near physiological conditions would be attractive alternatives for this class of biomolecules.

A supported lipid bilayer (SLB) platform can protect the hydrophobic regions of membrane species. SLBs are chemically tunable and maintain the mobility of the species residing within them, including lipids[177], glycolipids[178], lipid-linked proteins[179], and even some

transmembrane species[130,133,180]. The planar geometry of SLBs facilitates the integration of surface analytical techniques that can be used to monitor lipid-lipid, protein-protein, or lipid-protein interactions, such as fluorescence microscopy[36,181], ellipsometry[182], and atomic force microscopy[37,38,183,184].

Previous studies demonstrate the separation of membrane-bound biomolecules supported lipid bilayers using electrophoresis[177,185–188], bilayer self-spreading[189], or bulk hydrodynamic drag[190,191]. However, these studies used SLBs of homogeneous chemical composition as the separation medium, so the separation was based solely on differences in biomolecule charge and/or mobility through the bilayer medium. None of these strategies separate species based on their affinity for a specific lipid chemistry/environment.

Herein, we describe a planar (2-D) extraction platform that uses a two-phase coexistent SLB to separate membrane species based on their different chemical affinities for chemically-distinct phases in the bilayer. This strategy is suited to this class of biomolecules because of the natural tendency of membrane-bound species to associate with different lipid phases in the cell membrane, such as glycolipids[31], GPI-linked lipids[192] and certain proteins[33]. These species tend to associate with lipid microdomains known as lipid rafts. Other membrane constituents tend to avoid lipid rafts and reside in more disordered phases enriched with phospholipids[34]. We exploit this natural partitioning tendency to carry out a two-dimensional extraction process in a planar SLB platform.

To do so, different phases in the SLB (i.e. membrane heterogeneity) must be constructed and patterned in a useful geometrical shape that facilitates the physical separation and sorting of species. Many studies have shown that co-existent liquid-ordered and liquid-disordered lipid phases can exist in model membrane systems[36–41], but controlling the location of these phases

has been a challenge. Here in this chapter, we describe a way to pattern stable phases in an SLB using laminar flow in a microfluidic device to perform 2-D extractions in planer membrane. We then further focus on 1) studying the partitioning kinetics of membrane-bound species and 2) developing a transport model in a heterogeneous SLB platform to better optimize the separation/sorting performance of such extraction device.

2.2 EXPERIMENTAL SECTION

A detailed list of materials and methods used in this study is provided in Appendix A: Fluorescence Microscopy, Preparation of Lipid Vesicles for Formation of Supported Lipid Bilayers, PDMS Well Fabrication, Characterization of Diffusion in Supported Lipid Bilayers by Flurescence Recovery After Photobleaching (FRAP) and Preparation of glass coverslips used as supports for supported bilayers.

2.2.1 Materials

1-Palmitoyl-2-oleoyl-sn-glycero-3-phosphocholine (POPC), DOPC (1,2-dioleoyl-*sn*-glycero-3-phosphocholine), Ovine wool cholesterol (Chol), 16:0 N-palmitoyl-D-*erythro*-sphingosylphosphorylcholine (PSM), were purchased from Avanti Polar Lipids (Alabaster, AL). N-(4,4-difluoro-5,7-dimethyl-4-bora-3a,4a-diaza-s-indacene-3-propionyl)-1,2-dihexadecanoyl-sn-glycero-3-phosphoethanolamine, triethylammonium salt (head-labeled BODIPY FL DHPE), and Alexa Fluor 594 hydrazide used to label the head group of asialoganglioside-G_{M1} were purchased from Invitrogen (Eugene, OR). Glass coverslips (25 mm x 25 mm; No. 1.5) from VWR were used as solid supports for the bilayers. Polydimethylsiloxane (PDMS; Sylgard 184) polymer used to fabricate wells and microfluidic devices was purchased from Robert McKeown Company (Branchburg, NJ).

2.2.2 Microfluidic Channel Preparation

The polydimethylsiloxane (PDMS) microfluidic device was made by standard soft-lithography procedures at the Cornell Nanoscale Facility. PDMS prepolymer, along with a curing agent, was cast on the silicon wafer mold and cured at 85ºC for 3 hrs, producing a soft flexible material with the channels embedded in negative relief once removed from the mold. The channel inlets and outlets are connected to outside tubing by punching the PDMS mold with 20 gauge needles (610 μm ID). Glass coverslips, which become the fourth wall of the microfluidic channel, were cleaned in piranha solution (70:30 volume ratio of H_2SO_4 to 50% H_2O_2) for 10 min and rinsed thoroughly with distilled water for 20 min. Before use, glass slides and the PDMS mold were rinsed with deionized water, dried under high purity nitrogen air, and then treated with oxygen plasma using a Harrick Plasma Cleaner (Model # PDC-32G, Ithaca, NY) at a pressure of 750 micron on the high setting for 30 seconds. Immediately after plasma cleaning, the glass slide and PDMS mold were pressed together and heated for 10 minutes at 80ºC to seal the microfluidic channel device.

2.2.3 Formation of Patterned Supported Lipid Bilayers in a Single Stage Microfluidic Device

In this work, SLBs are formed during laminar flow conditions instead of under stagnant incubation. Laminar flow is advantageous for patterning heterogeneous bilayers in microfluidic channels because particles follow streamlines with minimal mixing[158]. Thus, lipid vesicles of different compositions can be sent through the channel on different streamlines and upon rupture will form contiguous, parallel bilayers. If the compositions are chosen so that they are phase stable, these bilayer stripes will have stable interfaces. The compositions of the two coexistent phases used in this work were chosen based on a published ternary phase diagram of POPC/PSM/Chol. We plotted a hypothetical tie line in this phase diagram, guided by previous

literature[193,194] and chose phase compositions close to the ends of this tie line. Recent work corroborates our selection of compositions for two-phase stability[195]. These compositions are 70/20/10 molar ratio of POPC/PSM/Chol, denoted as l_d phase, and 60/40 molar ratio of PSM/Chol, denoted as l_o phase. We found that we could pattern a composite membrane based on these compositions inside a microfluidic channel using laminar flow (as will be described in detail next) to define regions of specific lipid phases within the channel. Membrane-bound biomolecules are able to move between the phases after patterning.

To form a composite lipid bilayer with these lipid phases and load membrane at specified locations, we used the following procedure illustrated in Fig. 2.1. First, we sent l_o phase vesicles and a buffer stream concurrently through the main microfluidic channel. The buffer flow serves to keep the l_o phase vesicle stream, and thus the supported l_o phase bilayer, confined to one side of the channel. During this step, the system was heated to 65°C (both the device and the lipid mixture), so that the l_o phase lipid mixture was above its phase transition temperature and readily fused to the glass surface to form a bilayer. Afterwards, a 65°C buffer was used to rinse out the excess vesicles and the system was equilibrated to room temperature for 1 hr to allow the l_o phase membrane to gradually cool down. Next, the vesicles with load mixture (mixture denoted as red and green dots in orange background) were sent through the perpendicular loading channel. The load mixture was composed of the same composition as lipid l_d phase, but also included small amounts of the labeled glycolipid, Alexa 594-G_{M1}, and BODIPY DHPE lipid (approx. 1 mol % of each). At the same time, buffer flow from all other ports was maintained at a slow rate to prevent the load vesicles from entering into the main channel (these streams are omitted in the illustration). The membrane with the load mixture formed only on the glass surface where there was no bilayer under the stream of the load vesicles. Finally, l_d phase

vesicles were sent through the main channel (denoted as a pink arrow in the figure) and filled the exposed regions of the glass surface that had not been covered by lipid membranes.

In all of these steps, vesicles were exposed to the glass surface for 5 min under flow and then rinsed with buffer for 20 min. When the load formed, the flow rate of the load vesicle solution in the upstream side channel (50 μm wide and 70 μm high) was 10 μL/min and the overall flow rate of the load vesicle solution and buffers in the downstream side channel (50 μm wide and 70 μm high) was 30 μL/min. When the lipid phases formed, the flow rates of vesicle solutions and rinsing buffers were kept at 20 μL/min in the main channel (100 μm wide and 70 μm high).

To transport the mixed species into the main composite bilayer channel after bilayer formation, aqueous buffer flow was applied in the main channel towards the "Y" branch into the exit ports at a rate of 80 μL/min. The hydrodynamic flow provided a shear force on the membrane biomolecules that served to drag them along the main channel. Biomolecules were able to partition into either membrane phase across the channel by diffusion and were collected at the end of the channel in the separate ports.

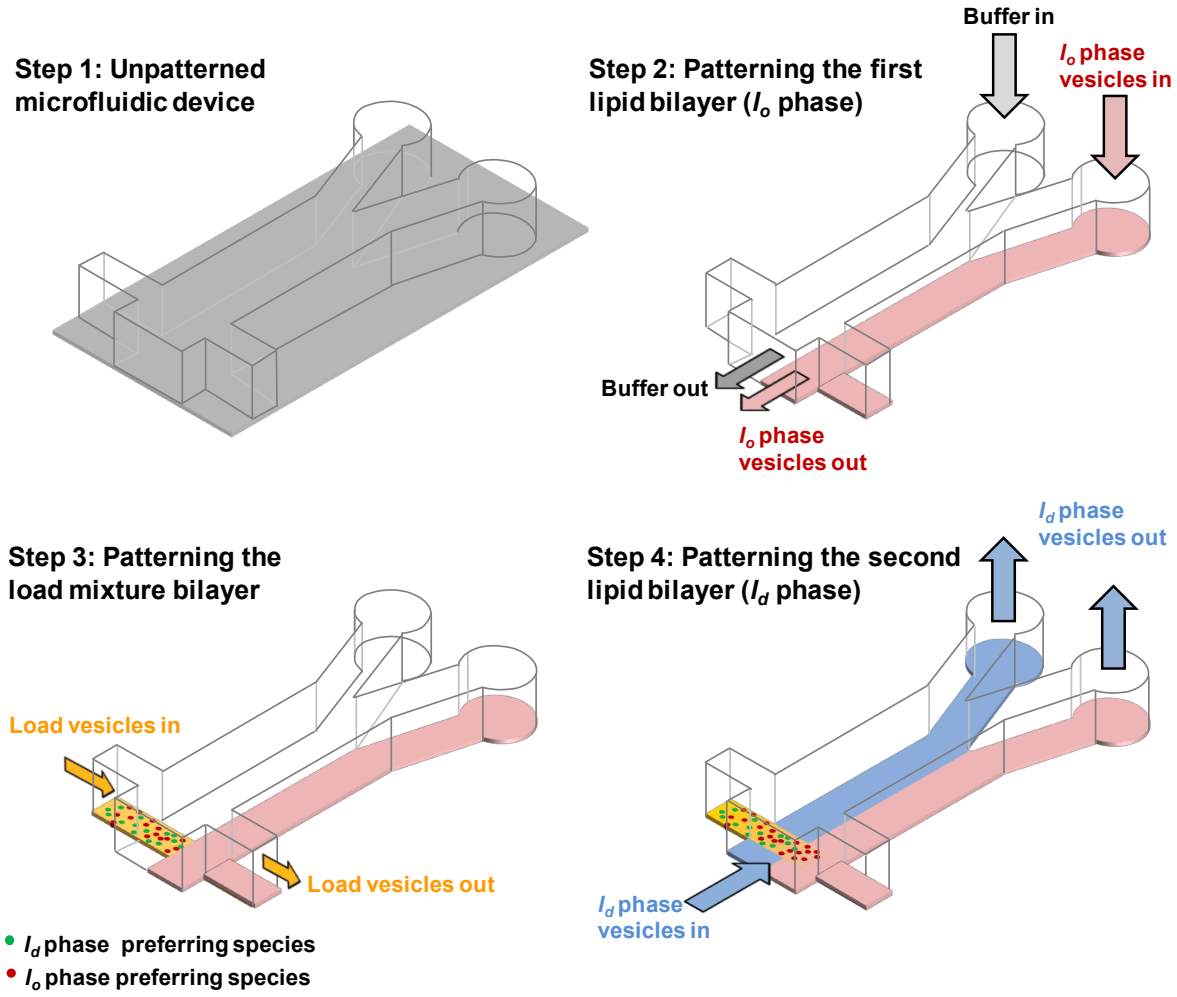

Figure 2.1. A three-dimensional cut-away view illustrating the loading and patterning of bilayers into the microfluidic device via vesicle fusion and laminar flow patterning, as described in the text. The pink color represents lipid l_o phase, the lipid-ordered bilayer; the blue color represents lipid l_d phase, the lipid-disordered bilayer; and the orange color represents the load bilayer that is the same composition as l_d phase, except that it contains the biomolecules to be separated and sorted. Green and red circles represent the biomolecule mixture. The arrows show the direction of the flow and streamlines as the pattern is being formed. Step 1: the blank microfluidic device design consisting of a clear PDMS mold bound to a glass support. The glass support is removed in the subsequent illustrations for clarity. Step 2: patterning lipid l_o phase. During this step the device is warmed to ~ 65ºC. Step 3: forming the load bilayer containing the mixture of membrane-bound biomolecules after l_o phase bilayer has been formed. Load only forms where vesicles contact glass, i.e. not where l_o phase bilayer already exists. Buffer flow also enters from the sides to confine the flow to the loading channel, but is omitted here for clarity. Step 4: patterning the l_d phase bilayer after both the load and l_o phase bilayers are formed. Note that while the l_d phase bilayer is forming, some of the l_o phase-preferring species (red here) begin to partition into the l_o phase bilayer adjacent to the mixture load.

2.2.4 Background Removal and Vignetting Correction

A background subtraction was used to reduce the effect of fluctuations in the light source and to zero the baseline measurement. Background levels measured immediately adjacent to the

channel at each time point where subtracted from all intensity measurements. Even after background subtractions, we found that vignetting remained an issue in our system such that our mass balance did not close entirely. Vignetting causes intensities in the center of the image to be slightly higher than at the edges. The main effect of this on our mass balance is to cause the inlet and outlet fluxes to differ depending on where they were located relative to the center of the field of view.

To correct for slight variation in light intensity, we applied a vignetting correction factor *(f)* to scale the outlet intensity to account for slight uneven illumination. We used the mass balance to solve for this factor at various positions, *L*, along the channel then fit the data to a second order polynomial *F(x)* which could then be used to scale the intensity at any position in the channel. We found that less than 10% correction was required to correct for uneven illumination. The vignetting correction was performed for BODIPY DHPE and Alexa 594-GM_1 independently.

2.2.5 Characterization of the Velocity Profile in a Two-Phase Supported Bilayer Using Fluorophore Photobleaching

In order to visualize and determine the velocity profile within the two-phase striped bilayer, a photobleaching technique was performed similar to that described by Jönsson et al[196]. Briefly, the convective motion of the SLB containing fluorescent species was driven by shear force, provided by the flow of buffer through the microfluidic channel. Flow was started prior to the bleaching experiment to ensure a fully-developed flow profile at a rate of 80 mL/min in the main channel. A thin photobleached line was created across the channel width on the SLB under a 20x objective with an Argon-Krypton tunable laser. The photobleached line was

generated by quickly moving the stage relative to the focused, stationary laser spot. Images were recorded every 10 seconds post-bleach. The photobleached band moved along the direction of the flow and its shape changed accordingly as shown in Fig. 2.4. The displacement of the photobleached line along with its shape evolution reveals how the target molecules are transported in the SLB and was used to determine a model for the velocity profile in the two-phase bilayer. In this experiment both phases of the bilayer were doped with 1 mol % BODIPY DHPE so that the entire cross-section of the bilayer could be photobleached with a single laser line and tracked.

2.2.9 Simulation

A convection-diffusion model was constructed using COMSOL Multiphysics to simulate the transport of membrane species in the extraction device. Parameters for the model were obtained from literature or independent experiments, as described in detail in the *Results* section.

2.3 RESULTS AND DISCUSSION

2.3.1 Separating and Sorting Membrane-Bound Species Using Bilayer Extraction

In analogy to classic liquid-liquid extraction, we demonstrate a 2-D continuous extraction in SLBs by separating two lipid species: the glycolipid G_{M1}, and BODIPY DHPE, a phospholipid. These species were chosen because they have known affinities for the particular lipid phases we employ. For these experiments, we chose two stably coexistent lipid membrane phases in two systems: POPC-based system and DOPC-based system. For POPC-based system, the l_d phase is: 70 mol % POPC, 20 mol % PSM, and 10 mol % cholesterol. The l_o phase is: 60 mol % PSM and 40 mol % cholesterol. For DOPC-based system, the geometry of the two phases was patterned to facilitate continuous extraction and biomolecule sorting to different parts of the microfluidic chip

following enrichment. The feed bilayer, containing the biomolecule mixture to sort, was chosen to match the l_d phase for maximum stability and compatibility. An illustration of the platform is in Figure 2.2A. Bilayer patterning was carried out using a combination of laminar flow and vesicle fusion techniques as described in the *Experimental* section[157].

After bilayer patterning, an applied hydrodynamic flow of the bulk solution in the microfluidic device provides a shear stress to drive the lipids in the membrane to move[177,190,197]. In this particular system, we characterized independently that the intrinsic mobility of biomolecules in the l_d phase is ~5 times greater than the mobility in the l_o phase using a fluorescence recovery after photobleaching technique[157,198,199]. Thus, most of the convection of biomolecules occurs in the l_d phase. When meeting the l_o phase, a biomolecule has the potential to be extracted depending on its chemical affinity. Figure 2.2B shows fluorescence images of continuous extraction in the patterned SLB platform.

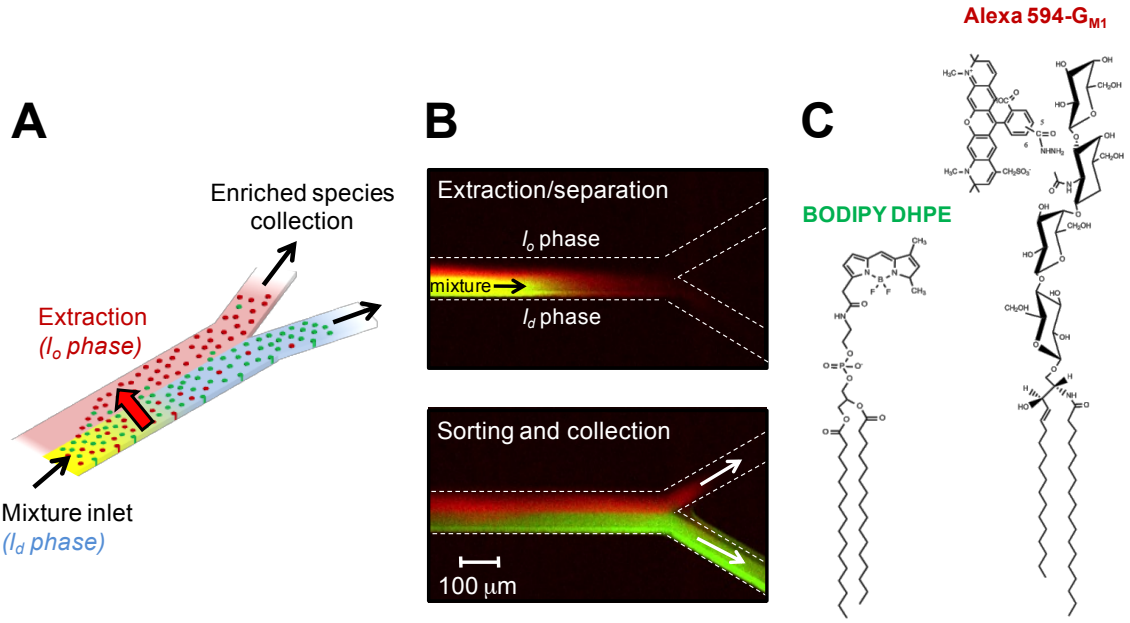

Figure 2.2 (A) A three-dimensional illustration of the two-phase supported lipid bilayer designed to separate and sort membrane biomolecules. The microfluidic device and glass support have been omitted for clarity. Laminar flow in a microfluidic device is used to create parallel stripes of coexistent lipid phases (l_d phase = blue, l_o phase = pink). The interface between the phases is contiguous, allowing membrane-bound molecules to partition into a preferred

phase as they are transported down the main channel. The initial mixture is color-coded as red and green dots and is transported in the l_d phase. Red species are extracted into the l_o phase bilayer, causing the l_d phase to become more enriched in green species. (B) In the experiment, the mixture is BODIPY DHPE (green) and Alexa 594-G_{M1} (red) and appears yellow in the upper image. In these top-view images, the l_d phase was patterned in the bottom section, where yellow is dominant, while l_o phase is in the top half (initially devoid of any fluorophore). The species are transported to the right in the l_d phase membrane along the main channel. The red color ahead of the yellow plug is a small amount of Alexa 594-G_{M1} that moves slightly faster under bulk flow than BODIPY DHPE because it has a larger cross section. In the bottom image, the red Alexa 594-G_{M1} is extracted into the l_o phase, while BODIPY DHPE generally remains in the l_d phase. Separated fractions are split by the "Y" at the end of the channel. (C) The chemical structures of Alexa 594-G_{M1} and BODIPY DHPE.

To demonstrate separation, extraction, and sorting, two fluorescently-labeled membrane biomolecules with differing propensities to partition into the two membrane phases were used. The fluorescent labels make it easy to track the biomolecules' positions in the device and quantify the extraction. We chose the glycolipid, G_{M1}, because it has established membrane partitioning behavior and serves as a typical marker for cell microdomains (lipids rafts). Since the acyl chain label in commercially available fluorescently-labeled G_{M1} disrupts its native preference for ordered lipid phases in cell membranes[31,41], we synthesized a head-labeled version, Alexa 594-G_{M1}[157,181]. We mixed Alexa 594-G_{M1} with another fluorescently-labeled phospholipid, BODIPY DHPE, which generally prefers lipid disordered phases, such as those composed primarily of POPC[157]. The structures of both of these biomolecules are shown in Figure 2.2C. We have also conducted a thorough study on how various lipid phases impact the partitioning kinetics of both Alexa 594-G_{M1} and BODIPY DHPE, shown in Appendix A.

In a first set of experiments, an approximately equimolar mixture of Alexa 594-G_{M1} (red fluorophore) and BODIPY-DHPE (green fluorophore) was loaded into the device (1 mol% of each in the load bilayer formulation), Figure 2.2B. The mixture is yellow when the red and green false-color images are superimposed on each other (Figure 2.2B, top image). Figure 2.2B, bottom image, is a later snapshot of the continuous extraction, showing the preferential affinity of red Alexa 594-G_{M1} to the l_o phase, and the enrichment of the green BODIPY DHPE in the l_d

phase. At the end of the channel a "Y" split directs the fractions to different areas of the chip for collection.

The exposure times during image acquisition for each channel (red or green) were set such that the starting intensities were nearly the same. The fluorescence intensity for each biomolecule in each phase varied linearly with concentration for the range of concentrations used here[157]. Because of these features, fluorescence intensity can be used to report concentration for these species to quantify the enrichment after the extraction process. To minimize photobleaching, samples were imaged every two minutes instead of continuously.

2.3.2 Extraction Efficiency – Theory and Analysis

Based on the design of this device, the extraction channel is analogous to a single stage extractor, operating in the 2-D plane of the bilayer. Due to practical kinetic limitations during experimental operation, the real performance of an extractor is often below what is predicted under equilibrium conditions. The real performance is quantified by calculating yield, *Y*, of a particular species in a particular lipid phase. A control volume in the 2-D membrane is shown in Figure 2.3. Initially, the entire control volume is devoid of any fluorescently-labeled species. The yield in phase *i*, $Y_i(t)$, is defined as the amount of species in phase *i* compared to the overall amount entering the control volume:

$$Y_i(t) = \frac{\alpha_{i,out}(t) + N_i(t)}{\alpha_{ld,in}(t) + \alpha_{lo,in}(t)} \qquad \text{(Eq. 2.1)}$$

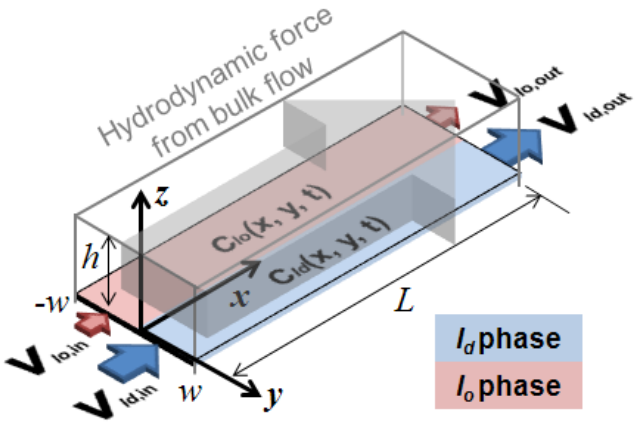

Figure 2.3. 2-D two-phase bilayer control volume in a 3-D view of the microchannel with the parameters used in the data analysis. All parameters are defined in the text.Blue denotes the l_d phase, and pink denotes the l_o phase. The hydrodynamic force from the bulk flow (gray arrow) convects species in the lipid membrane.

Yield in these experiments is a function of time because the initial input (the mixture) is a discrete plug of material and the extracted amount is significantly influenced by the local concentration distribution of the species in the two phases. $a_{i,in}$ and $a_{i,out}$ are the cumulative material that has entered/left the control volume by the reporting time, respectively.

Material accumulation in each phase $N_i(t)$, can be obtained directly by integrating fluorescence from the time-lapse micrographs. Cumulative material entering/exiting a particular phase in the control volume, $a_i(t)$, is defined generally in Eq. 2.2, where $F_i(t)$ is the amount of material entering at $x=0$ or exiting a phase i at $x=L$ in time:

$$\alpha_{i,\,in\,or\,out}(t) = \int_0^t F_{i,\,in\,or\,out}(t)\,dt \qquad \text{(Eq. 2.2)}$$

The equations that describe the amount of the material entering the l_o phase at $x=0$ and exiting at $x=L$ in time are:

$$F_{lo,in}(t) = \int_{y=-w}^{y=0} v(0,y)\cdot C(0,y,t)\,dy \qquad \text{(Eq. 2.3)}$$

$$F_{lo,out}(t) = \int_{y=-w}^{y=0} v(L,y) \cdot C(L,y,t)\, dy \qquad \text{(Eq. 2.4)}$$

where *v(x,y)* is the velocity of a species in the membrane and *w* is the width of the phase cross-section. Under conditions of fully developed bulk flow, the overall velocity profile in the planar membrane is a function of *y* only. The concentration profile across the bilayer can be obtained by measuring fluorescence intensity from experimental images. To calculate the yield, all that remains is to determine the velocity profile in the two-phase membrane.

2.3.3 Characterization of Convection Velocity Profile in a Two-Phase Coexistent Supported Bilayer

In this work, the convection of biomolecules in the supported bilayer is induced by the shear force resulting from bulk buffer flow inside the microchannel. Previous study of homogeneous (single lipid phase) bilayer systems has shown that when sheared in this manner, the upper monolayer of the SLB moves in the direction of the drag while the lower monolayer is approximately stationary[196,200]. These studies suggest that the lipid monolayer can be viewed as a 2-D continuum and the flow velocity can be described by the continuity equation and Navier-Stokes equation for creeping flow in 2-D and assuming fully developed flow and negligible viscous forces and surface pressure gradients.

The velocity profile in a homogeneous bilayer induced by hydrodynamic flow at the bilayer surface within a rectangular channel (Fig. 2.3B) is described by the following set of equations[196,200]:

$$\sigma_{hydro}(y) = -\frac{\Delta p}{\Delta x}\frac{h}{2}\left(1 - \frac{8}{\pi^2}\sum_{k_{odd}}^{\infty}\frac{1}{k^2}\frac{\cosh\left(\frac{k\pi y}{h}\right)}{\cosh\left(\frac{k\pi w}{h}\right)}\right) \qquad \text{(Eq. 2.5)}$$

$$\sigma_{hydro}(y) = -\frac{\Delta p}{\Delta x}\frac{h}{2}\left(1-\frac{8}{\pi^2}\sum_{k\,odd}^{\infty}\frac{1}{k^2}\frac{\cosh\left(\frac{k\pi y}{h}\right)}{\cosh\left(\frac{k\pi w}{2h}\right)}\right) \quad \text{(Eq. 2.6)}$$

$v(y) = \frac{\sigma_{hydro}(y)}{b} e_x$.where $\sigma_{hydro}(y)$ is the shear force from hydrodynamic bulk fluid flow; $\Delta p/\Delta x$ is the pressure drop over length of the channel; y is the position across the channel, perpendicular to the flow direction; h is the channel height; $2w$ is the width of channel; $v(y)$ is the velocity; b is the intermonolayer friction factor; and e_x is the unit vector in the x direction. Note here that the buffer flow is assumed to be fully developed and constant and that viscous forces and surface pressure gradients are negligible compared to the hydrodynamic force[200].

We build upon this work to describe the motion of biomolecules in a two-phase heterogeneous bilayer arranged in two stripes parallel with the bulk hydrodynamic flow. We have experimentally observed that there are three regions with distinct membrane compositions: a l_o phase region, a l_d phase region, and an interfacial transition region in-between[157]. Species present in these different bilayer environments possess different mobilities, and therefore velocities, when subjected to a shear force. The overall velocity profile in this system is approximated as a piece-wise function of the velocity profile in each phase and interfacial region:

$$v(y) = \begin{cases} \dfrac{\sigma_{hydro}(y)}{b_{lo}} e_x & \text{when } y < y_{Tlo} \text{ in the } l_o \text{ phase} \quad \text{(Eq. 2.7 a)} \\ \dfrac{\sigma_{hydro}(y)}{b_{trans}} e_x & \text{when } y_{Tlo} < y < y_{Tld} \text{ in the transition zone} \quad \text{(Eq. 2.7 b)} \\ \dfrac{\sigma_{hydro}(y)}{b_{ld}} e_x = \dfrac{5\sigma_{hydro}(y)}{b_{lo}} e_x & \text{when } y > y_{Tld} \text{ in } l_d \text{ phase} \quad \text{(Eq. 2.7 c)} \end{cases}$$

where y_{Tlo}, y_{Tld} are the locations of the boundaries of the transition zone between the l_o side and l_d side, respectively. b_{lo} = friction factor in the l_o phase, b_{trans} = friction factor in the transition zone between phases, and b_{ld} = friction factor in the l_d phase. The ratio for friction factor in l_o to l_d was ~5 for both BODIPY DHPE and Alexa 594-G_{M1} determined via a photobleaching technique. This ratio is substituted into Eq. 2.7c to reduce the number of parameters.

b_{trans} is difficult to define because the exact structure of the interfacial zone is unknown. However, since this region is small compared to the rest of the channel, we make the approximation that the velocity (and therefore b) varies linearly in this region. Thus, the velocity in this region can be rewritten to eliminate b_{trans} in Eq. 2.7 b as:

$$v(y) = \sigma_{hydro}\left(\frac{1}{b_{lo}} + \frac{y - y_{Tlo}}{y_{Tld} - y_{Tlo}}\left(\frac{1}{b_{ld}} - \frac{1}{b_{lo}}\right)\right)e_x = \sigma_{hydro}\left(\frac{1}{b_{lo}} + \frac{y - y_{Tlo}}{y_{Tld} - y_{Tlo}}\left(\frac{4}{b_{lo}}\right)\right)e_x \quad \text{when } y_{Tlo} < y < y_{Tld} \quad \text{(Eq. 2.8)}$$

The general velocity profile shape was visualized (Fig. 2.4A, inset) using a photobleaching technique. The general shape is captured by our piece-wise model, so b_{lo} is the only parameter remaining to obtain the $v(y)$.

Note that the photobleaching technique cannot be used directly to obtain b_{lo} in each extraction run because fluorescence intensity is being tracked as a proxy for concentration. Instead, an independent mass balance is used to determine the value of b_{lo} that corresponds to the

experimental conditions of a particular run. To illustrate the mass balance process, we present the result for one experiment using the longest channel length, 710 mm, at 80 ml/min bulk flow rate (Fig. 2.3). This mass balance procedure is repeated for each experiment to obtain the best fit parameter for that experiment. The mass balance on the control volume is:

$$Accumulation(t) = \int_0^t \int_{-w}^{+w} \left[C(0,y,t)\cdot v(y)\right]_{in} - \left[C(L,y,t)\cdot v(y)\right]_{out} dy\, dt \quad \text{(Eq. 2.9)}$$

Accumulation (LHS side of Eq. 2.9) can be obtained directly from time-lapse fluorescence micrographs and plotted as a function of time, as shown for Alexa 594-G_{M1} in Fig. 2.4C (solid line). For the RHS of Eq. 2.9, the concentrations, $C(0,y,t)$ and $C(L,y,t)$, are obtained directly from the fluorescence micrographs at the inlet and outlet locations. At this point, the magnitude of $v(y)$ for the RHS of Eq. 2.9 is unknown, but the shape of the profile has been experimentally verified, as described above, and is given by Eq. 2.7. Because the flow is steady, $v(y)$ does not vary with x, so the values at the inlet and outlet on a particular streamline are the same, i.e., $v(y)_{in} = v(y)_{out}$. b_{lo} is determined by minimizing the difference between the LHS and RHS of Eq. 2.9 (solid vs. dashed lines, Fig. 2.4C). For Alexa 594-G_{M1} for this particular run, b_{lo} = 3.0 x 10^8 Pa·s/m. The red line in Fig. 2.4B is the corresponding velocity profile for Alexa 594-G_{M1}. The same procedure is followed for BODIPY DHPE. The values for intermonolayer friction coefficients (b_i's) averaged over several experiments are shown in Table 2.1 and correspond well to values found in literature for similar bilayer phases[191,201].

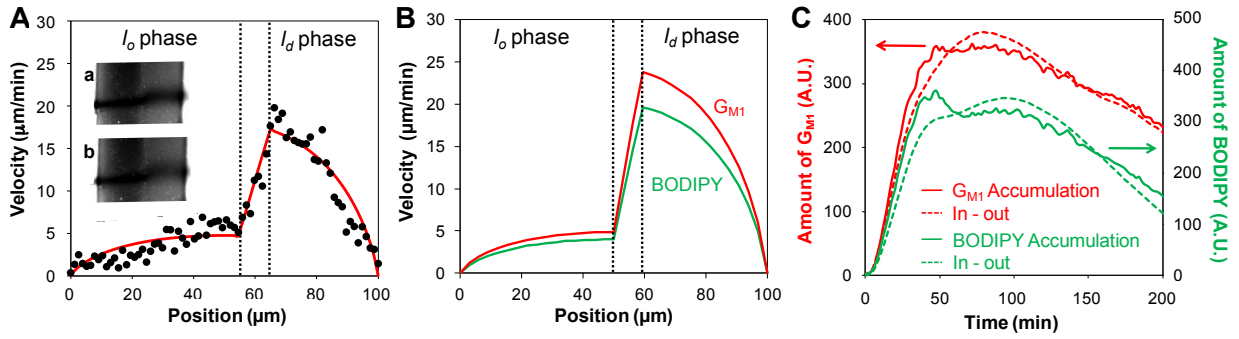

Figure 2.4. Velocity profile and mass balance. (A) Velocity profile obtained by photobleaching experiments (inset) to verify the shape of the profile and our model. Black data points are the velocities as a function of position across the channel, derived from the photobleached images, (a) and (b), during 80 ml/min buffer flow rate. The red line is the best fit of the data by our model, equation 5. (B) Velocity profiles for Alexa 594-G_{M1} (solid red) and BODIPY DHPE (dashed green) determined for a particular extraction experiment using the 710 mm extraction channel. The interface region between each phase is defined by the black dashed lines. (C) The accumulation of species in the control volume (LHS Eq. 7) versus the difference between the inlet and outlet material flux for the control volume (RHS Eq. 2.7) in a representative run at 80 ml/min bulk flow rate for Alexa 594-G_{M1} (red), and BODIPY DHPE (green). These curves have been purposely offset to by an arbitrary factor to separate the data. Velocity for each species was determined independently by minimizing the least squares error between the LHS and RHS.

Table 2.1. Average values determined for *b* based on four experiments.

Intermonolayer friction coefficient, *b* [Pa·s/m]	**BODIPY DHPE**	**Alexa 594-G_{M1}**
l_o phase	$3.6 \pm 1.1 \times 10^8$	$2.8 \pm 0.8 \times 10^8$
l_d phase	$7.3 \pm 2.1 \times 10^7$	$5.6 \pm 1.7 \times 10^7$

2.3.4 Extraction Performance

Once the velocity profile for an experimental run has been obtained, the yield of species can be calculated from Eq. 2.1. To quantify the enrichment of species in each phase, we measured the accumulation (yield) of both G_{M1} and BODIPY DHPE in the l_o phase as a function of the average residence time of a species in the device. The residence time, t, is defined as the ratio of the channel length, L, to the average velocity of a species, $\hat{v}_{ld}$, in the l_d phase: $t = L/\hat{v}_{ld}$.

The residence time can be increased by increasing the length of the control volume or reducing the bulk flow rate. Here, we fix the bulk flow rate at 80 ml/min and varied the control

volume lengths: 89, 355, and 710 mm. Each experiment is performed using the same channel geometry, bilayer compositions, and patterning, and a 50:50 starting mixture. % yield obtained from the experimental results for different residence times are shown in Fig. 2.5. For the longest residence time, ~ 34% of the entering Alexa 594-G_{M1} is extracted into l_o phase during 200 minutes, while ~19% of the BODIPY DHPE is extracted.

Species	L (μm)	τ (min)	Yield in l_o phase (%)
Alexa – G_{M1}	89	4.7	26 ± 5
	355	19	28 ± 1
	710	37	34 ± 2
BODIPY DHPE	89	6.2	10 ± 4
	355	25	13 ± 3
	710	50	19 ± 3

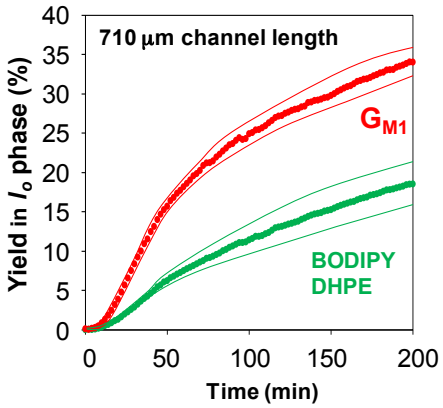

Figure 2.5. (Left) Yield of species to the l_o phase at various residence times, t. The buffer flow rate was constant at 80 ml/min, but the length of the channel, L, was varied. These yields correspond to total experimental time, t = 200 min of collection. (Right) The accumulated yield of species in the l_o phase normalized by the total amount that has entered the control volume for L = 710 μm. These data are averaged over 4 experiments at the same conditions. The thin lines bounding the data points are the standard deviation of the data.

The shape of the yield curve is influenced by the transport properties the biomolecule. If operated at equilibrium conditions, the extraction yields to the l_o phase are 66% and 38% for Alexa 594-G_{M1} and BODIPY DHPE, respectively, based on previously measured equilibrium partition coefficients of 1.96 and 0.6 from Chao & Daniel[157]. Thus, even at the longest channel length investigated, equilibrium is not reached. Optimization of the channel dimensions, patterning, lipid phase selection, and process conditions can be carried out to approach equilibrium. One possibility is to lengthen the channel more, but this is only practical to a limit, beyond which diffusion becomes significant during laminar flow patterning and results in a less

defined interface between lipid phases. Alternatively, decreasing the flow rate could allow partitioning to approach equilibrium. We found that halving the bulk flow rate increased the yield of G_{M1} to the lipid-ordered phase to ~ 40% at t = 200 min for L = 710 mm. The tradeoff here is that the extraction takes longer.

2.3.5 Verification of mass balance analysis using convection-diffusion model of species transport

To independently verify $v(y)$ and the intermonolayer friction factors (b_i's), we modeled the convection-diffusion for each species using COMSOL to simulate the extraction process. Parameter inputs were diffusivity, partitioning rates, and the b_i's (calculated as described above) to obtain the temporal concentration profiles in the control volume.

A simple model of the extraction channel was developed which used experimental concentration data and measured quantities to predict the species distribution during an extraction run (Fig. 2.6).

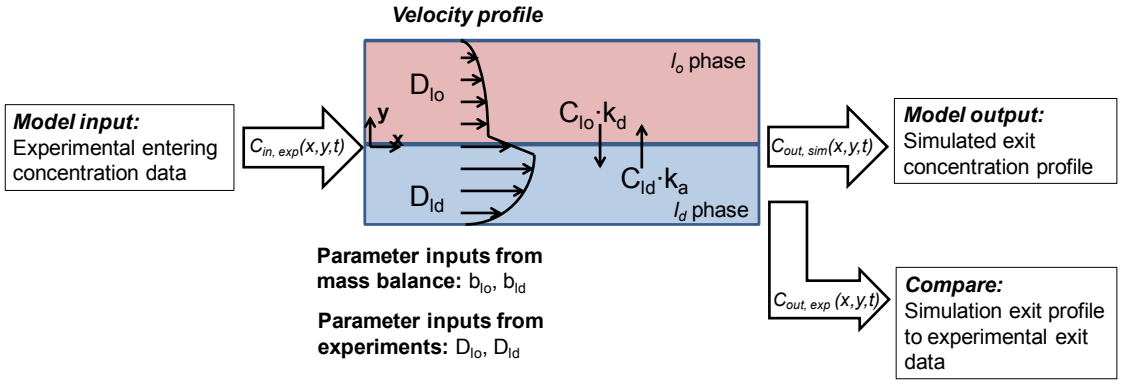

Figure 2.6. Strategy for comparing experimental data to simulated concentration profiles from the COMSOL model of convection-diffusion.

The model governing equation comes from the convection-diffusion process with an imposed velocity profile in the x-direction, given by the following equation:

$$\frac{\partial c(x, y, t)}{\partial t} = \nabla(D(y)\nabla c(x, y, t)) - \nabla(\vec{v}(y)c(x, y, t)) \qquad \text{(Eq. 2.10)}$$

where c is the concentration of the species, D is the diffusion coefficient of a species, and v is the velocity of the species. The diffusivity of each species in each phase is experimentally measured and is dictated by the properties of the lipid environment. We used fluorescence recovery after photobleaching to determine diffusion coefficients of each species in separate experiments (as described above). These values are reported in Table 2.2.

Table 2.2. Diffusion coefficient values used in Eq. 2.14 in the COMSOL simulation.

Lipid environment	**BODIPY DHPE**	**G_{M1}**
Liquid-disordered phase	0.63 $\mu m^2/s$	0.70 $\mu m^2/s$
Liquid-ordered phase	0.13 $\mu m^2/s$	0.14 $\mu m^2/s$

The velocity profile assumed here is that given by Eq. 7. Note that the experimentally measured inlet concentrations from raw fluorescence intensity values are the inputs to the COMSOL model. The boundary condition at the interface between phases is a flux corresponding to the partitioning kinetics of the system:

$$\frac{dN_{lo}(x,t)}{dt} = k_a c_{ld}(x,t) - k_d c_{lo}(x,t) \qquad \text{(Eq. 2.11)}$$

In this equation, N is the accumulation in the liquid-ordered phase, c represents concentration at the interface in either the l_d or l_o phases, and k_a and k_d represent the association and dissociation rate constants for the l_o phase, respectively.

The model was evaluated by comparing predicted outlet concentration profiles with experimentally measured profiles. Figure 2.7 shows comparisons of predicted to measured profiles for both G_{M1} (red) and BODIPY DHPE at the three different channel lengths studied.

The parameters used in these cases were measured diffusivities and partitioning coefficients and calculated intermonolayer friction factors. It was found that these parameters resulted in close matches to experimental data, especially for the shorter channel lengths. Increasing the friction factor would lead to a later eluting plug and decreasing leads to an earlier eluting plug causing significant mismatch in the profiles.

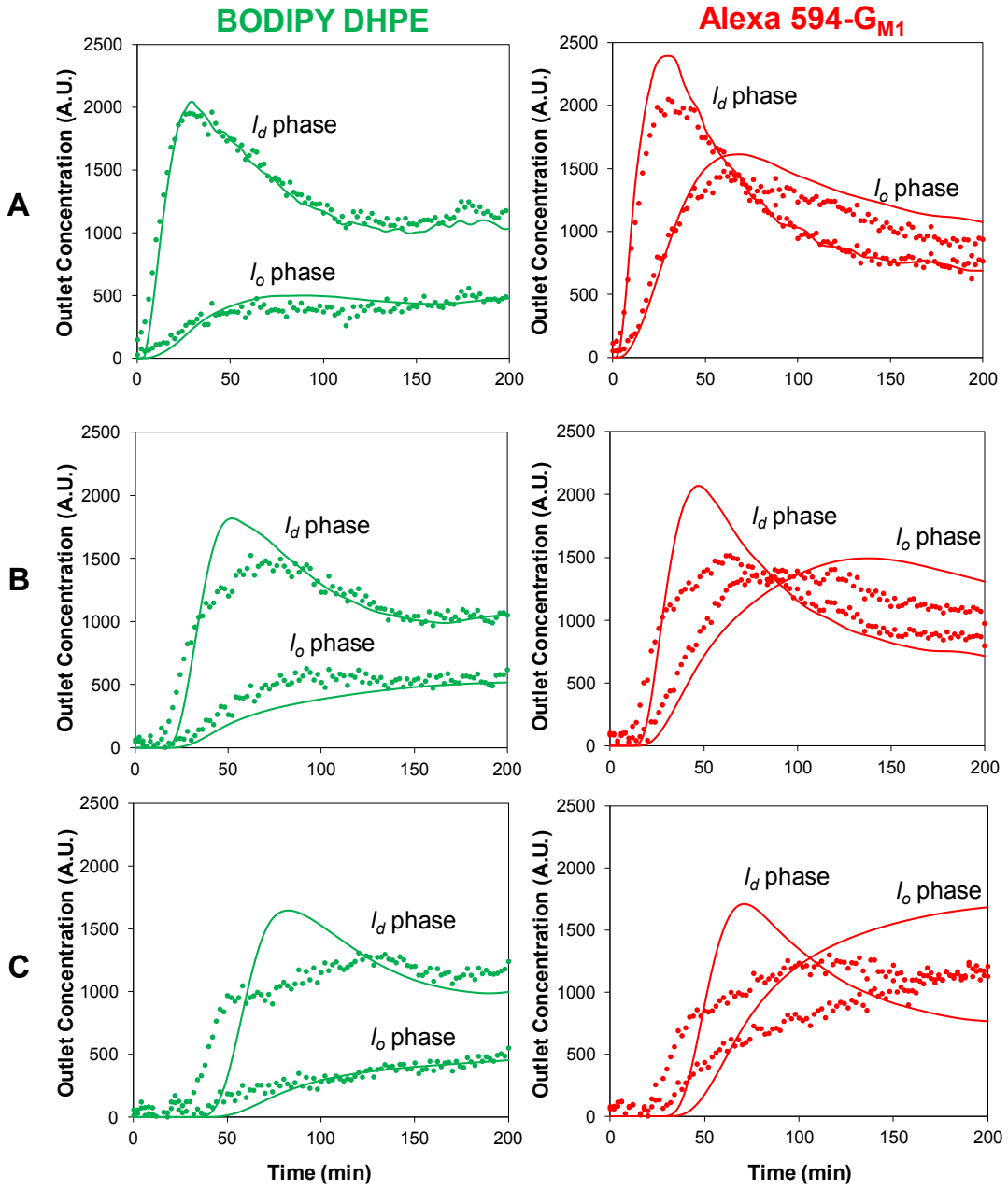

Figure 2.7. Comparison of outlet concentrations in each lipid phase from a representative experiment (points) to

model predictions (solid lines) for various channel lengths. (A) 89 μm; (B) 355 μm; (C) 710 μm. Data are separated into average l_o and l_d phase concentrations in the control volume for BODIPY DHPE (green, left side) and Alexa 594-G_{M1} (red, right side).

There are some differences between the predicted concentration profiles and the experimentally measured profiles that we attribute to complexities not accounted for in this model. We believe one source could be patterning and bilayer imperfections. Our model assumes that the geometry of the bilayer phases is two rectangular regions, but imperfections in the patterning could lead to varied extractor geometries. Additionally, minor bilayer imperfections in the extractor contribute to a dispersive effect in part by immobilization of species in bilayer defects. The cumulative effect of these defects could lead to deviations between the model predictions and the fluorescence data over long channel lengths. Dispersion differences are apparent by the change in the shape of the experimental data compared to the simulation curve as the channel length increases. Notice that the peak position for the experimental data and simulation generally remain registered, which is most obvious in the l_d phase data, but as the channel length increases, the width of the experimental peak grows larger relative to the simulation. In addition, we have made the simplifying assumption in our model that the interface region is infinitesimally small. Perhaps modeling the interface region as having a finite width with mixed phase properties could also improve the accuracy of the simulation.

The b_i's determined by mass balance and used in the simulation predicted concentration profiles that closely matched experimental profiles (Fig. 7), especially for shorter channel lengths. Other values shifted the elution time of the plug forward or backward because b directly impacts the velocity of the species in the bilayer. The shape of the velocity profile is also critical to accurate modeling of the extraction. Inputting, for example, a uniform (average) velocity in each lipid phase across the channel (a step function velocity profile) with constant averaged b_i's

was unable to capture the experimental concentration profiles.

When simulating the extraction for longer channel lengths, deviations grew between the experimental output concentration profiles and the model predictions (Fig 2.7). However, these deviations appear to have only a small effect on the predicted yield curve of an extracted species to the l_o phase up to the time of collection at t = 200 min as shown in Fig. 2.8.

Deviations between experimental results and simulation may result if the experimental velocity profile is not fully developed. We confirmed via photobleaching experiments that the flow is fully developed. Another explanation is that additional experimental dispersive effects that are not accounted for in the model become compounded as the channel lengthens. These effects may include patterning defects that disrupt the flow slightly and/or result in immobilization of biomolecules. These effects may accumulate as the length of channel increases. Nonetheless, our basic simulation reasonably predicts the extraction in this device, verifying that the parameters used in the model are acceptable. This model can be used to predict the enrichment of other biomolecules in this and other two-phase systems, or in optimizing the design of extraction devices.

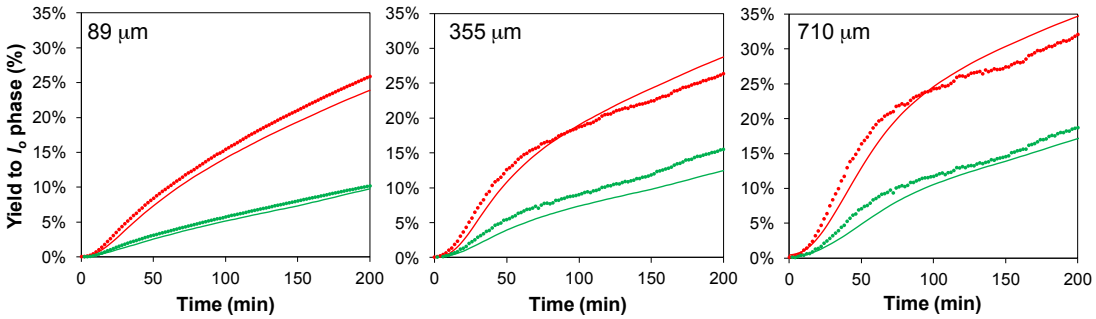

Figure 2.8. Comparison of yield of each species to the l_o phase for various channel lengths, as determined by experiment (points) and the model (lines) for Alexa 594-G_{M1} (red) and BODIPY DHPE (green).

2.3.6 Control Experiment Conducted in Single Phase Bilayer

The following control experiment shows that the observed enrichment of species along the

axial length of the channel is not an artifact of the experiment. Here we conduct the experiment in exactly the same manner as described previously, except that instead of patterning with a two-phase bilayer of parallel phase zones down the axial length of the channel, we pattern the channel with a bilayer of only one composition (l_d phase). In Fig. 2.9, l_d phase has been patterned in the channel and illustrates that enrichment is not observed in the absence of a two-phase patterned bilayer. A similar result is obtained when only l_o phase bilayer is used as a homogenous bilayer phase in the channel.

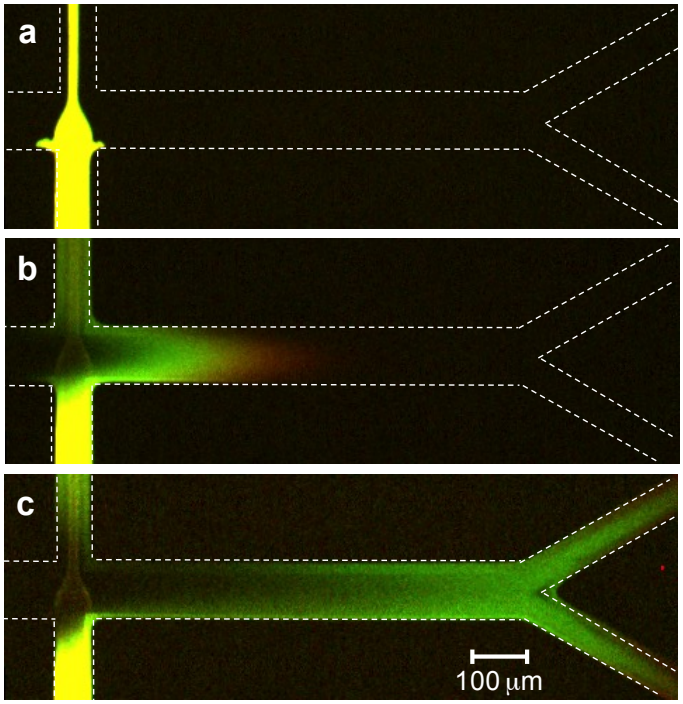

Figure 2.9. Control experiment of separation channel composed of only one phase. In this case only l_d phase composition is used to pattern the microchannel with a bilayer. In (a) the load consists of a mixture of Alexa 594-G_{M1} (red) and BODIPY DHPE (green). The dashed lines are superimposed on the image to outline the microchannel. (b) The load channel is transported down the main microchannel by hydrodynamic flow and no partitioning across the channel is observed. (c) In the absence of the two-phase bilayer, equal portions of the initial load are split equally at the "Y", resulting in no separation, sorting, or concentration of species from the initial load amount.

2.4 CONCLUSIONS

The SLB extractor platform described herein can spatially separate, enrich, and sort membrane-bound species based on their affinity for a specific lipid phase. We created two coexistent lipid phases, in analogy to classic liquid-liquid extraction, but operating in a flat plane of the supported bilayer. We demonstrate that G_{M1}, a typical lipid microdomain marker. can be extracted to an ordered lipid phase and become enriched, relative to non-raft species. This new platform does not require detergent, secondary antibody labeling methods, or electric fields often used in other strategies to identify lipid microdomain residents. Additionally, since the phase locations can be patterned to direct the species to a collection area, characterization tools, such as mass spectroscopy and surface plasmon resonance, could be also integrated at the outlet of this platform to identify unknown species or combined with other downstream analytical assays.

The approach described here is currently being extended to separate and sort lipids and proteins with posttranslational modifications, such as the addition of GPI anchors, sterols, and single saturated or unsaturated fatty acids. The platform is compatible with species derived from cell membranes and creating supported bilayers from sections of cell membrane has recently become possible[202,203], including a new technique developed by us[204]. In the future, this platform could be extended to separating and sorting transmembrane species by integrating an appropriate cushion beneath the bilayer to minimize protein-support interactions[203]. Finally, this platform may be useful not just for separating and facilitating the identification of membrane domain residents, but for characterizing how post-translational modifications, interactions with soluble species, or environmental conditions shift the affinity of species to a particular lipid phase[53,205].

2.5 ACKNOWLEDGMENT

This chapter was published in its entirety in "Analytical Chemistry[206]. Ling Chao and Mark J. Richards and were co-first authors on this paper with co-authors Chih-Yun Hsia and Susan Daniel. Chih-Yun Hsia has contributed to the following work: *Separating and Sorting Membrane-bound species using bilayer extraction, characterization of convection velocity profile in a two-phase coexistent supported bilayer and measuring partitioning behavior of biomolecules in heterogeneous bilayers (Appendix A).* We thank the National Science Foundation (EEC-0824381, CBET-1149452) and an Innovation Grant from the Institute for Biotechnology and Life Science Technologies at Cornell University for support. This work was performed in part at the Cornell NanoScale Facility, which is supported by the NSF (ECS-0335765).

CHAPTER 3

CREATE PROTEINACEOUS SUPPORTED LIPIDS BILAYERS DIRECTLY FROM MAMALIAN CELL MEMBRANES

3.1 INTRODUCTION

Understanding the functions of membrane proteins is important for combating disease and designing therapeutics, but they are a complicated and challenging class of biomolecules to study, as reviewed in a recent publication[170]. Cell-based studies of membrane proteins have provided valuable information because all native interactions are captured, but system complexity makes it difficult to isolate individual factor effects quantitatively. An alternative is to extract the proteins from the cell membrane and assay their behavior in an aqueous environment, but this often alters membrane protein structure and function from that of the native state[207]. Furthermore, the local interactions and organization of lipids and proteins are believed to regulate membrane protein activity[17,208] and thus are a crucial component of their study. With this in mind, new techniques bridging whole-cell complexity and membrane interactions with quantitative and flexible *in vitro* methods are desired.

Model membrane studies which utilize an artificial lipid bilayer have provided a framework for retaining critical membrane interactions among constituents while enabling the use of a wide variety of experimental techniques for characterization[115,133,157,206,207,209]. The supported lipid bilayer (SLB) platform provides a chemically tunable, planar geometry that is compatible with a vast array of surface characterization tools, such as total internal reflection fluorescence (TIRF) microscopy[116], atomic force microscopy (AFM)[117], quartz crystal microbalance (QCM)[210], and surface plasmon resonance (SPR)[120], among many others. While significant work has been

carried out using SLBs, their full potential has yet to be reached because of the challenges associated with integration of membrane proteins.

Several significant challenges remain for incorporating membrane proteins into SLBs, namely maintaining their fluidity, orientation, and function. The most significant bottleneck is the method in which membrane proteins are introduced into the SLB. To sidestep these issues, some studies use peripheral or self-inserting membrane proteins which can be introduced in solution after a bilayer has been formed and insert themselves in the membrane[130,133,143]. This limits the scope of the platform to a very small subclass of proteins. A prevalent alternative is to use a membrane disruption and proteoliposome reconstitution procedure often with the use of detergents[132,197,211,212]. Here, proteins are solubilized from the membrane with detergent (or mechanically), isolated from the cell debris, then reformed into proteoliposomes. Not only does this method involve tedious optimization of detergents, lipids, and conditions for each protein, but the process can also alter the protein orientation and structure[5,213–216].

We have developed a general method for the delivery of membrane proteins to the supported bilayer platform via cell blebs, which results in oriented, mobile proteins in the SLB. Cell blebs are sections of the cell membrane that bud off into a type of proteoliposome as a result of local detachment of the membrane from the actin cystoskeleton[217]. Overproduction of blebs is typically triggered by chemical means, and afterwards the blebs are collected from the culture media[95,218]. However, under specific conditions certain cell types bleb naturally without chemical induction. Expressing membrane proteins directly in mammalian cells and collecting the cell blebs circumvents the difficult purification and reconstitution procedures. Importantly, native membrane travels with the membrane proteins all the way to the SLB platform, so any crucial lipid interactions can be preserved. Finally, the use of mammalian hosts ensures proper folding

and post-translational modifications such as glycosylation and S-acylation. In previous work, we demonstrated that membrane proteins can be delivered to a supported lipid bilayer using this blebbing technique and remain functional as viral receptors[204,219]; however, these receptors were not mobile, which can reduce the efficacy of multivalent binding interactions. In general, protein mobility is important because membrane proteins need to be able to diffuse laterally to properly interact with co-factor species to function as they do within the cell plasma membrane. Thus, for this platform to be most useful, gaining protein mobility and proper orientation is paramount.

The major hurdle with this system, and SLBs in general, is protein immobility caused by interactions between the extramembranous regions of the proteins and the underlying glass support. In a typical SLB there is a small, ~1 nm water gap[126], that cannot accommodate extracellular or cytosolic domains of membrane proteins that could extend around 10 nm from the membrane[127]. In this work, we overcome protein immobility by mixing cell blebs with polyethylene glycol (PEG) containing vesicles to generate a cushioned bleb bilayer which increases the distance between the bilayer and glass surface[133]. Our design goal was a platform that would be general and applicable to a wide variety of types of membrane proteins. To this end, we tested a peripheral glycophospotidylinositol (GPI-linked) protein and a multi-pass transmembrane protein (MPTMP) (Fig. 3.1). The GPI-linked yellow fluorescent protein (GPI-YFP) was our representative GPI protein for this study. GPI proteins are linked to the extracellular leaflet of the plasma membrane via a lipid anchor instead of a transmembrane peptide and are involved in a variety of cellular processes including signaling, enzymatic catalysis, and cell adhesion[220]. They are typically sorted to raft microdomains[18] and some are used as targets for anti-cancer therapeutics because of their overexpression in tumors[221]. For a MPTMP, we examined the P2X2 receptor fused to a neon green fluorescent protein, referred to

here as P2X2-Neon. The P2X receptors are ATP-gated ion channels that are found in almost all mammalian cells and play important roles in inflammation, sensation of pain and taste, and control of vascular tone[222]. Each P2X2 receptor harbors two transmembrane helices and assembles into a functional trimer (thus total six transmembrane helices) in the plasma membrane[223]. Individual membrane proteins were tracked and their motions were analyzed to distinguish diffusion modes in the cushioned bleb-based bilayer system. We characterized the orientation of membrane proteins in the bleb bilayer and determined that the rupture process for both types of proteins results in predominantly outward facing membrane proteins, implying a "parachute"-type mechanism of bleb rupture[224]. Finally, we compare bleb bilayers created using chemically induced and native blebbing and found that at low levels, chemical induction does not hinder protein mobility in bleb bilayers. These supported bleb bilayers containing mobile, oriented proteins preserved with lipids from the plasma membrane are a critical intermediate platform that bridges whole cell to *in vitro* systems and will play a key role in novel membrane proteomic and lipodomic studies in the future.

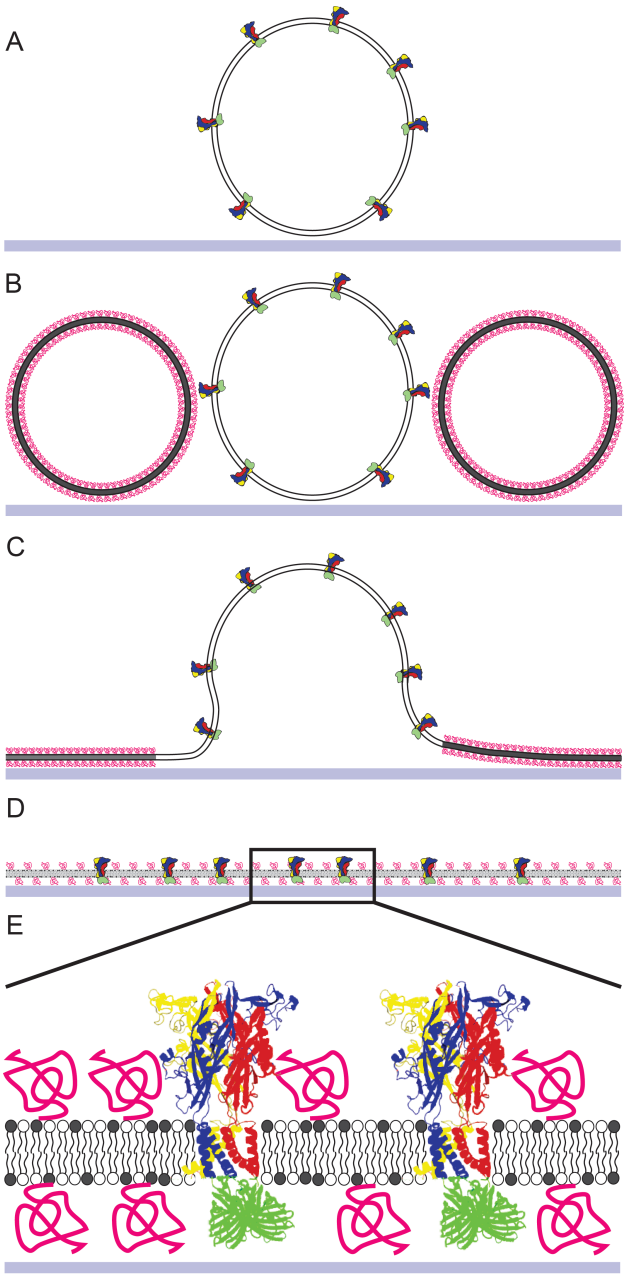

Figure 3.1. Depiction of the PEGylated bleb bilayer formation process demonstrated for P2X2-Neon membrane protein delivery (based on P2X4 structure solved by Kawate et al.[225]). Blebs (depicted by white lipids) are first adsorbed to the glass slide (A) and PEGylated lipid vesicles (black lipids) are then added (B). As the lipid vesicles rupture, they induce rupturing of neighboring blebs (C). The dominant rupture mechanism appears to be a "parachuting" mode where the inner leaflet of the bleb becomes the lower leaflet of the bilayer as determined from enzymatic accessibility assay results. Bilayer constituents are free to diffuse in the resulting cushioned bleb bilayer (D). A magnified view of the bleb bilayer shows the relative scale of the P2X2-Neon membrane protein (E).

3.2 EXPERIMENTAL SECTION

3.2.1 Materials

1-Palmitoyl-2-oleoyl-sn-glycero-3-phosphocholine (POPC), 1,2-dipalmitoyl-sn-glycero- 3-phosphoethanolamine-N-[methoxy(polyethylene glycol)-5000] (PEG5000-PE) were purchased from Avanti Polar Lipids (Alabaster, AL). The fusogenic liposomes were composed of 99.5% POPC with 0.5% PEG5000-PE.

3.2.2 Cells, Plasmids, and blebs

HeLa cells were maintained in RPMI 1640 medium (CellGro) supplemented with 10% fetal bovine serum (GIBCO), 100 U/mL penicillin (CellGro), 10 μg/mL streptomycin (CellGro), 2 g/L sodium bicarbonate (Sigma), and 1% HEPES buffer (CellGro) in a 37°C, 5% CO2 incubator (ESCO). The pYFP-GPI-N1 plasmid, a generous gift from the Baird/Howlawka research group at Cornell University, was used in transfection to produce a glycophosphatidylinositol (GPI) anchored yellow fluorescent (YFP) protein. The pINR3-Neon-THR-P2X2 plasmid was generated by inserting the full length mouse P2X2 receptor (GI: 258679504) followed by a thrombin cleavage site (Gly-Leu-Val-Pro-Arg-Gly) between BamHI and XhoI in pINR3 vector using a standard molecular biology technique. The pINR3 vector was modified from the pIRES-EGFP RK6 vector (provided by M. Mayer, National Institutes of Health, Bethesda, MD) such that the Neon Green fluorescent protein can be expressed as a fusion protein while mRuby2 fluorescent protein is expressed using an internal ribosome entry site. All DNA constructs were verified by sequencing.

3.2.3 Cell Membrane Bleb Preparation

Cell blebbing was performed using two different methods: serum starving of HeLa cells and via chemical induction. For both methods, 6 mL of cells were seeded at a density of 1.5 x 10^5

cells/mL in a 10 cm culture dish (Corning). Transfections were performed using 2 μL TurboFect (Thermoscientfic) and 6 μg of DNA in each culture dish and according to manufacturer instructions and incubated for 24 hrs. In the serum starving protocol, HeLa cells were washed with serum-free RPMI media and then incubated with 4 mL of serum-free RPMI media for 4-6 hrs before collection of the bleb containing supernatant. The chemical induction protocol has been described previously[204]. Briefly, after 24 h cells were washed with a buffer containing 2 mM $CaCl_2$ (J.T. Baker), 10 mM HEPES, 150 mM NaCl (BDH) at pH 7.4. Subsequently, 4 mL of a second buffer containing the same base components but additionally either 25 mM formaldehyde (Sigma) and 2 mM dithiothreitol (Sigma) or 500 mM formaldehyde and 40 mM dithiothreitol to induce blebbing. Blebs were collected from the supernatant and stored at 4 °C for up to one week before use, although it was determined that they were stable for up to one month.

3.2.4 Bleb Bilayer Formation for Fluorescence Microscopy

Glass slides (25 x 25 mm No. 1.5, VWR) were cleaned with piranha solution (mixture of 70% (v/v) H_2SO_4 (BDH) and 30% (v/v) H_2O_2 (Sigma 50 wt. %) for 10 min then rinsed for 20 min under 18.2 MΩ-cm water (ELGA Purelab Ultra, Woodridge, IL). Polydimethyl siloxane (PDMS) wells (5 mm diameter, 3 mm thick) were affixed to the clean, dry slides. 70 μL of bleb solutions at approximately 4 x 10^8 blebs/mL were incubated for 10 min in the wells (see Supporting Information). Afterwards, the well was rinsed vigorously with PBS buffer to remove excess, unadsorbed material. Bleb bilayer formation was induced by adding 70 μL of rupture liposomes at 0.5 mg/mL into the well and incubating for 30 min before rinsing again with PBS buffer. In a subset of experiments to verify rupturing of blebs, octadecyl rhodamine (R18, Molecular Probes), a membrane-intercalating fluorophore, was doped into blebs, and unincorporated probe

was removed using a G25 spin column (GE Healthcare, Buckinghamshire, UK) prior to bleb incubation on a glass slide. An inverted Zeiss Axio Observer.Z1 microscope with α Plan-Apochromat objectives, a Hamamatsu EM-CCD camera (ImageEM, model C9100-13, Bridgewater, NJ), and X-Cite® 120 microscope light source (Lumen Dynamics Group Inc., Canada) was used to visualize the bleb rupturing process. An ET MCH/TR filter cube (49008, c106274, Chromatech Inc.) was used to collect the fluorescence emitted from the R18 fluorophores. A 20 μm diameter spot in the supported lipid bilayer was bleached with a 4.7 mW 488 nm krypton/argon laser for 400 ms. The recovery of the intensity of the photobleached spot was recorded for 15 min at regular intervals. The fluorescence intensity of the bleached spot was determined after background subtraction and normalization for each image. The recovery data was fit using a Bessel function following the method of Soumpasis[198]. The diffusion coefficient is then calculated using the following equation: $D = w^2 / 4t_{1/2}$, where w is the full width at half-maximum of the Gaussian profile of the focused beam.*3.2.5 Quartz Crystal Microbalance with Dissipation Monitoring (QCM-D)*

QCM-D was used to verify bleb bilayer formation. All experiments were measured on QCM-D crystals made of silicon dioxide (QSX303, Q-Sense, Sweden) using a Q-Sense E1 (Q-Sense, Sweden) instrument. Solutions were pumped into the chamber by Peristaltic pump (Ismatec Reglo Digital M2-2/12, Q-Sense, Sweden).

This technique measures changes of resonance frequency (Δf) and energy dissipation (ΔD) of an oscillating piezoelectric quartz crystal, which is driven by an applied AC voltage. In this paper, we focus on the third overtone (15 MHz), which captures the bleb bilayer formation process. The shift of resonance frequency (Δf) reflects the change of adsorbed mass on the quartz crystal sensor. Simultaneously, shifts of energy dissipation (ΔD) were measured, which

characterize the viscoelastic properties of the adhered layer to the crystal surface.

Before measurements, crystals were cleaned with 18.2 MΩ-cm water and ethanol, and dried with nitrogen gas. Crystals were then plasma cleaned in UV-Ozone Procleaner (Bioforce) for 10 minutes to remove any organic contamination. PBS buffer was pumped into the system at a flow rate of 100 μL/min for 5 min. Thereafter, 500 μL blebs solutions were sent into the flow chamber at 100 μL/min. The solutions were circulated in the system until desired values of Δf and ΔD were reached indicating surface coverage of adsorbed blebs. Then the system was rinsed with PBS buffer for 10 minutes to wash out excess blebs. 300 μL of 99.5 mol% POPC, 0.5 mol% PEG 5000-PE liposome solution was then pumped into the flow chamber at 100 μL/min until Δf and ΔD reached steady state. PBS buffer was then sent through the system to wash the bilayer to achieve stabilized final frequency and dissipation shifts.

3.2.6 Tracking the Motions of Individual Membrane Proteins

Bleb bilayers were imaged using total internal reflection fluorescence microscopy (TIRFM) on an inverted Zeiss Axio Observer.Z1 microscope with an α Plan-Apochromat 100x oil immersion objective. Samples were excited using a solid-state laser at 488 nm excitation wavelength. A Laser TIRF 3 slider (Carl Zeiss, Inc.) was used to control the incidence angle at ~ 69° ensuring total internal reflection and generating an evanescent wave around 100 nm thick. The laser light was filtered by a Semrock LF488-B-ZHE filter cube and sent to an electron multiplying CCD camera (Hamamatsu ImageEM C9100-13, Bridgewater, NJ).

Acquired images were analyzed using MATLAB (Mathworks) and ImageJ (NIH). A custom detection method was used to achieve high sensitivity to enable accurate tracking. This method determined particle locations based on pixel clusters that meet an intensity cutoff. Full sample trajectories were found and calculated using in-house scripts based primarily on the "Diffusing-

Spots" tracking methods described by Smith[226] (details can be found in Tracking algorithm and trajectory analysis below). Briefly, this method weights candidate particle positions based on their intensity, change in intensity from the previous frame, and displacement from the previous frame to find the best match for each trajectory. The algorithm we used includes criteria for removing immobile particles, rapidly diffusing particles, and overlapping particles for which particle identity is lost from the final diffusivity analysis. Only particle trajectories that last for at least 20 frames were used in the analysis to minimize noise. Parameters of the model were adjusted to achieve the best possible tracking fidelity. To verify accuracy of the methods, some individual trajectories were semi-manually tracked with computer assistance for comparison using the open-source SpeckleTrackerJ plugin for ImageJ.

A variety of methods for bilayer single particle tracking (SPT) analysis have been described previously in the literature[59,227–230]. We have chosen to use the moment scaling spectrum (MSS) analysis over the mean squared displacement analysis in this work as it is appropriate for the type of anomalous diffusion observed in this system and provides a quantitative value for the mode of motion, with less error for the diffusion coefficient[230,231].

3.2.7 Tracking Algorithm and Trajectory Analysis

Linking of trajectories was performed by finding maximizing value of $w_t = w_i f_i + w_{\Delta i} f_{\Delta i} + w_d f_d$ (Eq. 3.1) among all candidate particles in each frame. Weighting values used were: $w_i = 0.05$, $w_{\Delta i} = 0.05$, $w_d = 0.9$. Equations for each criteria are given as:

$$f_i = e^{\left(\frac{I-\langle I\rangle}{\langle I\rangle - I_{bg}}\right)}$$
$$f_{\Delta i} = e^{\left(\frac{-\Delta I^2}{2\sigma_{\Delta I}^2}\right)}$$
$$f_d = e^{\left(\frac{-d^2}{2\sigma_d^2}\right)} \qquad \text{(Eq. 3.2)}$$

In these equations, I represents the intensity of the particle, I_{bg} is the background intensity

averaged over all frames, ΔI is the change in intensity from the previous frame and d is the displacement from the previous frame. Particle candidates are only accepted into trajectories if they have $w_t > 0.7$.

Moment scaling spectrum analysis is performed on each trajectory j individually. Let M be the length of the trajectory, n be the frame number, Δn be the frame step displacement (in this paper, we limited Δn to $M/4$ to limit error[231]), x be the position of the particle, p be the moment order, and $\|\cdot\|_2$ be the Euclidean norm. First, the displacement moments μ are calculated as

$$\mu_p = \frac{1}{M_j - \Delta n} \sum_{n=0}^{M_j - \Delta n - 1} \left\| x_j(n + \Delta n) - x_j(n) \right\|_2^p \qquad \text{(Eq. 3.3)}$$

for p values from 1 through 6. Each moment follows a power law where $\mu_p \; \alpha \; \delta t^{\gamma(p)}$. The exponential factors, $\gamma(p)$, are determined by a linear regression through $log\ (\mu_p)$ vs $log\ (\delta t)$. If the diffusion process is strongly self-similar, the moment scaling spectrum, i.e. $\gamma(p)$ vs. p, will be linear with a slope defined as β which quantifies the type of diffusion. Species with β values near 0.5 are exhibiting normal diffusion, $0.5 < \beta < 1$ are superdiffusive and $0 < \beta < 0.5$ are subdiffusive. The diffusion coefficient D is determined from the second moment ($p = 2$), since

$$\mu_2 = 4D\delta t^{\gamma(2)}. \qquad \text{(Eq 3.4)}$$

It follows that D can be found from the y-intercept y_0 of $log\ (\mu_2)$ vs. $log\ (\delta t)$ through the relationship

$$y_0 = \log(4D). \qquad \text{(Eq. 3.5)}$$

3.2.8 Enzyme Accessibility Assays for the Determination of Protein Orientation in Cell Blebs and in Planar Supported Bilayers

Enzyme (either 300 U/mL of Thrombin (Sigma) for probing accessibility to the N-terminal Neon domain of P2X2-Neon or 100 μg/mL of Proteinase K (Ambion) for probing accessibility

to the YFP domain of the GPI-YFP protein) was added to 100 mL samples of either adsorbed blebs or bleb bilayers on the glass slides. Images of several regions of the surface were recorded at 10 min intervals to capture the enzymatic action. As the enzyme cleaved the protein, the fluorescent fusion protein domains were no longer attached and could diffuse out of the evanescent field resulting in a loss of fluorescence at the surface of the bilayer or bleb. Particles were counted and a percent change compared to control samples without enzyme was calculated. From this information, we can infer the orientation of proteins in the bilayer and blebs by their susceptibility to enzymatic cleavage, as will be described extensively in the *Results and Discussion* section.

3.3 RESULTS AND DISCUSSION

3.3.1 Verification of Bleb Rupture into Planar Bilayers

Harvested blebs were directly incubated on glass substrates. Blebs generally did not spontaneously rupture to form supported bilayers on their own, but required addition of fusogenic lipid vesicles, as verified using quartz crystal microbalance (QCM) measurements and by direct observation of fluorescent species diffusing from ruptured blebs. QCM with dissipation detects bleb rupture as a change in frequency and dissipation from the initial adsorbed bleb state to that of the final bleb bilayer. In Figure 3.2A we compared the formation of a bilayer formed from only fusogenic POPC-PEG5k vesicles (left) with that formed from blebs and fusogenic vesicles (right). In both cases, it is the fusogenic lipid vesicles that cause rupture and bilayer formation as evidenced by an increase in frequency and simultaneous decrease in dissipation. As vesicles rupture they expel their luminal water to become less massive and more rigid[118]. In the bleb bilayer case, the rupture step happens on a much longer time-scale of around 30 min compared with 1 min for fusogenic vesicles on their own. From the QCM data, the rupture

process of lipid vesicles appears to initiate the much more stable blebs to rupture. The final frequency of the POPC-PEG5k bilayer is -33 Hz (matching well to Kaufmann's results[232]), while that of the bleb bilayer is -50 Hz, aligning with the expectation that the bleb bilayer is more massive due to the additional protein content in the bilayer.

A possible alternative interpretation is that some blebs desorb from the surface during bilayer formation, and the mass increase over the POPC-PEG5k bilayer is due to residual adsorbed unruptured blebs. While it is possible that some blebs never rupture, we confirm that most blebs do rupture and deliver protein to the SLB using two direct visualization methods. First, we label blebs with membrane-intercalating fluorescent probes prior to rupture to visualize the rupture process in real time, and second, we track fluorescently-labeled membrane proteins that are released into the SLB upon bleb rupture. Both of these experiments confirm the formation of contiguous planar bilayers from the ruptured cell blebs. The membrane-intercalating probe experiment is described next, while discussion of the protein tracking experiments is described later in the *Results* section.

To observe and verify cell bleb rupture and planar bilayer formation as it occurs, a membrane-intercalating probe, octadecyl rhodamine B (R18), was incubated with intact blebs for 30 mins. Excess, free R18 was removed from the bleb solution using a G25 spin-column. The R18 incorporated into the bleb membranes is a reporter for lipid mobility, and its spreading is indicative of bleb rupture. In the first step, labeled blebs were incubated with the glass support. A laser was focused to a ~ 20 μm diameter spot on the surface of adsorbed blebs and used to bleach the R18 molecules. No recovery of fluorescence was observed from the adsorbed blebs, indicating that a planar bilayer had not yet formed. Next, unlabeled fusogenic lipid vesicles, either POPC-PEG5k or POPC, were added.

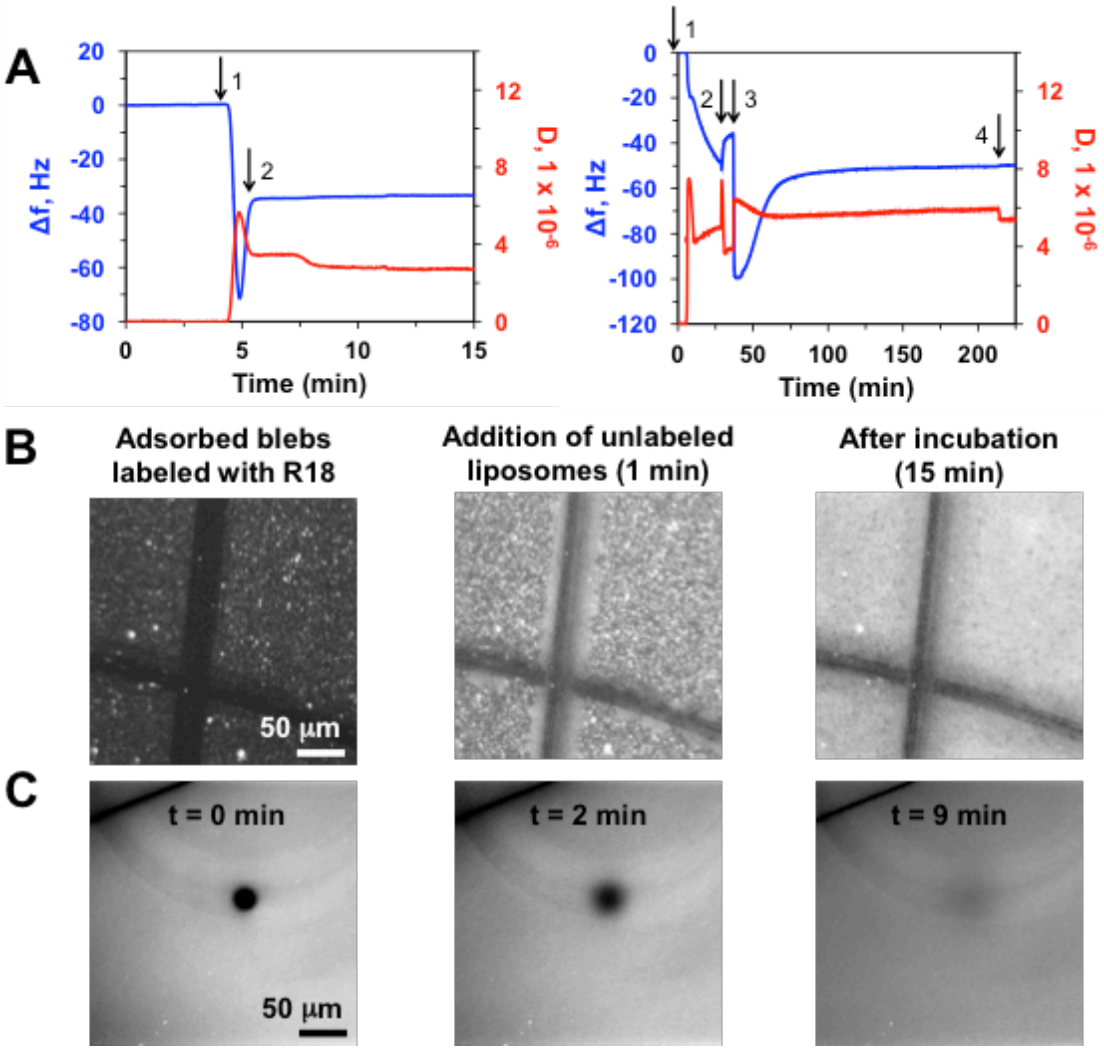

Figure 3.2. Characterization of bleb rupture process. A) Left, a QCMD frequency and dissipation trace for POPC-PEG lipid vesicle adsorption and lipid bilayer formation. Vesicles are added (step 1) and bilayer forms quickly as seen by the sharp increase in frequency and decrease in dissipation. After bilayer formation (step 2), excess vesicles are rinsed away. On the right, the trace is shown for HeLa bleb rupture. Initially, blebs were injected into the system (step 1) and allowed to incubate for ~30 minutes before being rinsed (step 2). During rinsing the frequency decreased, indicating loosely associated blebs were rinsed away. Fusogenic liposomes were then added (step 3) resulting in a rupturing process to form a bleb bilayer and excess vesicles were rinsed away (step 4). B) Fluorescent images of bleb bilayer formation process. Initially R18 signal in blebs was isolated to adsorbed bleb positions. When fusogenic vesicles were added, they triggered rupture of adsorbed blebs into bleb bilayer. During this process, the R18 was able to diffuse laterally and spread out within the bilayer. C) R18 signal from the bleb bilayer is bleached with a laser and recovery is observed. The resulting FRAP diffusivity is 0.3 $\mu m^2/s$ (see Supplemental for FRAP fitting).

For both cases, the blebs began to rupture and form a bilayer within minutes. SLB formation was indicated by spreading of the R18 dye from the original punctate spots of the intact blebs to a fully fluorescent surface (Figure 3.2B). After laser-bleaching this surface, recovery of fluorescence was observed (Figure 3.2C). Diffusivity of R18 molecules was 0.30 ± 0.03 $\mu m^2/s$ in the bleb bilayers, using either POPC or POPC-PEG5k vesicles, so the PEG appears to be inconsequential to the lipid diffusion in these bilayers.

3.3.2 Membrane protein integration into SLBs via blebs

HeLa cells expressing P2X2-Neon or GPI-YFP were observed using brightfield and fluorescence microscopy and determined to be at adequate densities and expressing adequate levels of target protein. Blebs derived from these cells were incubated on glass coverslips and observed using 100x TIRF microscopy. Bleb density and protein concentration in the bleb bilayer can be controlled by dilution of blebs in a consistent manner since we found batch-to-batch variability of bleb yields to be low (see Supporting Information for QCMD data). After adsorption of blebs and subsequent addition of fusogenic, PEGylated vesicles, it was possible to

watch bilayer formation through the radial spreading of species originating from the blebs into the surrounding SLB.

Sufficient time (at least 30 minutes) was given to allow for complete bilayer formation prior to rinsing any loosely associated blebs or lipid vesicles and quantitatively tracking membrane species within the bilayer. An image series was taken at various positions for each bleb SLB. Acquisition settings were chosen to maximize signal while minimizing photobleaching. For these samples an exposure time of 50 ms was used with a laser power of 0.6 mW. A sample tracking analysis for GPI-YFP and P2X2-Neon is shown in Figure 3.3.

Trajectories were mapped following a cost-minimizing function that used the particle locations and intensities to optimize linking across the sample for the duration of the image series (Fig 3 A,B,E,F). The trajectory data was analyzed using the slope of the mean squared displacement (MSD) to determine diffusivity, D, and the moment scaling spectrum (MSS) analysis pioneered by Ferrari[230] to quantify the mobility via a parameter, β. Initially, moments of displacement are determined for each trajectory and the slope of the plot of moment scaling factors, β, describes the type of motion for the trajectory (Fig. 3 D,H). Diffusion modes can be grouped as follows: $\beta < 0.4$ as confined diffusion, $0.4 \leq \beta \leq 0.6$ as quasi-free diffusion and $\beta > 0.6$ as convective diffusion. Particles that are confined to an area smaller than the maximum observed displacement for immobile fluorescent beads in our system are considered immobile[227]. The single particle analysis is useful when there is not enough fluorescent material to carry out ensemble diffusion measurements and provides an additional level of detail for individual proteins, important when tracking in heterogeneous environments and probing the local nature of the membrane.

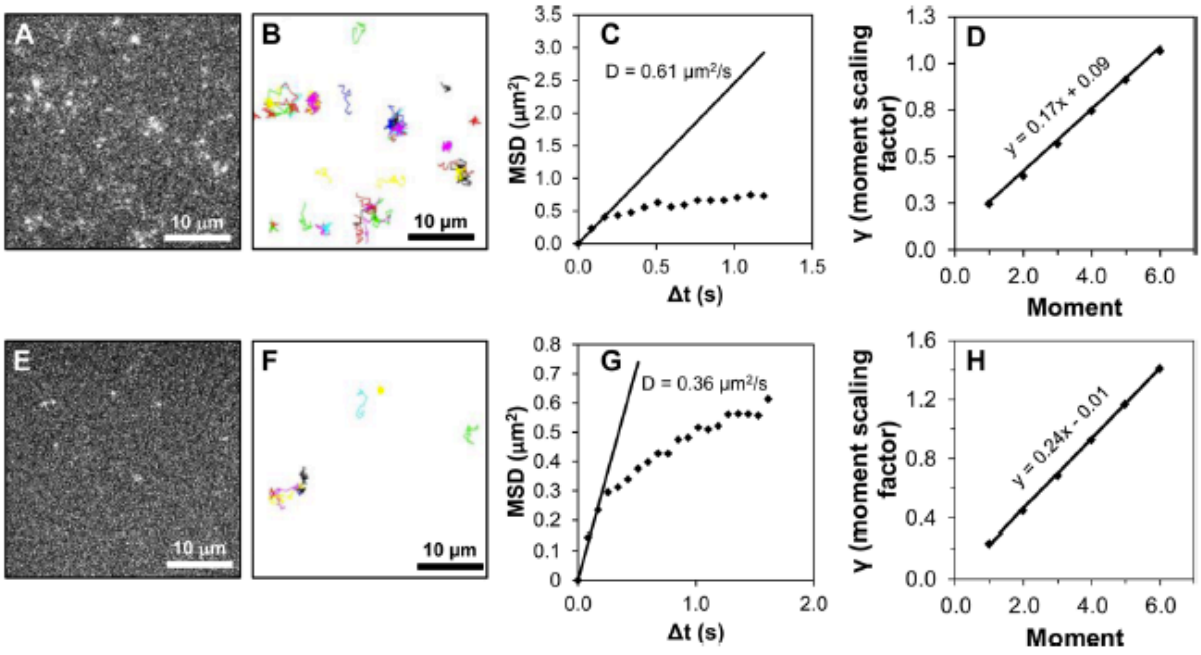

Figure 3.3. GPI-YFP fluorescent proteins tracked on bleb bilayer membrane and analyzed according to the moment scaling spectrum in A-D. A) First frame of fluorescent image of GPI-YFP bleb bilayer. B) Trajectories of GPI-YFP diffusion in the bleb bilayer (same region as A). C) Example trajectory second moment analysis. The diffusion coefficient can be found from the y-intercept (see Eq. 3.5). D) Plot of moment scaling factors. The slope of this plot, β, indicates the type of particle motion for this trajectory is subdiffusive. Corresponding figures are shown for P2X2-Neon bleb bilayers in E-H.

By compiling the diffusion coefficients for collected trajectories, we can determine the ensemble diffusivity from fitting to a cumulative distribution function described by a gamma distribution (Eq. 3.1) where $k\theta$ represents the average diffusivity and $k\theta^2$ is the variance[59,125].

$$\frac{1}{\Gamma(k)}\gamma\left(k,\frac{\theta}{x}\right) \qquad \text{(Eq. 3.1)}$$

This can also be represented as the probability density function, which overlays the diffusion coefficient histogram well (Fig 3.4). Additionally, we determine the percentage of mobile particles from the total particles observed. With this analysis, we have measures comparable to the standard bilayer diffusivity method of fluorescence recovery after photobleaching (FRAP). To ensure our results for the bleb bilayers were reliable, we compared results of single molecule tracking analysis with FRAP results for a peripheral protein probe.

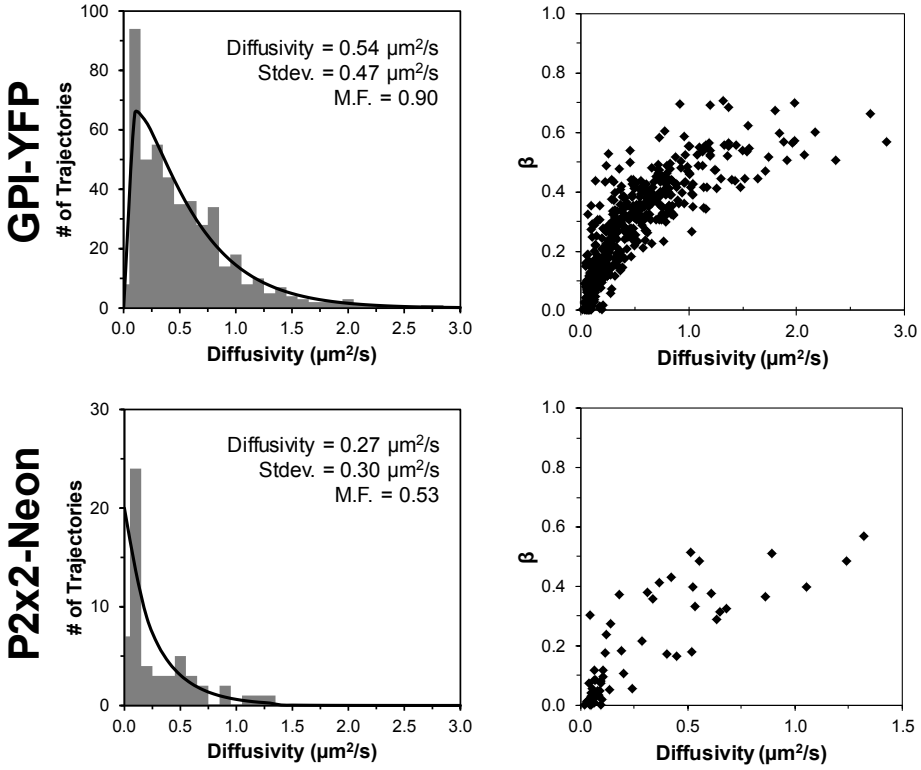

Figure 3.4. Diffusion coefficient histograms and β-plots for GPI-YFP and P2X2-Neon in bleb bilayers. Diffusion coefficients of membrane proteins are shown for GPI-YFP and P2X2-Neon compiled from several tracking videos. Each distribution was fit to a gamma distribution from which average diffusivities and standard deviations were found (left). Mobile fractions were calculated as the fraction of trajectories meeting a mobility criterion described in the text. Plots of β vs. diffusivity quantify the type of motion associated with each trajectory (right).

In initial control experiments, we tracked protein diffusion in uncushioned POPC bilayers. P2X2-Neon was completely immobile in an uncushioned POPC bilayer, while GPI-YFP was 96% mobile. Next, we carried out trajectory analysis for bleb bilayers with either GPI-YFP or

P2X2-Neon to characterize the diffusion of these membrane proteins in cushioned POPC-PEG5k bleb bilayers. Figure 4 shows the histograms of diffusion coefficients for both proteins as well as plots of the corresponding mobility parameters. For both proteins, more than half were mobile, with GPI-YFP proteins at 90% mobility while P2X2-Neon was 53% mobile, verifying the critical requirement of the PEG cushion for providing enough space for the P2X2-Neon extramembranous domains. GPI-YFP had an average diffusion coefficient of 0.75 $\mu m^2/s$ while P2X2-Neon was 0.51 $\mu m^2/s$.

According to the Saffman-Delbrück approximation, which has been upheld by recent literature on membrane protein diffusivity in black lipid membranes[233] and giant unilamellar vesicles[234], the diffusion coefficient scales inversely proportional to the logarithm of the membrane-embedded radius of the protein. As expected, the P2X2-Neon protein diffused slower than GPI-YFP because of its significant transmembrane domains that increase its drag[235]. Particularly, the radius of GPI-YFP is approximately 0.4 nm while P2X2-Neon is 3.3 nm from the crystal structure of P2X4[225], so the predicted diffusivity ratio between GPI and P2X2 from Saffman-Delbrück (using approximate parameters from Ramadurai et al[234]) is about 1.46, matching very closely to the ratio of the diffusivities we found here of 1.47. It is important to note that diffusivity measurements vary with the system being used and components included in the membrane so absolute values may differ, but our results still fall within the expected range from 0.01 – 1 $\mu m^2/s$ based on similar measurements reported in literature[130,131,236].

In POPC-PEG5k supported lipid bilayers, we found R18 diffused at 0.41 ± 0.14 $\mu m^2/s$ via FRAP experiments. R18 is typically a slow diffusing probe with between 1/3 to 1/10 the diffusivity of other membrane lipid probes[237,238]. When cell material from blebs is present in the cushioned bilayer, R18 diffusion is reduced by about 25% to 0.30 ± 0.02 $\mu m^2/s$. For proteins in

bleb bilayers, most β values fall in the range of anomalous subdiffusive behavior with 73% of GPI-YFP and 87% of P2X2-Neon trajectories having β values less than 0.4. Thus the additional material in the bilayer delivered during bleb rupture impacts diffusion of both protein and lipid probes. It is expected that the diffusion would be slowed and present confined behavior in a bleb bilayer compared with a purely artificial membrane because of the presence of a variety of membrane heterogeneities.

The spread in b values from the SPT experiments indicate that heterogeneities exist. These may result from unruptured vesicles; membrane heterogeneity (e.g., domains of differing compositions); and immobilized or cross-linked proteins. Each of these factors influences the diffusion of species in the membrane. Unruptured vesicles prevent bilayer formation at their location, creating voids in the SLB. These voids reduce the total free area the probes have to diffuse around, thus leading to subdiffusive behavior. We believe that this effect is minor given the uniform spread of R18 dye in the bleb bilayer and the near full recovery in fluorescence following photobleaching as observed by florescence microscopy.

Membrane heterogeneity can arise if there are patches of plasma membrane not well mixed with the surrounding lipid bilayer, which could reduce diffusion due to different local viscosities. Alternatively, membrane heterogeneity could arise from the non-uniform distribution of PEG resulting in cushioned bilayer domains and uncushioned domains[139]. Both of these situations could explain the confined, subdiffusive protein diffusion we observe. However, because the GPI protein also shows a significant anomalous diffusive behavior with a very high mobile fraction, and they are located predominantly in the upper leaflet (details provided in later section), we believe that the more likely cause of the confinement is due to the heterogeneity of the plasma membrane itself. Studies of membrane protein diffusivity in cell membranes show that a large

fraction of proteins, usually more than half, show confined motion[239], thus this critical feature of "real" cell membranes appears to be preserved in this platform, even though it is "diluted" with extra lipid material from the fusogenic liposomes.

Protein immobilization results when the extramembranous parts of the protein come into contact with the underlying support, as observed when non-PEGylated fusogenic vesicles are used to rupture blebs on the support. We note that the PEG cushion that should result from the PEGylated fusogenic vesicle formulation used here is expected to be on the order of ~ 6 nm, based on deGennes' theory[138]. The neon green label of the P2X2 on the cytosolic side is about 4 nm long. On the other side of the membrane, the extramembranous P2X2 loop extends 7 nm. With protein oriented such that the neon green label is between the bilayer and substrate it is possible that some proteins are not fully fluidized and still able to interact with the glass surface; however, if the proteins are inverted in the bilayer, the much larger extracellular domain would contact the support and the P2X2 receptor would not be fluidized at all. While it is appealing to consider using higher molecular weight PEGs to accommodate larger proteins, we note that increasing the PEG length too much can reduce the fusogenicity of the vesicles and may also protrude past the protein and possibly hinder its interaction with extracellular species. To rule out protein inversion as a significant cause of immobilization, we conducted experiments to determine the orientation of proteins in the SLB derived from cell blebs (next section). We should point out that any immobile protein obstacles will act as barriers that hinder the free diffusion process as well as a give a hydrodynamic penalty, also leading to anomalous diffusion behavior we observe. A final possibility to consider is that some of the proteins are cross-linked together by the blebbing chemicals. We also investigated this possibility and report our findings in a later section.

3.3.3. Orientation of Membrane Proteins in Blebs and SLBs

Determining the orientation of membrane proteins in our system is useful in two ways. First, if there is little leaflet scrambling during the rupture process, one could imagine designing experiments based on probing either the extracellular or cytosolic side of the plasma membrane, increasing the value of the this system as a cell membrane mimic. Second, this information can help us characterize the protein diffusion in the bilayer system and determine the extent to which extramembrane domain interaction with the support could be playing a role.

The vesicle rupture process is still not well understood. There are several theories on the mechanism of bilayer formation from lipid vesicles. Two important implications, the directionality and degree of lipid scrambling in the bilayer, are controversial. Because the rupture process is not known, it follows that the orientation of membrane proteins in the bleb SLB after rupture is also unknown. Here, we determine orientation in blebs and resulting bleb bilayers as a first step toward characterization of the blebbing process and the vesicle rupture mechanism. We expect the orientation of proteins in blebs to be the same as in the cell membrane because blebs arise as outward protrusions of the cell membrane, encapsulating cytosol in their lumen[217]. To verify this, we adsorbed blebs to glass slides prior to addition of enzymes to cleave accessible protein domains in a manner similar to the fluorescence protease protection assay described by Lorenz et al[240]. Protein domains on the outside of the blebs are accessible, while luminal domains are inaccessible to the enzymes. For GPI-YFP, Proteinase K was added which will cleave any accessible protein releasing the YFP from its GPI anchor. Since GPI-linked proteins are monotopic peripheral membrane proteins, GPI-YFP will only be cleaved by Proteinase K if it is on the outer leaflet of the bleb membrane. For P2X2-neon, we added thrombin, a specific protease that can cleave a thrombin cleavage site inserted between P2X2 and the neon fusion

protein at the N-terminus of the protein. In both of these cases, a signal drop reports on when proteins are cleaved as the fluorescent fusion proteins diffuse out of the TIRF field, and can be used to interpret protein orientation. To control for photobleaching effects, we performed side-by-side experiments without enzyme.

A significant drop in signal of 74% was observed for GPI-YFP blebs (99.9% confidence compared to control), but no significant change in signal was detected for P2X2-Neon blebs during this 40 minute assay (Fig. 5). This indicates that the GPI-YFP proteins are on the surface of the blebs. Since the GPI-YFP proteins are located on the outside of the cell membrane this means most of the proteins have the same orientation in the blebs. The thrombin site on the P2X2-Neon protein is inaccessible in the blebs, indicating it is in the lumen, matching its cytosolic location in cells. Bleb orientation indeed mimics orientation in the cell membrane for both of these proteins, as expected.

To determine the final orientation of proteins in our SLBs, we used the same enzymatic assays on bleb SLBs. In this case, the enzymes cannot access protein domains that are underneath the bilayer. GPI-YFP signal dropped for almost all particles at the first time point after addition of enzyme. The percent change of 95% was significantly different than a control without enzyme to 99.9% confidence. P2X2 signal did not change appreciably compared to control, although in both control and enzyme tests, a slow signal drop over the time course of the experiment was observed. This drop may be attributed to photobleaching, as a similar drop was observed in all control experiments.

Because the result for P2X2 was derived from a lack of significant change in particle counts after addition of thrombin, we performed an additional control to verify thrombin activity. Following a similar procedure for scrambling proteoliposomes presented by Pace et al[216] we

found that thrombin could cleave the neon fusion protein off of the P2X2 protein constructs in a population of P2X2 proteins in bilayers created from scrambled blebs. We attribute this population as having the inverted orientation. The results for the scrambled bleb experiment can be found in the Supporting Information.

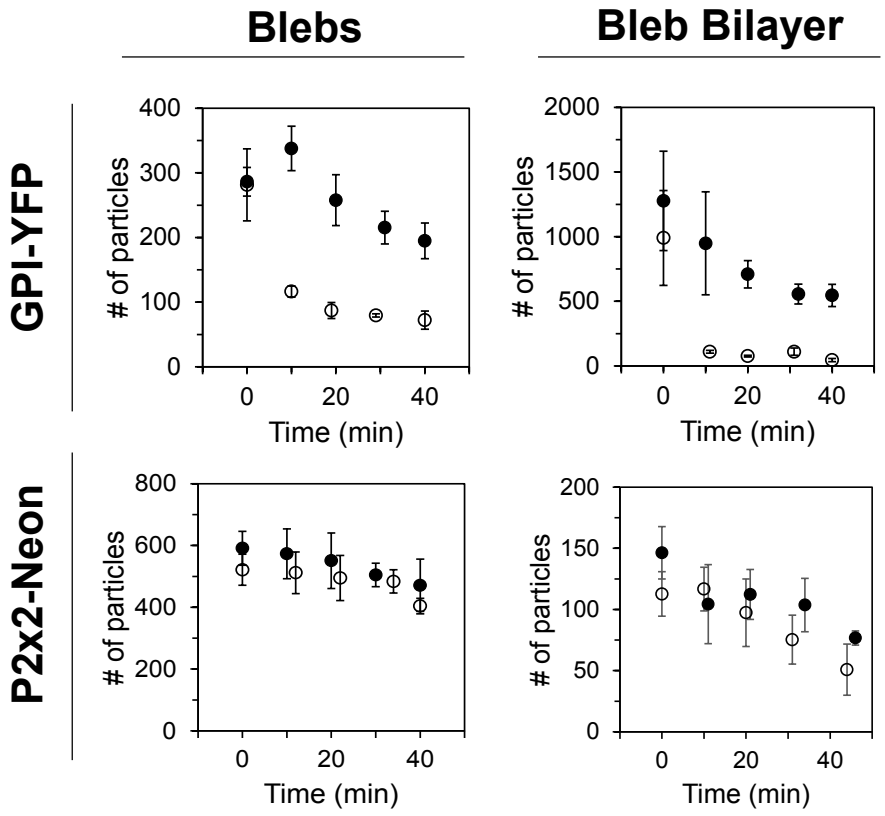

Figure 3.5. Determination of protein orientation through fluorescence enzyme accessibility assays. Solid circles indicate control experiments; empty circles indicate experiments with enzyme added. Bleb and bilayer orientation were determined for GPI-YFP and P2x2-Neon membrane proteins. The signal change in GPI-YFP shows a sharp drop after addition of proteinase K with percent change of about 74% for intact blebs and 95% for bilayer. P2X2-Neon signal after thrombin addition does not change significantly compared to control. GPI-YFP was accessible to enzyme in both blebs and bilayers, but the fluorescent N-terminus of P2X2-Neon was not. This indicates that GPI-YFP is predominantly located in the outer leaflet of the blebs and upper leaflet of the SLB, and P2X2-Neon is oriented with its termini extending from the inner leaflet of blebs and large extramembranous loop above the SLB.

For both GPI-YFP and P2X2-Neon, bleb bilayer orientation matches that of the cell and the blebs, i.e. the extracellular domains are accessible to the bulk and cytosolic domains are not. We conclude that blebs appear to rupture with the luminal sides down towards the glass (see

schematic in Fig. 1). This "parachute" mechanism may result in a small patch of the bleb inverting where it initially contacts the substrate, but we cannot resolve this with our methods. Literature shows that factors that support this mechanism include high surface potential, vesicle crowding and vesicle cargo which may play a role in our system. Interestingly, the bleb lumen may hold various soluble proteins as cargo which could adsorb to the surface underneath the bilayer during rupture. These adsorbed proteins could provide additional passivation of the surface and further improve the membrane protein mobility in an analogous manner to Diaz et al's[133] BSA passivation layer approach. However, large proteins could also adversely affect the bilayer and may be a source of the anomalous diffusion behavior we observe.

As mentioned above, bilayer formation is an unclear process and while both of these membrane proteins demonstrated the same orientation after rupture, it may not be the case for all membrane proteins or for bleb lipids. We performed an antibody binding experiment on an endogenous transferrin receptor protein in our bleb bilayers and found that it too displayed outward-up orientation, though we could not quantify the extent using the antibody binding approach alone. This data further supports the parachute mechanism (see Supporting Information for additional experimental details). Importantly, this experiment also shows that the PEG cushion does not prevent binding of ligands to membrane proteins. Additional experiments are required to determine the orientation of other bleb constituents, particularly lipids, and the destination of luminal cargo molecules, to develop a more complete picture of the rupture process. However these studies are not as straightforward to carry out and interpret due to experimental limitations, and thus are beyond the scope of this work.

3.3.4 Effect of chemically induced blebbing on protein mobility in SLBs

Production of cell membrane blebs using chemical induction is an established technique for harvesting and studying membrane proteins in vesicles[241–243]. However for their use in SLBs it is important to ensure the chemicals used for blebbing do not adversely affect the protein quality particularly in a sensitive application such as tracking mobility. Formaldehyde (FA) (at 4%) is a typical non-specific cross-linking reagent, and dithiothreitol (DTT) may reduce disulfides and palmitoylated cysteines, which may lead to differences in phase partitioning[53,94]. Additionally, chemical treatment has been found to alter the phase behavior and even compositions of bleb membranes[103]. Thus, to test the effect of chemical induction on bleb bilayer quality, we prepared YFP-GPI bleb bilayers using three different bleb preparation conditions: serum-starved (i.e. chemical-free) blebbing; standard chemical induction at 0.075% FA (2mM DTT, 25mM FA); and high chemical induction at 1.5% FA (40mM DTT, 500mM FA) (Table 1). The amount of formaldehyde at the high chemical induction case is still much less than the 4% used for a standard fixation protocol, but still may be enough to cause some localized crosslinking[244,245] and a commensurate reduction in protein mobility due to increased size.

Table 3.1. Comparison of GPI-YFP protein mobility and diffusivity in bleb bilayers for three different bleb induction processes: chemical-free blebbing, 25mM FA 2mM DTT chemical induction (0.075% FA), and 500mM FA 40mM DTT (1.5% FA) chemical induction from HeLa cells. Trajectories are grouped by diffusional modes as either: confined, quasi-free or convective.

		Confined ($\beta < 0.4$)		**Pseudonormal ($0.4<\beta<0.6$)**		**Convective ($0.6<\beta$)**	
Treatment	% Mobile	% of Trajectories	Diffusivity ($\mu m^2/s$)	% of Trajectories	Diffusivity ($\mu m^2/s$)	% of Trajectories	Diffusivity ($\mu m^2/s$)
GPI-YFP Serum Starved (0% FA)	72	84.7	0.54	14.0	0.73	1.3	1.02
GPI-YFP 25mM FA 2mM DTT (0.075% FA)	95	75.7	0.69	22.9	0.97	1.4	1.26
GPI-YFP 500mM FA 40mM DTT (1.5% FA)	70	83.5	0.55	16.1	0.80	0.4	1.34

The 0.075% FA condition resulted in a bleb bilayer with very high protein mobility at 95%. Interestingly, both the 0% and 1.5% FA conditions resulted in bilayers with protein mobility around 70%. In the 0.075% FA case, the highest percentage of quasi-freely diffusing proteins ($0.4 \leq \beta \leq 0.6$) was found at 23% vs. 14% and 16% for 0% FA and 1.5% FA blebs, respectively. The diffusion coefficient for GPI-YFP proteins in the pseudo-normal regime was found to be 0.97 $\mu m^2/s$ for the standard 0.075% FA chemically-induced blebs, slightly higher than that of the other two cases as well (0.73 $\mu m^2/s$ for chemical-free and 0.80 $\mu m^2/s$ for 1.5% FA). Similarly, the diffusivity of the confined proteins in the standard chemical case was highest at 0.69 $\mu m^2/s$ as compared to 0.54 $\mu m^2/s$ for chemical-free and 0.55 $\mu m^2/s$ for 1.5% FA chemical induction. In all cases, there was only a very small fraction (<2%) of proteins showing convective or directed motion, potentially reflective of capturing late rupturing blebs, bilayer reorganization or rare unruptured blebs rolling on the surface.

The mobility trend for the 1.5% FA case can be explained as a result of some crosslinking of membrane species causing diffusion barriers or even crosslinking of some YFP-GPI reporter proteins. For the chemical-free case, one plausible explanation for the lower mobile fraction and slightly lower diffusivity is the presence of more unruptured blebs. If the blebs do not fuse into the bilayer, then the proteins within them are immobilized, and the blebs themselves act as barriers to diffusion in the SLB. We hypothesize that blebs formed from serum starving may not be as fusogenic as chemically-induced blebs as a result of their formation process. It is possible that the mechanism of formation is different when not chemically induced, resulting in changes in bleb composition and size. Evidence to support that bleb formation could be different depending on the inducing method comes from light scattering measurements that show chemical-free blebs are smaller, with a peak size of about 125 nm, compared to about 200 nm for

chemically-induced blebs (see Supporting Information). We note that while the mobile fractions from the chemical-free blebs are not as high as those from the standard chemically-induced blebs (0.075% FA); they are still high enough to deliver protein to bilayers when blebbing chemicals could adversely affect the experiment. In conclusion, using the 0.075% FA blebbing formulation does not appear to crosslink proteins or adversely affect membrane protein diffusivity in the final bleb bilayers. We would like to point out that alternative bleb preparations exist, e.g. *N*-ethyl maleimide (NEM), but examining them thoroughly is beyond the scope of this work. Future studies will report on these results.

3.4 CONCLUSION

The membrane protein platform described here using cell blebs to deliver species directly to a supported lipid bilayer is widely-applicable to the study of membrane proteins derived from various mammalian cell hosts, and to membrane spanning proteins as well as peripheral proteins. In this work, we addressed several of the chief concerns of membrane protein incorporation into SLBs – the immobilizing interactions of the extramembranous domains of the proteins with the support and maintaining protein orientation. Our use of PEGylated lipids in the rupture vesicles provided enough of a cushion to retain mobility for greater than 50% of the multi-pass transmembrane proteins tested. However, this particular cushion may not be universal for all proteins and we are currently testing modified cushions to further improve this technique. Tethered cushions may provide more even spacing at the cost of some additional bilayer resistance[125]. Including a passivation layer on the glass surface may also improve the mobile fraction by preventing irreversible binding of membrane proteins[133]. Many other cushioning options exist and deserve further study[130,131,246,247].

The techniques for single particle tracking and theory for membrane protein dynamics have seen much development recently. Until now, most of the work has been performed either on simplified model probes in artificial membranes or with difficult to interpret cell-based measurements of real membrane proteins. This platform enables a crossover of the two methods, bringing membrane proteins to the artificial membrane system and opening up a new avenue of study using planar characterization tools. To our knowledge, this is the first planar bilayer platform to demonstrate mobility and proper orientation of a truly integral transmembrane protein of this size, derived directly from cell source without reconstitution.

The cushioned bleb bilayer provides a simple way to build more biological complexity into the supported lipid bilayer model membrane system and addresses the key challenge of membrane protein reconstitution. This promotes the use of the rich SLB and SPT toolset to answer important elusive questions about membrane proteins. While the focus of this work was to characterize the quality of the membrane protein platform by measuring diffusion and orientation of proteins, there are many studies in the directions of fundamental protein function and biosensing applications that could benefit from using this platform. For example, combining this technology with bilayer patterning and other surface assays, it may be possible to reveal information about membrane protein compartmentalization, interactions with lipid rafts and proteins, oligomeric state kinetics[248] and other stochastic level dynamic processes due to the capabilities of SPT methods. We foresee use of this platform as a backbone to enable modular on-chip assays for membrane proteins. For example, after bleb bilayer formation, proteins could be separated by charge[177], separated by lipid phase affinity[206], or screened for binding interactions with drug candidates[207].

3.5 ACKNOWLEDGEMENTS

This chapter was published in its entirety in "Membrane Protein Mobility and Orientation Preserved in Supported Bilayers Created Directly from Cell Plasma Membrane Blebs" in Langmuir[249]. Mark J. Richards was the first author and the co-authors include Chih-Yun Hsia, Huma Haider, Julia Kumpf, Toshimitsu Kawate, and Susan Daniel. Chih-Yun Hsia has contributed to the following work: *Verification of bleb rupture into planar bilayers, membrane protein integration into SLBs via blebs, membrane protein integration into SLBs via blebs and orientation of membrane proteins in blebs and SLBs*. The authors would like to thank Barbara Baird and David Holowka of Cornell University for providing the pYFP-GPI-N1 plasmid and related reference material. We thank the National Science Foundation (grant CBET-1149452) for supporting the work presented in this article.

CHAPTER 4

A MOLECULAR COMPLETE PLANAR BACTERIAL OUTER MEMBRANE PLATFORM

4.1 INTRODUCTION

The bacterial outer membrane (OM) is a distinctive feature of gram-negative bacteria[250,251]. It forms a semi-permeable barrier that protects the bacterium from environmental attack, allows essential nutrients to cross the membrane to sustain life, and plays a major role in the virulence of pathogenic bacteria. The ability of the OM to prevent the entry of many antibacterial agents, especially hydrophobic compounds, is closely related to its structure. The OM is highly asymmetric, with the outer leaflet mainly composed of lipopolysaccharides (LPS) and the inner leaflet consisting of phospholipids[252,253]. The tightly packed LPS molecules on the outer leaflet give the bacteria structural integrity and form a stable barrier that resists antibacterial penetration[250,254]. In addition to the lipid content of the OM, proteins embedded in this membrane also play important biological functions, such as omptins (*e.g.*, ompA) that facilitate signal transduction through the cell envelope[255] and pore-forming toxins (*e.g.*, ClyA) in the OM that perforate and disrupt host cells[256]. The importance of the OM in these and other important biological processes urges the development of tools to (1) understand fundamental biological events occurring in the OM[257], and (2) study the action of new antibacterial drugs against OM components[258,259].

To circumvent the experimental complexity imposed by *in vivo* systems, we developed a versatile model system to study bacterial outer membrane molecules in a convenient planar geometry that is compatible with many bioanalytical techniques and high throughput microfluidic devices. Supported lipid bilayers (SLBs), are thin planar bilayers that self-assemble

during lipid vesicle rupture near a hydrophilic surface[260,261], and are one of the most commonly used model systems to study cell membranes[262]. First, SLBs closely resemble cell membranes with the ability to protect the hydrophobic portion of membrane species to preserve their structure and functionality. Second, SLBs are amenable to surface sensing techniques and imaging tools due to their planar geometry, enabling studies of fundamental biological interactions between lipid-lipid, lipid-protein[170], and pathogen-host[36,118,120,261].

Unfortunately, developing a SLB platform that closely mimics the bacterial OM environment is a challenging task for two main reasons. First, it is difficult for negatively charged LPS to undergo vesicle fusion on a bare glass to become a planar sheet. Several strategies have been reported in literature to overcome this obstacle; such as depositing LPS monolayer on alkanethiol-linked gold surface[263], or inducing LPS vesicle fusion on positively charged polymer polyethylenimine (PEI) supports[264]. However, these approaches employ surface modification to facilitate the formation of LPS monolayer/bilayer, which may result in artifacts due to the strong electrostatic/hydrophobic interactions between the modified interface and LPS layer. Alternative methods extract lipid materials from bacterial membranes and reconstitute them into vesicles and supported bilayers[119,265,266]. As a result, these supported bilayers contain a mixture of outer and inner membrane components with no native proteins incorporated. Detergent reconstitution methods are commonly used to generate proteoliposomes, but they may induce denaturation of membrane proteins and loss of function. Finally, cell disruption methods and fractionation of resultant proteoliposomes with sucrose gradients has been used to isolate bacterial inner membrane vesicles and form planar bilayers[267]. In the end, reconstitution methods of any kind highlighted here result in loss of asymmetry of the membrane, which is an important feature of the OM. Hence, we sought to develop a simple and detergent-free method to incorporate

molecularly complete OMs (i.e., containing lipids, LPS, and proteins) into a supported bilayer platform that preserves native asymmetry.

Our approach for creating an OM-mimetic supported bilayer (OM-SB) involves bacterial outer membrane vesicles (OMVs) as the source of OM materials. OMVs are nano-scale vesicles naturally secreted from gram-negative bacteria[268]. OMVs form during cell growth as the OM blebs outward and pinches off resulting in ~20 - 250 nm spheres of OM containing membrane-bound proteins and soluble periplasmic components trapped in their lumens[268,269]. Hence, the composition of OMVs reflects components of the OM and periplasm, for example, soluble proteins, OM proteins, and LPS. OMVs have been linked to a number of important biological processes such as envelope stress[270], virulence[271–273] and removal of antibacterial compounds [274–277].

In this study, we created an OM-mimic platform by inducing OMVs to rupture into planar supported bilayers on glass/SiO_2 supports. Unlike pure liposomes, OMVs are difficult to convert into supported bilayers via spontaneous vesicle fusion due to their high LPS and OM protein content[197]. To induce OMVs to fuse, we adapted a method reported previously by our group to form proteinaceous bilayers from mammalian cell blebs[249]. The resulting OM-SBs were studied in detail, including bilayer property characterization, protein orientation, and an investigation of bilayer formation kinetics using several surface-sensitive techniques: total internal reflection fluorescence microscopy, fluorescence recovery after photobleaching (FRAP), and quartz crystal microbalance with dissipation (QCM-D). Furthermore, we demonstrate using QCM-D that OM-SBs facilitate the evaluation of antibacterial drugs by providing details on mechanical property changes of membranes upon peptide-OM interactions. Using the OM-SB, we probed the antibacterial mechanism of polymyxin B (PMB), a cyclic cationic peptide used for treating gram-

negative bacterial infection and endotoxin. The action of PMB on OM-SB was monitored using QCM-D in real time, and the data was subsequently fit to a theoretical model to quantify the change in mass and viscoelastic properties of OM-SB upon interaction with PMB. Based on the results, we validated that PMB interacts with the OM-SB following a mechanism of action that has been reported in literature [278], supporting that the OM-SB is a suitable mimic of the bacterial membrane surface. However, with QCM-D, additional information can be learned about the changes in bacterial membrane properties (e.g., thickness, viscosity, shear modulus) upon peptide interaction, which we illustrate and report here for PMB. These mechanical properties are important for understanding how the outer membrane is compromised as a first protective layer preceding bacterial inner membrane failure. To our knowledge, this work outlines the only approach to construct a molecularly complete planar bacteria outer membrane (lipids, LPS, proteins, etc.) that preserves the hallmark asymmetry of the structure. By combining OM-SB with the appropriate surface sensing techniques, we illustrate the potential of an OM-SB as a convenient platform to quantitatively measure antibiotic interactions with bacteria membrane surfaces, including disruption kinetics and changes to bacterial membrane properties. Combining OM-SB with microfluidic platforms will enable higher throughput screening of compounds beneficial for future antibiotic design. Beyond thus, such a complete membrane-scaffold could be useful for cell-free studies/applications using expressed membrane proteins in bacterial membranes for myriad technological purposes.

4.2 METHODS

A detailed list of materials and methods used in this study is provided in Appendix A: Fluorescence Microscopy, Preparation of Lipid Vesicles for Formation of Supported Lipid

Bilayers, PDMS Well Fabrication, Characterization of Diffusion in Supported Lipid Bilayers by Flurescence Recovery After Photobleaching (FRAP) and Preparation of glass coverslips used as supports for supported bilayers.

A detailed list of materials and methods used in this study is provided in Appendix B:

QCM-D modeling to detect adsorbed mass on the quartz sensor, OMV size and surface charge characterization, fluorescent labeling of OMVs and liposomes, and Proteinase K susceptibility assays for the determination of ClyA-GFP orientation in OM-SB. Other key aspects are described next.

4.2.1 Preparation of bacterial outer membrane vesicles

OMVs were purified as described in previously published literature[279]. Briefly, the plasmid pClyA-GFP was transformed into the JC8031 hypervesiculating strain of *Escherichia coli* and grown in Luria-Bertani (LB) medium supplemented with chloramphenicol (25 μg/mL) at 37˚C[280]. Protein expression was induced at an OD_{600} ~ 0.5 with the addition of L-arabinose (0.2% w/v) and allowed to grow for an additional 16 hours. Cells were pelleted at 7500x*g* for 20 min at 4˚C and the supernatant was collected and filtered through a 0.02 μm filter. OMVs were then isolated from the filtrate via ultracentrifugation at 141,000x*g* for 3 hours at 4˚C then resuspended in fresh buffer composed of 5 mM phosphate buffered saline (PBS) with 150 mM NaCl at a pH of 7.4, and stored at -20˚C. OMV protein content was quantified via bicinchoninic acid assay (QuantiPro BCA Assay; Sigma) using a BSA protein standard (Sigma).

4.2.2 Quartz crystal microbalance with dissipation monitoring

QCM-D was used to quantify the kinetics of various supported lipid bilayers formation. This technique measures changes of resonance frequency (Δf) and energy dissipation (ΔD) of an oscillating piezoelectric quartz crystal, which is driven by an applied AC voltage. The shift of resonance frequency (Δf) reflects the change of adsorbed mass on the quartz crystal sensor. The fundamental frequency (5

MHz) together with the third (15 MHz), fifth (25 MHz), seventh (35 MHz), ninth (45 MHz), eleventh (55 MHz) and thirteenth (65 MHz) overtones were generated and recorded during measurements. Simultaneously, shifts of energy dissipation (ΔD) were measured, which characterize the viscoelastic properties of the adhered layer to the crystal surface. Please see Appendix B for a detailed description of QCM-D models, including Sauerbrey Model[281], One-layer Voigt-Voinova model[282] and Two-layer Voigt-Voinova model[282].

4.2.2.1 QCM-D experimental setups for supported bilayer formation

All experiments were measured on QCM-D crystals made of silicon dioxide (QSX303, Q-Sense, Sweden) using a Q-Sense E1 (Q-Sense, Sweden) instrument. Before measurements, crystals were cleaned with Milli-Q water and ethanol, and dried with nitrogen gas. Crystals were then cleaned in UV-Ozone Procleaner (Bioforce) for 10 minutes to remove any organic contamination. Note that although the crystals chosen here are the most similar material to the glass slides used in the microscopic experiments, the bilayer formation kinetics observed using QCM-D and fluorescent microscopy may be slightly different due to the variance in the elemental composition of surfaces. Measurements were taken under flow conditions. Solution was pumped into the chamber by Peristaltic pump (Ismatec Reglo Digital M2-2/12, Q-Sense, Sweden). The experimental details are provided below for different bilayer formations:

4.2.3.2 SLB formation on quartz sensors from pure liposomes.

PBS buffer was pumped into the system at a flow rate of 100 μL/min for 5 minutes to collect the baseline of frequency and energy dissipation shifts (i.e. $\Delta f = \Delta D = 0$) of the crystal itself. Afterward, 500 μL of pure liposome solutions were pumped into the flow chamber under 100 μL/min. Then, PBS buffer was sent through the chamber at 100 μL/min to wash the bilayer to achieve stabilized final frequency and dissipation shifts.

4.2.2.3 OM-SB formation on quartz sensors

PBS buffer was pumped into the system at a flow rate of 100 μL/min for 5 min. Thereafter, 500 μL OMVs solutions were sent into the flow chamber under 100 μL/min. The solutions were circulated in the system until desired values of Δf and ΔD were reached. Then the system was rinsed with PBS buffer for 10 minutes to wash out excess OMVs. 500 μL of PEG (5k) 0.5% DOPC liposome solution was then pumped into the flow chamber under 100 μL/min until Δf and ΔD reached steady state. PBS buffer was then sent through the system to wash the bilayer to achieve stabilized final frequency and dissipation shifts.

After measurements, the system was rinsed with 0.1% sodium dodecyl sulfate (SDS) solution, Milli-Q water and ethanol to ensure the removal of any residual materials prior to the next experiment. Air was pumped through to dry the tubing and the flow chamber. The crystal was removed and cleaned by UV-Ozone for 20 minutes and sonicated for 2 hours at 40 °C.

4.2.2.4 Peptide interaction with OM-SB on quartz sensor

To prepare peptide solutions, Polymyxin B sulfate salt (Sigma) was dissolved in PBS buffer at the concentrations of 0.1 mg/ml. Following the formation of OM-SB, peptide solution at desired concentration was added in the system. The solution was flown until the signals stabilized (~ 1hr), and replaced with a buffer rinse to achieve final stable values of frequency and dissipation (~ 30 min). The flow rate was set to 100 μL/min throughout all experiments.

To better understand the action of polymyxin B on OM-SBs, normalized changes of frequency and dissipation at various overtones (3^{rd}, 5^{th}, ..., 13^{th}) upon addition of peptide solution were monitored and fit to a two-layer Voigt-Voinova viscoelastic model. Signals of fundamental resonance, i.e. F_1 and D_1, were discarded since they are rather unstable due to edge effects.[283]

4.2.3 Preparation of lipid vesicles

The lipids used in this study were DOPC (1,2-dioleoyl-*sn*-glycero-3-phosphocholine) and PEG (5K) - PE (1,2-dioleoyl-*sn*-glycero-3-phosphoethanolamine-N-[methoxy(polyethylene glycol)-5000]). Both lipids were purchased from Avanti Polar Lipids (Alabaster, AL). The composition of lipids used was: 0.5 mol% PEG(5K)-PE with 99.5 mol% DOPC. This composition was chosen so that the PEG would exist at (or below when mixed with OMVs) the mushroom-to-brush transition in the final bilayers to minimize interference with bacterial components and binding of peptides in later experiments[284]. The extension of the PEG chain at this composition is approximately 5 nm.[134] Lipids were dissolved and mixed in chloroform. Chloroform was dried under high purity nitrogen gas and samples were subsequently placed in a vacuum desiccator overnight to drive off any remaining chloroform. Lipid films were rehydrated in PBS buffer to a final concentration of 2 mg/ml. Lipid solutions were extruded 15 times through a polycarbonate filter (Whatman Nucleopore) with 50 nm pore size and sonicated 20 min before use.

4.3 RESULTS AND DISCUSSION

4.3.1 Formation of OM-SB from OMVs

To induce OMVs to fuse to a glass surface, we modified a procedure reported previously by our group for the formation of proteinaceous bilayers from mammalian cell blebs[219,249]. This involved first adsorbing OMVs onto the glass followed by addition of PEG (polyethylene glycol)-liposomes to the system to catalyze OMV rupture. PEG-liposomes used here are composed of pure DOPC phospholipids mixed with a small fraction of PEGylated PE lipids containing PEG chains attached on their headgroups. There are several reasons for using PEG-

attached liposomes. First, PEG cushion underneath the membrane can increase the limited aqueous space between the substrate and the lipid bilayer. The expansion of the water gap in between the bilayer and the support has been suggested to protect transmembrane proteins from denaturing during contact with the substrate and further preserves their functionality,[130] which promotes the potential use of OM-SBs for bacterial OM protein studies. Second, PEG is a hydrophilic polymer and thus closely mimics the hydrophilic structures of carbohydrates attached on lipid headgroups in the OM, such as sugar moieties linked to lipid A molecules.

To visualize the formation of OM-SB, we used fluorescence microscopy. OMVs were first labeled with R18, a lipophilic dye that intercalates into membranes. OMV solution was diluted to desired concentration in PBS. 50-100 μL labeled OMVs were incubated on a glass slide in a PDMS well for 15-20 minutes. OMVs adsorbed to the glass support observable as punctuate bright spots in the top image of Figure 4.1a. Following adsorption, excess OMVs in the bulk solution were removed by rinsing the well with PBS buffer. OMVs adsorbed on the surface did not fuse and rupture into supported bilayers on their own. The immobility of lipids confirmed that bilayers were not formed at this stage (further confirmed by FRAP and QCM-D, discussed later).

To induce the OMVs to rupture, 50 -100 μL of PEG-liposomes were added to the PDMS well. The rapid formation of SLBs from PEG-liposomes in between the adsorbed OMVs catalyzed OMV rupture, most likely due to high edge energies of the SLB patches colliding with the adsorbed OMVs. The image series in Figure 4.1a shows that the bright punctuate spots originally confined to the adsorbed OMVs had spread throughout the surface uniformly at this stage. Diffusion of R18 originating from the membranes of OMVs into the newly formed PEG-SLBs confirmed the rupture of OMVs.

4.4.2 Acoustic property changes during planar bilayer formation

Quartz crystal microbalance with dissipation (QCM-D) is a technique that measures adsorbed mass to surfaces by tracking the change in resonance frequencies of the surface that is oscillated via piezoelectric excitation. Additionally, the dissipation feature measures the ability of the adsorbed material to dissipate acoustic energy, which can then be correlated to film stiffness. Figure 4.1b shows typical QCM-D frequency and dissipation responses and the corresponding mass curve of the OM-SBs formation process. First, OMV solution was sent to the chamber where OMVs gradually adsorbed on the QCM sensor, as indicated by the reduction in frequency and increase in dissipation. The amount of OMVs adsorbed depends on the length of time the solution is exposed to the sensor surface and the concentration of OMVs in the solution. A more detailed discussion of OMVs adsorption kinetics is provided in supplemental information. After the desired amount of adsorbed OMVs was achieved, PBS buffer was pumped in the chamber to rinse out unattached OMVs from the chamber. Buffer was then replaced by PEG-liposomes solution to induce OMV rupture. The frequency and dissipation changes that occur following the liposome solution support that OMVs ruptured upon the addition of PEG-liposomes, as observed previously monitoring R18 spread. After the frequency and dissipation shifts reached plateaus, PBS buffer rinsed out excess PEG- liposomes. Note that the final frequency was higher and dissipation was lower than the values before the addition of PEG-liposomes, indicating that not only PEG-liposomes form SLBs, but OMVs also rupture in the process.

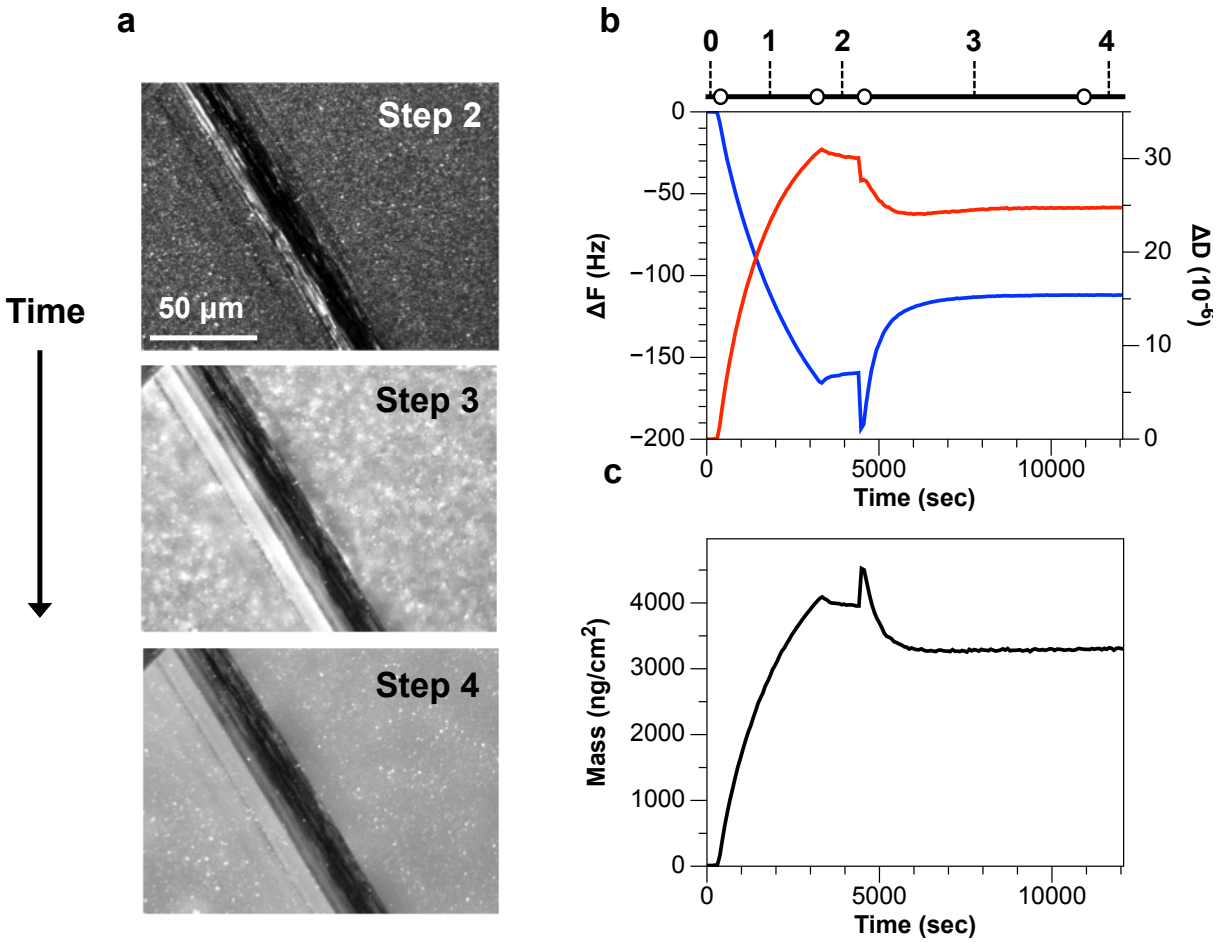

Figure 4.1. **(a)** The microscopy images showing the formation process of OM-SBs. OMVs were labeled with lipophilic fluorophore, R18, and PEG-liposomes were devoid of fluorescence. The dark lines in the images are scratches intentionally made to find the focal plane of bilayer. Intact OMVs labeled with R18 first adsorbed on the glass substrate, corresponding to step 2 in Fig. 1b. After the addition of PEG-liposomes, OMVs were induced to rupture (step 3), which resulted in the diffusion of R18 fluorophores from OMVs to newly formed bilayers (Fig. 1b, step 3). The uniform distribution of the fluorescence indicated the contiguous nature of the OM-SB as well as the mobility of the R18 within it (step 4). The images were all taken under 40x magnification. **(b)** Typical QCM-D curves showing the formation process of OM-SB. After initial PBS buffer baselines were achieved (0), OMVs were flowed into the chamber and adsorbed on the sensor (1). This step was followed by a PBS buffer rinse to remove excess OMVs not absorbed to the surface (2). PEG-liposomes were then sent into the system (3), which formed SLB patches and induced adsorbed OMV rupture. A final buffer rinse was made to remove any excess amount of vesicles from the system (4). **(c)** Frequency and dissipation signals were converted to adhered mass values, as shown in the lower plot. Changes in the mass on the surface along the formation process were determined using the one-layer Voigt-Voinova model (Appendix B).

4.3.3 Diffusivity and mobility of OM-SBs.

To further assess the mobility of OM-SBs, fluorescence recovery after photobleaching (FRAP) was used to measure two-dimensional diffusivity of the supported bilayers. Sample preparation and data analysis were performed as described in the *Appendix A*. Three types of

samples were prepared: adsorbed OMVs (before rupture), formed OM-SB, and DOPC with 0.5% PEG(5K)-PE SLBs (PEG-SLB). All of the samples were labeled with R18 for performing FRAP experiments.

As shown in Figure 4.2 (a), Sample A contained only intact OMVs and the photobleached spot did not recover at all after five minutes. The result was expected since fluorophores are not diffusive across adsorbed, unruptured OMVs. Sample B and Sample C were OM-SB and PEG-SLB, respectively. The diffusivities of sample B and C were around 0.4 $\mu m^2/s$ and 0.5 $\mu m^2/s$ respectively. The mobile fractions were both near one, suggesting that lipid mixing between the

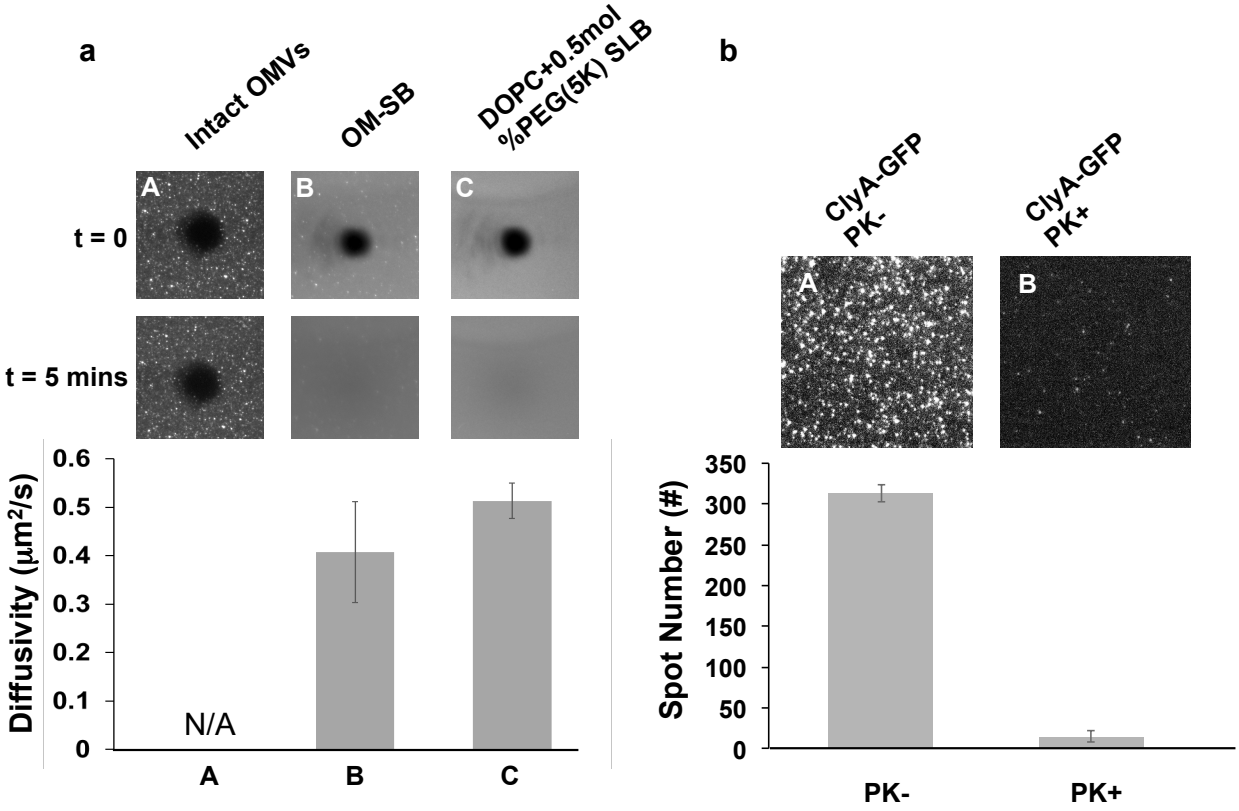

PEG-SLB and OM-SB was complete.

Figure 4.2. (a) Microscopic images of fluorescence recovery after photobleaching. (A): Intact OMVs labeled with R18. (B): OM-SBs labeled with R18. (C): DOPC with 0.5 mol% PEG(5K)-PE SLBs labeled with R18. The bar graph summarizes the diffusivities of these three types of supported bilayers. Note that due to the immobility of Sample A, no diffusivity could be determined. (b) Microscopic images of OM-SB expressing ClyA-GFP before (A) and after (B) Proteinase K treatment. The intensity of the punctate spots was abolished dramatically after the addition of proteinase K, which indicates that the majority of ClyA-GFP face up toward the bulk solution and that the orientation of the SB is the same as the OMV and bacterial cell. The bar graph below summarizes the densities of bright spots in the images. Multiple runs (n>3) were performed to obtain bilayer diffusivities and particle numbers.

4.3.4 Orientation of OM-SBs

One of the motivations for developing an OM-SB is to use the resulting bilayers as mimics for the bacterial OM. Thus, it was imperative to determine the orientation of the resulting bilayer after rupture. This characterization is easily carried out using a green fluorescent protein (GFP)-based fusion protein expressed in the OMVs. Previously, we demonstrated that OMVs can be engineered to display recombinant proteins on their exterior by leveraging the vesicle-associated hemolysin ClyA as a carrier molecule[285]. Specifically, a genetic fusion between ClyA and GFP (ClyA-GFP) was expressed in hypervesiculating in *E. coli* cells and observed to localize in OMVs with GFP facing the external solution[279].

To determine whether ClyA-GFP in OMVs became incorporated in OM-SB and oriented with extracellular side facing toward the bulk, proteinase K (PK) susceptibility experiments were performed on OM-SB derived from ClyA-GFP-containing OMVs in the following way. Upon exposure to PK, if the GFP proteins were oriented toward the bulk, they would be digested by PK and the fluorescence signal would be abolished. Otherwise the GFP would be protected beneath the lipid bilayer and resistant to PK treatment[285]. **Figure 4.2(b)** is the fluorescence microscopy of OM-SB derived from OMVs containing ClyA-GFP under 40x magnification, where the bright spots are the fluorescence signals from GFP. These images were analyzed using MATLAB (Mathworks) and ImageJ (NIH) for particle number counting. A home-based program was used to determine particle locations and numbers based on pixel clusters that meet an

intensity cutoff[36]. We used a fixed particle size in the model, so any larger fluorescent spot, i.e. vesicle aggregation or clusters, will be counted as multiple particles depending on the surface area.

Before incubation PK with the OM-SB sample, there were 313 ± 10 particles in a 1,600 μm^2 bilayer area (area shown in Figure 4.2(b)). After the treatment of PK, the majority of the signals are eliminated, and the number of the punctate spots dropped to 15 ± 7 particles. The result suggests that greater than 95% of the GFP were oriented facing the bulk phase and proteolytically digested by PK in the solution. This protein orientation reflects that in the intact bacterial OM, as well as the orientation in the bacterial membrane itself. Note that the OM-SB in this experiment was created from pure DOPC liposomes without any PEG. The replacement was made as a precaution to remove the possibility that outward-facing PEG molecules adjacent to the bilayer might hamper PK ability to interact with the transmembrane proteins[140] and bias the results.

4.3.5 Kinetic analysis of adsorbed OMVs to OM-SB transition

With the ability to control the amount of OMVs adsorbed on the surface, we investigated the relationship between the adsorbed amount of OMVs and the quality of the resultant OM-SB; that is, the variation in the % of OMVs that rupture overall. A higher OMV rupture percentage indicates that fewer OMVs remain intact, which then results in higher OM-SB quality (fewer defects), and vice versa. To assess OM-SB quality, we first developed a method to estimate the surface coverage of adsorbed OMVs, the theoretical mass of supported bilayers from 100% OMVs, and the theoretical mass of OM-SBs. We then applied these analyses to calculate the OMV rupture percentage and assess the role of surface coverage on OM-SB quality.

Estimation of the surface coverage of OMVs adsorbed on the sensor. To estimate the coverage of OMVs on the sensor, we formed a saturated monolayer of adsorbed, intact OMVs on the surface. The QCM-D curves in Figure B2 *(Appendix B)* show the mass at saturation of adsorbed OMVs (M_{satd}) is approximately 12000 ng/cm^2, which represents the maximum mass (jamming mass) for random sequential adsorption of OMVs on the surface. A detailed discussion of OMV adsorption kinetics is presented in the *Appendix B*. Thus, the surface coverage of unruptured OMVs (θ) can be estimated as a function of mass of adsorbed OMVs (M_{Ad}), saturation mass of adsorbed OMVs (M_{satd}) and the jamming limit of spheres on a 2D plane (~54%)[286]:

$$\theta = \frac{Mass\ of\ adsorbed\ OMVs\ (\frac{\mathrm{ng}}{\mathrm{cm}^2})}{\frac{Saturation\ mass\ of\ adsorbed\ OMVs\ (\frac{\mathrm{ng}}{\mathrm{cm}^2})}{0.54}} = \frac{0.54 \times M_{Ad}}{M_{satd}} \qquad (4.1)$$

Note that the expression shown in eq. (4.1) is only valid under the assumption that the acoustic mass from QCM-D (M_{Ad}, M_{layer}) is proportional to the biomolecule mass, i.e. $M_{Ad} \propto$ Number of OMVs adsorbed. However, the amount of coupled water may change with number of OMVs adsorbed and hence the acoustic mass obtained from QCM-D may not truly reflect the amount of OMVs adsorbed on the surface. To correct the error caused by the assumption, we applied a theoretical model proposed by Bingen et al (2008)[287] along with a three-dimensional COMSOL Multiphysics model to quantify the variation of solvation at different OMV surface coverage The simulated results can then be implemented to correct the surface coverage calculated using eq. (4.1) (*Appendix B*). All the calculations below were performed based on the corrected OMV surface coverage.

Estimation of theoretical mass of supported bilayer made only from OMVs. In the next step, we estimate the theoretical mass of lipid bilayer composed of 100% of OMVs (OMV-SB). It is not feasible to experimentally measure the mass of a pure OMV-SB since OMVs do not readily self-

assemble into supported bilayers on their own. Assumptions can be made to estimate the mass of OMV-SB as follows. The acoustic mass of OMV-SB is composed of the lipid mass, the protein mass, and the mass of solvent coupled to them. Kaufmann et al[119] reported that the mass of 100 wt% POPC SLB was 464 ng/cm^2 and the mass of a SLB consisting of 90 wt% POPC and 10 wt% *E. coli* wild type LPS was 563 ng/cm^2. Since bacterial outer membranes contain approximately 1:1 of phospholipids to LPS (ratio by weight), we assumed the mass of lipids and their coupled solvent was approximately 960 ng/cm^2.

The other contribution in OMV-SB mass is from membrane proteins. OMVs contain approximately 9:1 of lipids and proteins by weight, based on the BCA essay and Bradford protein assay (data not shown). Therefore we assumed that the mass of membrane proteins and their coupled solvents is one tenth of the lipid mass, 96 ng/cm^2. Note that we may be slightly underestimating the mass of the solvent coupled with membrane proteins here since proteins may possess higher amount of solvent than lipids. We then combined both masses and the mass of OMV-SB, $M_{OMV\text{-}SB}$, was determined to be 1075 ng /cm^2.

Estimation of theoretical mass of OM-SBs. We then applied the analyses above to estimate the theoretical mass of OM-SB, $M_{OM\text{-}SB,T}$, representing the mass of a complete bilayer with all OMVs and PEG-liposomes ruptured. $M_{OM\text{-}SB,T}$ is composed of the mass of OMV-SB ($M_{OMV\text{-}SB}$) and PEG-SLB ($M_{PEG\text{-}SLB}$ = 722±5 ng/cm^2) as a function of OMV surface coverage (θ) and area correlation coefficient $\varkappa$:

$$M_{OM-SB,T} = M_{OMV-SB} \times \kappa\theta + M_{PEG-SLB} \times (1 - \kappa\theta) \qquad (4.2)$$

$$\kappa = \frac{Surface\ area\ of\ ruptured\ OMVs}{Projected\ area\ of\ unruptured\ OMVs} = \frac{4\pi r^2}{\pi r^2} = 4$$

The coefficient $\varkappa$ illustrates the surface area changes of OM material on the support due to bilayer expansion upon vesicle rupture.

Calculation of OMV rupture percentage. In the last step, we gathered all the information obtained above to calculate OMV rupture percentage. Ideally, if all adsorbed OMVs and PEG-liposomes ruptured, the experimental mass of OM-SB, $M_{OM\text{-}SB,EXP}$, should be identical to the theoretical mass, $M_{OM\text{-}SB,T}$. However, depending on the surface coverage of OMVs (θ), some amount of OMVs may not rupture, which then makes $M_{OM\text{-}SB,EXP}$ different from $M_{OM\text{-}SB,T}$.

To determine the role of surface coverage of OMVs (θ) in shifting the OMV rupture percentage, we first analyzed the composition of the experimental mass of the OM-SB, $M_{OM\text{-}SB,EXP}$ as follows:

$$M_{OM-SB,Exp} = (1-P)\times M_{Ad} + \kappa P\theta \times M_{OMV-SB} + M_{PEG-SLB}\times(1-(1-P)\theta - \kappa P\theta) \qquad (4.3)$$

$$When\ P\ \rightarrow 1, M_{OM-SB,Exp}\ \cong\ M_{OM-SB,T}$$

Where P is OMV rupture percentage. The first term is given by the mass of non-ruptured OMVs. The second term is the mass of bilayer from the ruptured OMVs, and the last term indicates the mass of bilayer from PEG liposomes. Since all the variables are known except the rupture percentage (P), we can calculate its value from equation (4.3).

Figure 4.3 (a) reports the results of OMV rupture percentage (P) along with the corresponding OMV surface coverage (θ), showing the trend of lower rupture percentage for higher surface coverage. The inverse relation between the rupture percentage and OMV coverage is as expected. Lower coverage indicates higher PEG-SLB, which then increases the possibility for adsorbed OMVs to rupture upon the contact with fluidic PEG-SLB. Moreover, it is less likely for PEGylated vesicles to get in and land on the spaces in between the intact OMVs at higher surface coverage. We concluded from the above analysis that fewer OMVs adsorbed on the surface would result in better OM-SB qualities, that is fewer defects, and thus there is always a trade-off between the amount of OMVs adsorbed to obtain decent OM-SB quality with

incorporating a significant amount of OMV-originated materials into it.

Based on the study of estimated OMV rupture percentage reported in Figure 4.3a, we have further calculated the corresponding amount of final OM component incorporated in OM-SB, as shown in Figure 4.3b. Our calculation suggests that at lower OMV surface coverage (<10%), the amount of OM material in OM-LB increases as more intact OMVs are introduced in the system. When OMV surface coverage exceeds ~ 10%, the amount of OM materials that can be incorporated in the platform roughly levels out to 22-25%. Although beyond the scope of this study, we believe it may be possible to increase the amount of OM materials incorporated in OM-SB using several physicochemical approaches. By optimizing temperature, pH (especially acidic condition)[288], liposome compositions and liposome sizes, we can potentially improve the quality of OM-LB with more OMV catalyzed to rupture and fuse.

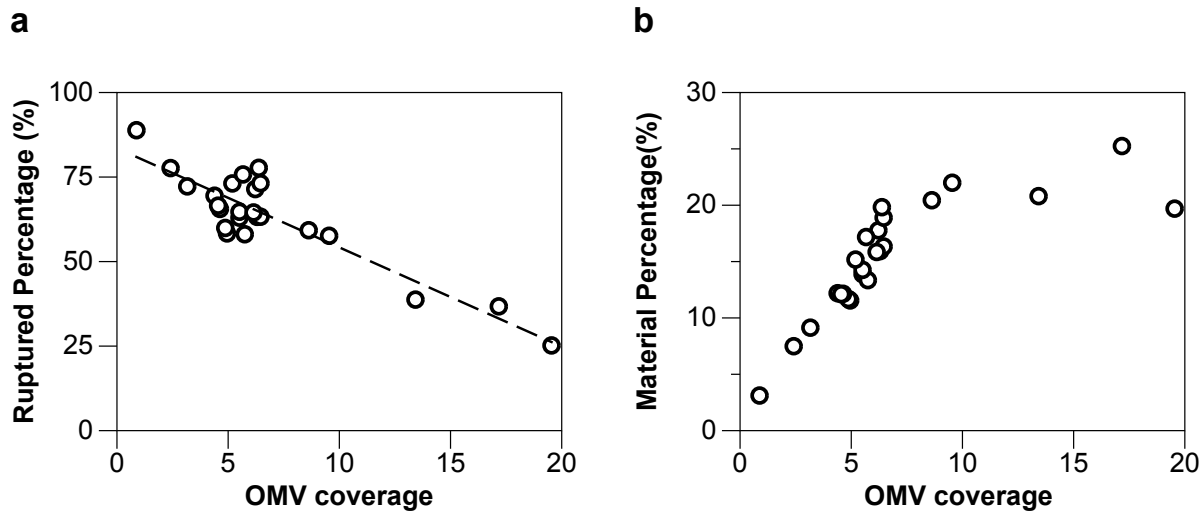

Figure 4.3 (a) The relationships of OMV surface coverage and the estimated OMV rupture percentage. The black dash line was a linear regression line with correlation factor, R^2, to be 0.82 . (b). The relationships of OMV surface coverage and the estimated OM material incorporated in OM-SB. Note that OMV coverage correlates to the footprint of intact OMV before rupturing. For instance, 9% OMV coverage with ~ 60% ruptured percentage corresponds to ~ 22% OM material in OM-SB.

Kinetics of OMV rupture catalyzed by the addition of PEG-liposomes. Following the analysis of bilayer properties, orientation, and quality, we further analyzed QCM-D curves to characterize

OM-SB formation kinetics. As shown in Figure 4.1c, the mass curve displays four stages: OMVs adsorption (1), PBS rinse (2), PEG liposomes incubation (3) and final buffer rinse (4). To study how OM-SB forms upon the addition of PEG liposomes, we focus on the third stage since it reveals detailed information about the planar bilayer formation process.

Upon the addition of PEG vesicles, the mass dramatically increased due to the adsorption of PEG vesicles on the surface in between OMVs. The critical coverage was soon reached and PEG vesicles began to rupture, as indicated by the decrease in mass. The decrease in mass was mainly due to the release of buffer from the internal lumens of both the PEG vesicles and OMVs. From a series of experiments, we observed that the trend of the decrease in mass is highly dependent on the OMV surface coverage(θ). When OMV surface coverage is low (Fig. 4A), the negative mass shift presents two-regime kinetics, where the mass first dramatically decreases and continues to drop at a slower rate until it reaches steady state. As OMV surface coverage increases (Fig. 4B) only one-regime kinetics is observed with the loss of the first rapid decrease in mass.

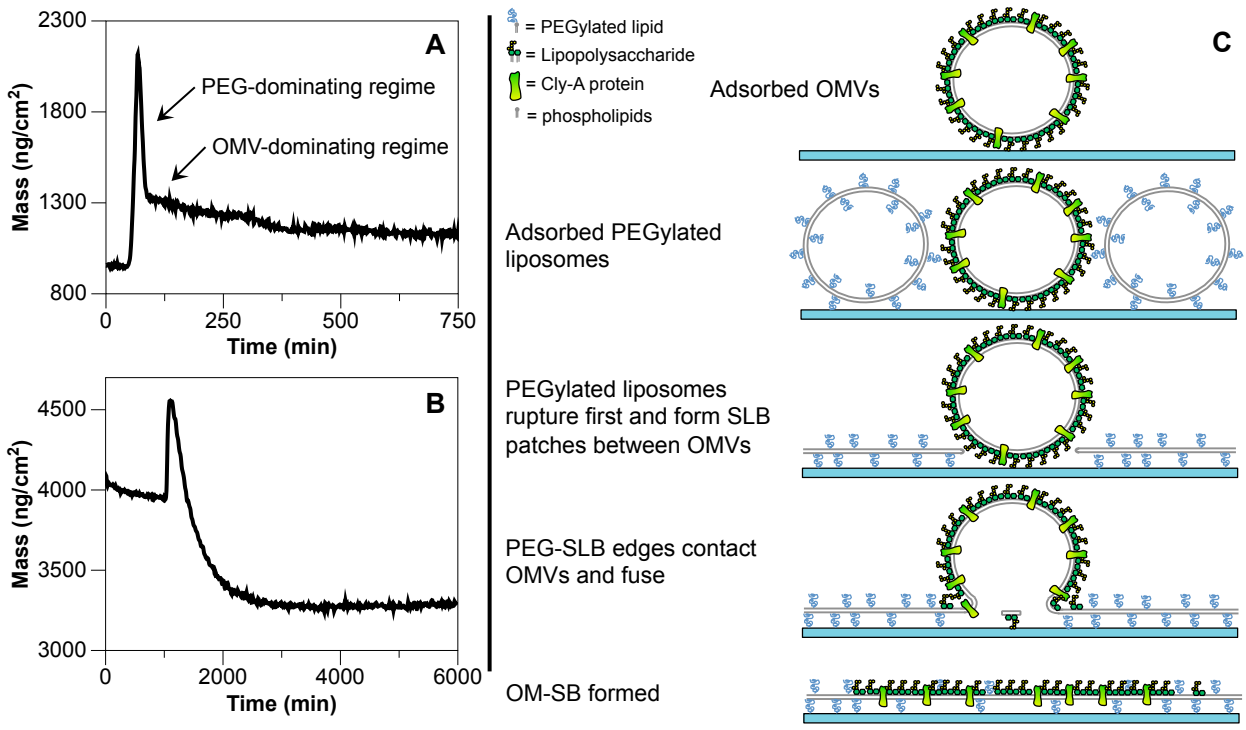

Figure 4.4 The mass curves of the formation process of OM-SBs with (A) lower OMV coverage (3.2%) and (B) higher OMV coverage (13.4%). (A) At lower OMV coverage, the rupturing process presents two-regime kinetics, the mass first dramatically decreases (PEG-dominating regime) and then transitions to a slower rate of decay (OMV-dominating regime). (B) At higher OMV coverage, only one-regime kinetic (OMV-dominating regime) is observed: the initial quick drop is no longer distinguishable. (C) A proposed scheme of OM-SB formation mechanism. OMVs first adsorbed on the substrate and remained in vesicle form. PEG-liposomes were then added to the system, which rapidly adhered to the surface and formed PEG-SLB in between OMVs. The newly formed PEG-SLB induces OMV rupturing and spread on the surface, which results in the formation of OM-SB. Note that the components of the OMV are not drawn to scale, but simplified to illustrate the mechanism of OM-SB formation.

One of the possible mechanisms to explain the observations is that the first regime, which is only present when OMV surface coverage is low, indicates that the dominating mechanism initially is the formation of bilayer from the PEG vesicles (PEG-dominating regime). The following slower negative mass shift suggests that the newly formed PEG bilayer then catalyzes OMVs to rupture, which is the rate-determining step in the second kinetic regime (OMV-dominating regime).

When working with low OMV surface coverage, there is a larger surface area for PEG vesicles to adsorb, rupture and form bilayer sheets, and this PEG bilayer formation process is

less likely to be affected by the adsorbed OMVs. Therefore, it is not surprising that the PEG bilayer formation phase is distinguished from the OMV rupture phase in the curve. As OMV surface coverage increases, the surface area for PEG liposomes to form bilayer is limited, which makes pure PEG bilayer formation no longer significant enough to be observed alone. The higher amount of adsorbed OMVs force the immediate interaction of the small PEG SLB patches with unruptured OMVs and catalyze them to rupture. Throughout the entire process there are no distinguishable kinetic phases, but a single convolution of both types together, resulting in a general slowdown of the overall kinetics due to the slower kinetics of OMV rupture. The proposed OM-SB formation scheme described above is summarized and illustrated in Figure 4.6c

Based on the proposed formation mechanism, we built a kinetic model to describe the OMV-dominating regime to understand how OMVs were catalyzed to rupture via their contact with the edge of PEG bilayer:

$$\text{OMV + PEG-SLB} \rightarrow \text{OM-SB+ Mass loss due to release of luminal solution} \qquad (4.4)$$

By hypothesizing equation (4.4) as a Poisson process, we fit the corresponding rate equation, a single exponential equation (4.5), to the normalized OMV-dominating regime, which represented the cumulative mass lost due to the release of encapsulated solution in OMVs:

Poisson Process

$$Probability\ of\ reaction = k \cdot \exp(-kt), k = rate\ constant$$

$$Cumulative\ Distribution\ Function = 1 - \exp(-kt) \qquad (4.5)$$

To define the location of the OMV-dominating regime, we followed the principles described next. We found qualitatively from a series of experiments that two-phases regimes occurred whenever surface coverage (θ) was lower than 10%, and we defined the OMV-dominating regime by finding location that gave the best least-squares fit of equation (4.5). For surface

coverage (θ) higher than 10%, the mass curve starting from the maximum value till the plateau was seen as the OMV-dominating regime.

Figure 4.5 shows the relation of the rate constant, *k,* and OMV surface coverage, θ. When θ < 17%, the values of *k* were around 2×10^{-3} to 4×10^{-3} (1/s), showing no strong dependence on the surface coverage. However, once OMV surface coverage increased above 17%, *k* dropped significantly. The decrease in *k* at high surface coverage conditions may originate from the dense packing of OMVs. As θ increases, it is highly probable that OMVs are close enough together to limit the likelihood of OMVs contacting the PEG bilayer that have already formed. When OMVs no longer have access to freely associate with PEG bilayers, OMV rupture rate slows down and the rate constant *k* drops.

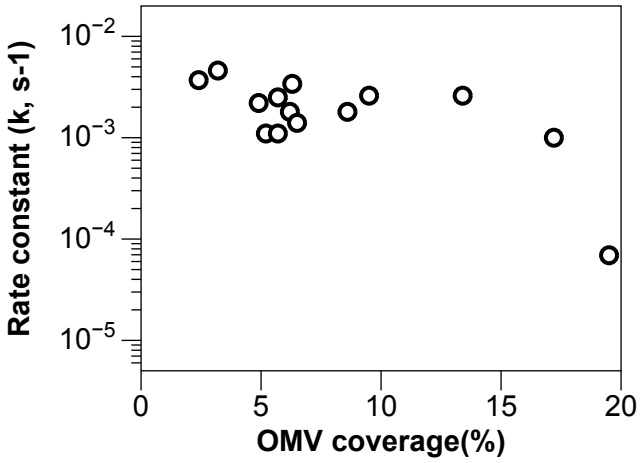

Figure 4.5 The rate constant k under different OMVs surface coverage.

4.3.6 Application of OM-SB: sensing anti-microbial peptide activity.

The most valuable characteristic of OM-SB system is its native-like bacterial OM bilayer environment in the geometry of a planar sheet that couples well to analytical tools. Thus, OM-SBs open up many possibilities for investigating bacterial OM biological functions, especially its

role in protecting gram-negative bacteria from its environment *i.e.*, antibacterial compounds. OM-SBs have great potential to test how bactericidal antibiotics disorganize/disrupt the highly ordered OM to kill gram-negative bacteria, which can be used as a basis for a new generation of antibiotic design.

In this study, we demonstrate how OM-SB is applied to probe the antimicrobial mechanism of polymyxin B (PMB), an amphipathic peptide composed of a cationic cyclic portion (a net charge of +5) and a hydrophobic fatty acyl tail. PMB is primarily used for treating gram-negative bacterial infection and endotoxin. The mechanism of action of PMB has been investigated since 1970s and because it has been studied extensively, PMB is a great candidate to test our OM-SB system against to ensure our system recapitulates known results and therefore is an effective, functional model of the OM surface. It is believed that PMB molecules specifically bind to lipid A molecules in a one to one ratio[289] and the binding is generally described as following a two-step mechanism. The polar portions of PMB first interact with the anionic lipid A head groups through electrostatic attractions, which allows the aggregation of PMB on OM surfaces. These electrostatic interactions further promote the insertion of PMB's fatty acyl chains due to their hydrophobic interaction with the lipid A tails.[290–293] The PMB-lipid A binding further alters membrane permeability by destabilizing the tight packing of adjacent lipid A fatty acyl chains to disrupt OM integrity.

To clearly elucidate the mechanism of PMB towards OMs, various techniques have been applied to determine the binding kinetics of PMB-lipid A complexes. For instance, Thomas et al[263,294,295] first reported the kinetics of each elementary step involved in the binding process using surface plasma resonance and stopped flow spectrofluorometry. However, to our knowledge, no kinetic evaluation of how the mechanical properties of the bacterial membrane change upon the

binding of PMB has been reported. In this work, by monitoring the interaction of PMB and OM-SB using QCM-D, we are able to extract additional information on how bound mass and viscoelastic properties of OM vary during the interaction with PMB.

QCM-D has been used extensively to study antimicrobial peptide interaction with model membranes due to unique insights it provides into structural/conformational information of membrane-peptide complexes[283,296,297]. However, these studies were performed on simple artificial bilayers composed of phospholipids like POPC/DOPC, or biomimetic bilayers mimicking bacterial inner membrane (IM). Due to the difficulty of LPS vesicles to fuse into a supported bilayer[119], to our knowledge, no QCM-D studies have been developed to study peptide-OM interaction. Since LPS is central to the mechanism of PMB action, investigating antimicrobial mechanism on OM-SB using QCM-D fills this gap in the literature.

To explore the interaction between PMB and OM-SB in a quantitative way, we fit the QCM-D responses using a two-layer Voinova viscoelastic model[282]. Most of the peptide-QCM studies use the Sauerbrey relation to directly correlate the frequency shifts to mass changes. However, as previously stated, OM-SB is a highly viscoelastic film ($\Delta D \gg 10^{-6}$) so that a viscoelastic model must be applied for an accurate estimation of mass and viscoelastic properties of the system. The one-layer model relies on the assumption that the entire system is a homogeneous viscoelastic film attached to the surface, so the fitted results of film mass, viscosity, and shear modulus represent a general picture of the mechanical properties of the whole layer. However, OM-SB is a heterogeneous film and we want to examine the detailed structural events occurring at different locations in the membrane. That is, for PMB binding/insertion kinetics, a two-layer model must be applied to distinguish mechanical property changes of the top layer (membrane surface at the interface with the bulk) from the bottom layer (the rest of the membrane). A

detailed simulation scheme has been described in the *Methods* section.

Before investigating PMB activities, first we must define the location of the interface in between the layers. By fitting the frequencies and dissipations of all overtones at initial time point to the model, we extract the information of thickness, viscosity, and shear modulus of both films. The simulated thicknesses of the top layer and the bottom layer are 3.6 ± 0.41 nm and 11.7 ± 3.40 nm, respectively. The model also yields a viscosity of 1.12 ± 0.17 cp and a shear modulus of $(4.3 \pm 1.4) \times 10^5$ Pa for the top layer, and a viscosity of 1.34 ± 0.14 cp and a shear modulus of $(4.6 \pm 0.4) \times 10^4$ Pa for the bottom layer.

Based on the simulated results obtained from the two-layer model, the top layer extends from the headgroup of the upper leaflet to the PEG chain, and the rest of OM-SB then belongs to the bottom layer (as shown in Figure 4.6a). Note that the PEG globular diameter is about 5 nm at this PEG density and the typical thickness of a lipid only bilayer is on order of 4 nm, so the model predictions fall within a reasonable range. The estimated thicknesses of both films also correspond well with the viscoelastic information obtained from the model. The viscoelastic ratio, $\tan(\delta)$, of the top layer is about ten times smaller than the bottom layer, indicating the top film is particularly stiff compared to the rest of the system. The stiffness of the top portion is probably a result of dense packing of LPS molecules due to lateral interactions of sugar units and headgroups. This integrity further imposes steric constraints to the PEGlyated lipids and restricts the motion of the PEG chain above the bilayer as well. The rigidity of the LPS layer above the bilayer mechanically distinguishes the top glycosylated layer from the rest of the membrane bilayer.

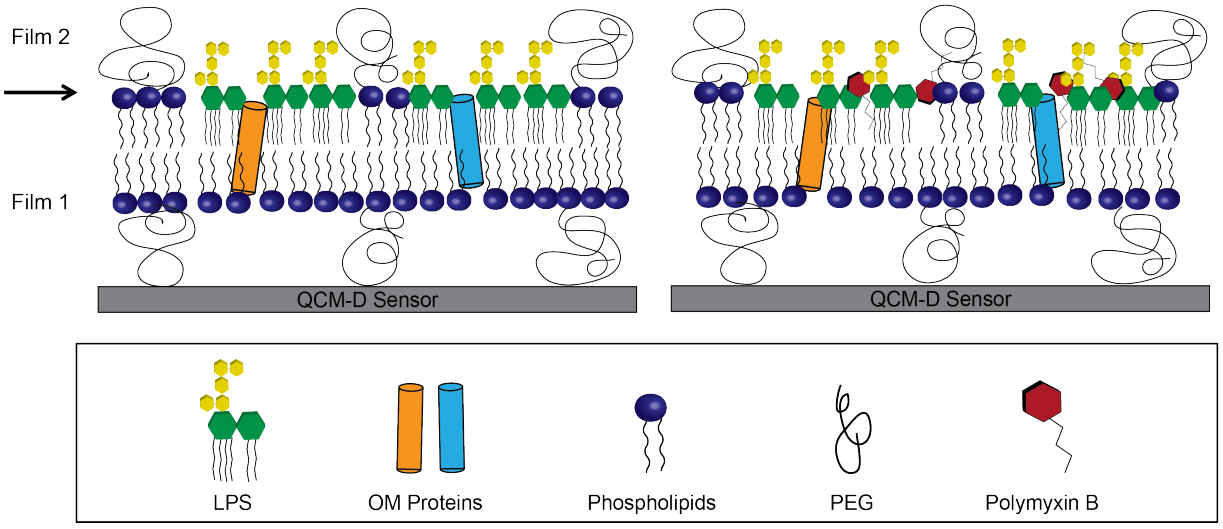

Figure 4.6 The illustration of (a) OM-SB and (b) the complex of OM-SB-PMB. Based on the simulated result of two-layer Voigt-based model, a guideline (dot line) was drawn to indicate the interface of film 1 and film 2. OM-SB contains both native OM lipids and a variety of OM proteins.

An overall QCM-D response of OM-SB formation along with PMB addition is presented in Figure B5. The qualitative shifts of frequency and dissipation upon the addition of PMB solution are magnified in Figure 4.7a, and 4.7b. To rule out the possibility that non-specific artifacts (PMB to PEG-SLB) are present, negative control experiments were performed to confirm that no signal was detected with the addition of PMB to simple PEG-SLB (*Appendix B*). We noticed that the frequency and dissipation kinetics are highly overtone-dependent. The lower-order overtones show decrease in frequency signals while the higher-order overtones exhibit a slight increase. The dissipation shifts grow for all overtones, and the increasing amount is in a descending order from low to high overtones. To further understand the physical meaning behind these responses, we fitted the frequency and dissipation data to the two-layer Voinova model and extracted the information of how viscosity, shear modulus, and thickness of both layers evolve along with the addition of PMB (Fig. 7, c-h). These simulation results not only reveal important clues on the antimicrobial mechanism of PMB, but also provide a qualitative view of how PMB alters the

OM-SB structure and mechanical properties.

First we pay our attention to the quick increase in thicknesses of both layers upon the addition of PMB. The increased thicknesses of both layers are probably a result of PMB-LPS complexes. Upon the introduction of PMB into the system, PMB molecules quickly bind to LPS (lipid A) and further penetrate into the bilayer with the hydrophobic tails inserted into LPS acyl chains. Since PMB-LPS complexes span across the layer-layer interface, the effective thicknesses grow for both the top and bottom films. The fitted changes of viscosity and shear modulus in both layers also support the proposed mechanism.

The aggregation of PMB on the bilayer surface and the tightly bound of PMB-LPS impose steric constrain to the top layer, resulting in the increase of shear modulus and viscosity of the top layer. Conversely, the shear modulus and viscosity of the bottom layer both dropped along with the OM-SB-PMB interaction. The insertion of PMB molecules disrupts the integrity of the bilayer and transforms the membrane to be more permeable to the bulk fluid. As a consequence, more solvent molecules are entrapped within the membrane, which lowers the shear modulus and viscosity of the bottom layer.

The above antimicrobial mechanism study successfully demonstrates that OM-SBs are a useful model that closely mimics OMs of bacteria, and it can be utilized as an *in vitro* platform to capture antibiotic mechanism of PMB. With the appropriate analysis, we are able to monitor how bilayer mechanical properties (thickness and viscoelasticity) evolve dynamically at different locations within the membrane. This detailed mechanistic information can be applied to propose antimicrobial mechanism of PMB, which turns out to correspond well with the existing studies (binding and insertion) in the literature for this compound. In addition, this platform serves as a unique tool to quantitatively report the mechanical property changes of the membrane

itself induced by antimicrobial activity, which is not available by using other techniques.

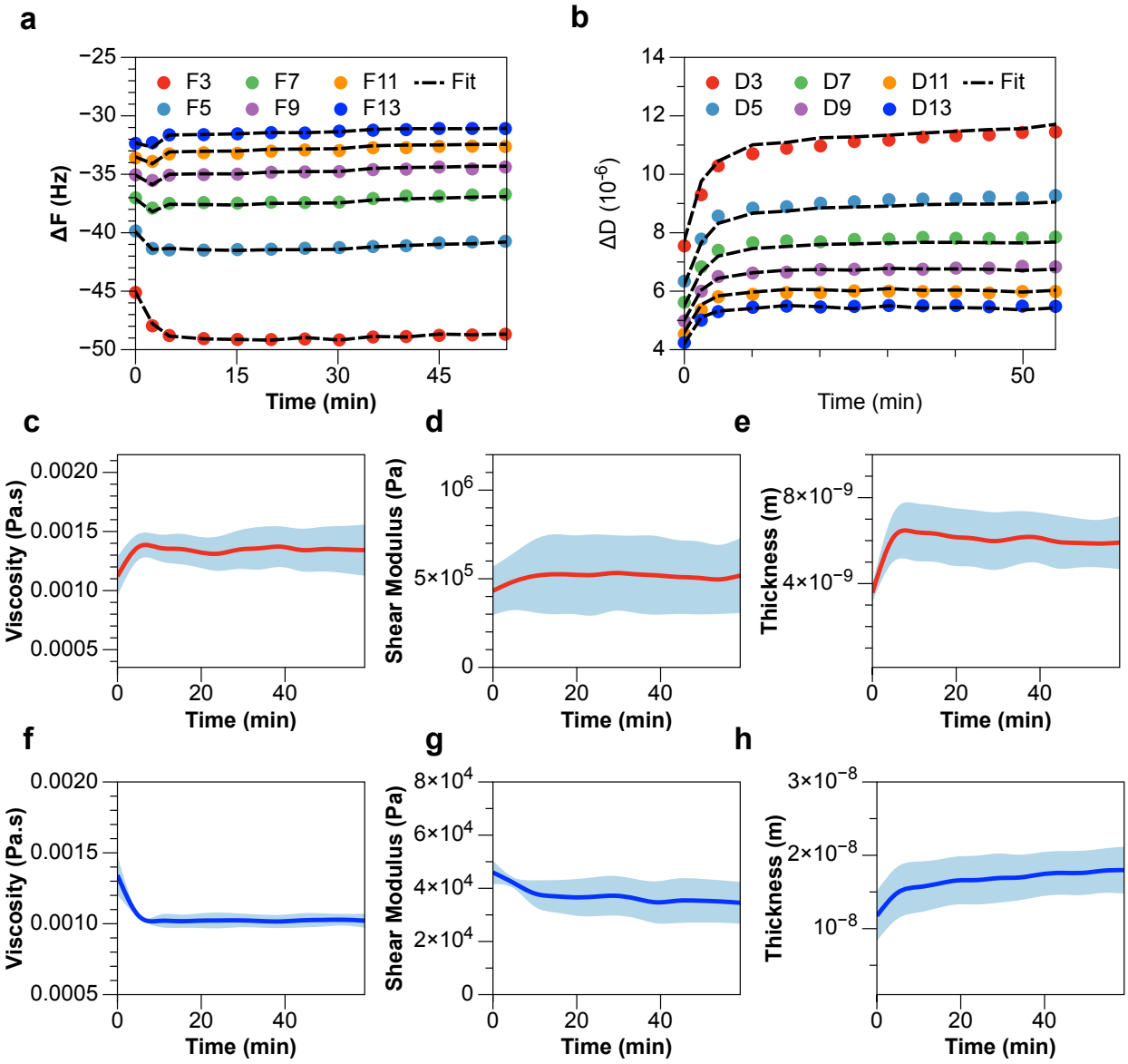

Figure 4.7 The experimental (a) frequency and (b) dissipation kinetics and the simulated results (black dot line) derived from two-layer Voinova model. As PMB introduced it to the system, the viscosity (c) and shear modulus (d) of the top layer (film 2, red) increase as PMB molecules bind with LPS and aggregate on the surface, and thus the mass of top layer (thickness (e)) also increases. Upon the binding with LPS, PMB molecules further penetrate into the bilayer and disrupt it integrity, which then result in the decrease of bottom layer's (film 1, blue) viscosity (f) and shear modulus (g). The mass of the bottom layer (h) increases due to PMB binding and insertion. The simulation results were carried out using three individual experiments and the standard deviations are shown as the blue regions.

4.4 CONCLUSION

In this work, we developed an in vitro supported bilayer platform (OM-SB) directly from outer membrane vesicles (OMVs) of *E. coli* that closely mimics the outer membrane of these gram-negative microbes, including their native lipid and protein content, and preservation of the asymmetry of the membrane. Our approach, in contrast to reconstitution methods, overcomes the difficulty of incorporating OM lipids and proteins into a planar geometry while preserving native orientation and structure of membrane molecules.

The advantage of the planar OM-SB is its capability of being investigated by surface sensitive techniques. In this study, we combined both fluorescence microscopy and QCM-D to quantitatively characterize the OM-SB compositions and formation kinetics. We then demonstrated that the OM-SB is capable of recapitulating the mechanism of antibacterial agents using a well-study antimicrobial peptide, Polymyxin B, for an illustration. By elucidating the frequency and dissipation shifts measured using QCM-D with two-layer mechanical models, we provide new information as well about the changes in bacterial membrane mechanical properties during antibacterial action. We conclude that PMB binds to and aggregates on the OM-SB surface and destabilizes membrane integrity by further insertion throughout the bilayer. Extending similar studies to other antibiotic compounds using the OM-SB and surface analysis techniques like QCM-D, we believe this platform can offer many insights into understanding antibiotic kinetics for future drug design and screening host-pathogen interactions to facilitate bacterial vaccination development.

4.5 ACKNOWLEDGEMENTS

This chapter has been accepted for publication in Scientific Reports as “A Molecularly Complete

Planar Bacterial Outer Membrane Platform". Chih-Yun Hsia was the first author and co-authors include Linxiao Chen, Rohit Singh, Matthew DeLisa and Susan Daniel. C.Y.H. and S.D. conceived and designed the study. C.Y.H. performed experiments and carried out data analysis, modeling, and interpretation of results. L.C. generated the OMVs, characterized them, and assisted with data interpretation. M.P.D. assisted with interpretation of results. All authors wrote and edited the manuscript, and approved the final versionWe thank Roland Lloubes for strain JC8031. This material is based upon work supported in part by NIH Grant EB005669-01 (to M.P.D.), NSF Grants CBET 1159581 and CBET 1264701 (both to M.P.D.), NSF Grant CBET-1149452 (to S.D.), and an NSF GK-12 "Grass Roots" Fellowship (to L.C.).

CHAPTER 5

OUTLOOK

Several *in vitro* methods that advance the characterization of lipid-protein interaction are presented and discussed in this thesis. Model membranes, supported lipid bilayers especially, provide simple solutions to the complexity of cell-based systems. This work has centered on the idea of expanding the current simple SLB systems with increased complexity and biological relevance. The ultimate goal of this research is to use such a system to offer new insight into the interaction of a broad range of membrane proteins with their lipid environment. This emerging technique possesses significant advantages over traditional tools because it preserves the key biologically relevant components in a simplified model while circumventing several drawbacks associated with the current methods.

One of the significant features of the SLBs model developed in this work is its capacity to capture the heterogeneity of a native cell membrane. With the ability to control the spatial location and lipid compositions of the supported bilayers, we patterned two-phase coexistent SLBs inside a microfluidic and introduced the target membrane species within it. The device was used to quantify the partitioning of targeted biomolecules based on their chemical affinity for the particular lipid domain. We have demonstrated that this device is capable of providing insight into how structural factors, membrane compositions, and environmental factors influence partitioning. The platform can also be applied to serve as a two-phase lipid bilayer extraction channel to separate or enrich the membrane species within heterogeneous SLBs. A drag force due to the hydrodynamic bulk flow of the buffer solution was applied to move the SLBs, and the moving SLBs convect the species along the microchannel, while those species also gradually diffuse and partition into the lipid phases they have the most affinity for.

Another important advancement outlined in this thesis is the development of membrane protein delivery into the lipid bilayers. The traditional methods of delivering proteins into SLBs are often associated with low yield protein purification and difficult reconstitution processes. Also, these methods are often detergent mediated; thus they require careful optimization of conditions for the protein of interest and may cause changes to the protein conformation. In light of these challenges, we have developed a simple and universal technique to incorporate a board range of membrane proteins into SLB models: delivery of membrane proteins via cell derived bleb fusion. Adsorbed blebs rupture, forming a bilayer, when additional fusogenic lipid vesicles are added. This platform has enabled us to study viral fusion, which requires membrane protein receptors in a mobile lipid bilayer. To use this system to study lipid–protein interactions, we require 1) mobile membrane proteins that do not interact with the support and 2) correct protein orientation such that the extracellular portions of membrane proteins are exposed towards the bulk. By incubating blebs with PEGylated liposomes, a cushioned bleb bilayer can be generated and this approach results in more membrane protein mobility. We have also conducted a thorough characterization to define the orientation of proteins in SLBs using enzyme assays where we confirmed that bleb fusion is following a parachute mechanism and protein orientation is preserved.

Besides simply introducing targeted membrane proteins in SLBs, this methodology also provides the benefit of building a molecularly complete platform to closely mimic a specific type of cell environment. In Chapter 4, we developed a SLB platform directly from outer membrane vesicles (OMVs) of *E. coli*, and this OM-like supported bilayer (OM-SB) exhibits the physiochemical characteristics of the bacterial outer membrane from which the OMVs are derived. This approach overcomes the difficulty of incorporating OM lipids and proteins into

SLBs, which often requires laborious purification and reconstitution steps. Also, these native OM materials are in their native conformations and orientation, so the asymmetry of the OM membrane is preserved. These features allow for the interrogation of cellular membrane components using surface sensitive techniques that are otherwise impossible to apply to live cells. We have demonstrated the utility of the OM-SB platform by quantitatively measuring antibiotic interactions between OM-SBs and an antimicrobial peptide using QCM-D and fluorescence microscopy. This proof-of-concept work suggests that we can apply our biomimetic OM-SB system to the study of cell surface interactions via surface analysis techniques to characterize cellular surface properties, investigate antibiotic kinetics, guide drug discovery and investigate host-pathogen interactions.

Future work on this project could involve combining the platform along with other techniques to open the platform to have a broader impact on assessing various biological processes. Currently, we have ongoing collaboration with the Owens Groups in Ecole Nationale Supérieure des Mines, CMP-EMSE. We are interested in combining the proteinaceous SLB platform with organic electrochemical transistors (OECT) to investigate activities of ion channel embedding in proteinaceous supported bilayer. Organic electrochemical transistors (OECTs) are organic electronic devices that have been extensively developed as biosensors to study biological events due to their tunable and flexible properties[298]. OECT can effectively record and amplify changes in ion flux through the biomaterials of interest to unravel the fundamental bioelectrical mechanism. We aim to develop novel biosensors by coupling proteinaceous supported bilayers with OECTs to monitor electrical readout of targeted ion channels in real time.

The challenge of developing such a system lies in assembling a proteinaceous supported bilayer on a conducting polymer film, which is the active material in OECTs. The polymer film

in this case is poly(3,4-ethylenedioxythiophene) doped with poly(styrenesulfonate) (PEDOT:PSS). A supported bilayer is easily formed on smooth and hydrophilic substrates like glass or mica. However, forming a bilayer on a rougher and less hydrophilic polymeric film is challenging and requires optimization and characterization. To overcome this difficulty, we need to engineer the compatibility of the bilayer to the polymer film. The transformation of liposomes self-assembling to a supported bilayer is mainly governed by van der Waals and electrostatic interactions in between liposomes and the support. The lack of these attractive forces will result in the failure of bilayer formation. Two strategies will be applied to enhance the attraction of liposomes and the polymer surface. First, we will focus on the optimizing the polymer surface through both chemical modification and physical preparation so that its structure and surface properties are best suited for vesicle fusion to occur. Second, we will alter liposomes composition to enhance the interactions between the polymer and lipids. For example, we can incorporate positive lipids to increase the electrostatic forces with the negatively charged PEDOT:PSS surface. Other possibilities are to enhance interactions with chemical modifications that bridge the polymer surface and lipids through engineered binding interactions and reactive groups.

Along with the direction to apply the technique to characterize various aspects of membrane proteins, we are also working on improvement of the current platform to broaden up its accessibility. One of the obvious aspects is to optimize the formation process of proteinaceous SLBs to induce more cell blebs/OMVs to undergo vesicle fusion. With the current technique, the amount of cell vesicles that can be incorporated in is limited. In chapter 4 we have found that the relation of the vesicle surface coverage and vesicle rupture percentage inversely proportional. That say, it is not plausible to introduce targeted membrane proteins in abundance using the

developed procedure and an optimization must be performed to remove the limitation.

This limitation may pose restrictions to the potential applications of the technology. For instance, one application we have started to pursue is looking into the interactions of targeted membrane proteins with local lipid domains. We proposed to combine the developed techniques discussed in Chapter 2 and Chapter 3 to create a two-phase coexistent proteinaceous SLBs in a microfluidic device. We plan to first pattern lipid raft on one side of the channel and form fluidic supported lipid bilayers containing target membrane proteins adjacent to lipid raft. Such a device can be applied to 1) identify the partitioning of membrane proteins to understand how they are sorted/organized with lipid raft, and also 2) probe protein activity levels as a function of bilayer compositions to unravel the impact of lipid-protein interaction to biological processes. However, we found that single particle imaging in a two-phase SLB system is much more challenging than expected. In preliminary work, we have noted that the amount of membrane proteins is low, which prevents high-quality protein imaging. This is probably because the population of membrane proteins originating from the fluidic SLBs is diluted as proteins partition into lipid raft. A signal drop is also observed, which may be attributed to photobleaching as protein partitioning takes up to a few hours to reach stable state. To remove this limitation, current procedure will have to be modified to improve membrane vesicle rupture upon the addition of liposomes to introduce more membrane materials in the SLB platform. This modification can be addressed through several aspects such as: liposomes composition optimization, buffer salt concentration, incubation temperature or cushion strategy.

While membrane proteins have long been the focus of studies aimed at understanding biological function in the cell, lipids are only starting to become appreciated for their role in regulating membrane protein functions. Therefore, few platforms and approaches have been

developed to directly assess lipid-protein interactions and determine their regulatory roles in cellular activities. So far, most of the work has been performed either in complex *in vivo* environments that prevent identification of individual cellular activities, or simplified artificial membrane platforms that lack biological relevance. The techniques described in this thesis have removed the complexity of real cells while preserving the heterogeneous nature of membrane environment and native membrane proteins' structures /functions. The platform bridges the two distinct methodologies in the current field and serves as a novel membrane model that expands the characterization of lipid-protein interactions.

Appendix A

1. Fluorescence Microscopy

Unless noted otherwise, images shown in this dissertation were obtained using an inverted Zeiss Axiovert Observer.Z1 fluorescence microscope equipped with α Plan-Apochromat objectives, a Hamamatsu EM-CCD camera (ImageEM, model C9100-13, Bridgewater, NJ), and X-Cite® 120 microscope light source (Lumen Dynamics Group Inc., Canada). Different filter cubes were used to collect the fluorescence: ET GFP filter cube (49002, c106273, Chromatech Inc.) was used to collect the fluorescence emitted from GFP and BODIPY fluorophores; ET MCH/TR filter cube (49008, c106274, Chromatech Inc.) was used to collect the fluorescence emitted from octadecyl rhodamine (R18) and Alexa 594 fluorophores.

2. Preparation of Lipid Vesicles for Formation of Supported Lipid Bilayers

Lipids were dissolved and mixed in chloroform and methanol at the desired compositions. The solution was dried under high purity nitrogen gas to remove the solvent. The dried samples were subsequently placed in a vacuum desiccator overnight to drive off any remaining chloroform. Lipid films were then rehydrated in PBS buffer (5 mM phosphate buffered saline with 150 mM NaCl at a pH of 7.4) to a final concentration of 2 mg/ml. Lipid solutions were extruded 15 times through a polycarbonate filter (Whatman Nucleopore) with 50 nm pore size and sonicated 20 min before use. Lipids contain high amount of PSM and cholesterol may be heated during the extrusion and sonication process to achieve uniform vesicle sizes. All vesicles were on the order of 100 nm in diameter as measured by dynamic light scattering measurements (Zetasizer Nano, Malvern Instruments, Worcestershire, UK).

3. PDMS Well Fabrication

PDMS monomer and crosslinker were mixed in a ratio of 10:1. After being stirred and degased, the mixture was poured in a Petri dish and baked at 85°C overnight. The thin sheet of PDMS was then cut into small pieces such that they fit over the glass coverslips. Each piece had a hole punched at the center of diameter ~ 1 cm. The PDMS piece was attached on a clean glass coverslip to form a well to hold various solutions used here.

4. Characterization of Diffusion in Supported Lipid Bilayer by Fluorescence Recovery After Photobleaching (FRAP)

To examine the diffusivity of biomolecules within the supported lipid bilayers, FRAP experiments were performed using an inverted Zeiss Axiovert Observer. Z1 fluorescence microscope. The microscope was coupled with a α Plan-Apochromat 20x objective, a CCD camera (Hamamatsu ImageEM, model C9100-13, Bridgewater, NJ), a microscope light source (X-Cite 120, Lumen Dynamics Group Inc., Canada) and a Argon-Krypton tunable laser (CVI Melles Griot, model 643-AP-A01). The appropriate wavelength for each labeled species was chosen to photobleach the SLB with a ~10 μm diameter spot under 40x objective by the laser for 3 seconds. The fluorescence intensity of the bleached spot as it recovers with time was recorded for 15 minutes and determined after background subtraction and normalization to reduce artifacts resulting from background photobleaching,. The recovery data was then fit by following the method of Soumpasis[198]. The equation used to calculate the diffusivity is, $D = \frac{w^2}{4t_{1/2}}$, where w is the full width at half-maximum of the Gaussian profile of the focused laser beam and $t_{1/2}$ is the characteristic diffusion time.

5. Preparation of glass coverslips used as supports for supported bilayers.

Glass coverslips were used as the substrate for supported lipid bilayers for fluorescence studies. 25 mm x 25 mm glass coverslips (No. 1.5, VWR) were cleaned in piranha solution for 10 min. Piranha solution consists of 45 ml 50% wt H_2O_2 (Sigma) and 105 ml H_2SO_4 (BDH chemicals). After cleaning, glass coverslips were rinsed with copious amounts of deionized water for 30 min. Deionized water was generated by an Ultrapure water system (Siemens Purelab). Clean glass coverslips were stored in deionized water and dried with nitrogen gas before each use.

6. Measuring partitioning behavior of biomolecules in heterogeneous bilayers

To better optimize the design of the extraction channel for desired separation efficiency, a thorough study on how various lipid phases impact the partitioning kinetics of membrane-bound species is necessary. Biological studies suggest that the partitioning behavior of biomolecules into or out of a particular lipid phase (lipid raft or liquid-disordered) is regulated by several factors, such as species properties and bilayer rigidity[41].To study these impacts on partitioning, we measure the overall intrinsic partitioning (at equilibrium) of Alexa 594-G_{M1} and Bodipy-DHPE in two types of heterogeneous bilayer systems: POPC system and DOPC system. For POPC system, these compositions are 70/20/10 molar ratio of POPC/PSM/Chol, denoted as $l_{d,\ POPC,}$ phase, and 60/40 molar ratio of PSM/Chol, denoted as $l_{o,\ POPC}$ phase. For DOPC system, these compositions are 63/30/7 molar ratio of DOPC/PSM/Chol, denoted as $l_{d,\ DOPC,}$ phase, and 10/40/50 molar ratio of DOPC/PSM/Chol, denoted as $l_{o,\ DOPC}$ phase. We found that the distinct preferences of the two biomolecules toward lipid raft demonstrate great examples of the partitioning behaviors of raftophilic and raftophobic membrane species.

The main difference in between the two heterogeneous bilayer systems used in this study is the bilayer order of lipid rafts compared to its coexisted liquid-disordered phases. We first examined the order of bilayers in each phase by measuring its lateral diffusivity. Table A1 shows the diffusivities of Alexa-594 G_{M1} and BODIPY-DHPE in liquid-disordered phases and lipid rafts in both POPC-based and DOPC-based systems. The ratio of the diffusivities in liquid-disordered phases and lipid rafts indicates the difference of bilayer rigidity of lipid rafts over liquid-disordered phase. The result suggests that POPC system is considered to be "more heterogeneous" than DOPC system, thus we expect that the partitioning behaviors of biomolecules in POPC system will be more distinct due to the significant difference of bilayer rigidity between lipid raft and liquid-disordered phases.

Table A1. Average diffusivities of both Alexa-594 G_{M1} and BODIPY-DHPE in various lipid phases

Diffusivity ($\mu m^2/s$)	**POPC l_d**	**POPC l_o**	**l_d / l_o**	**DOPC l_d**	**DOPC l_o**	**l_d / l_o**
BODIPY DHPE	0.85±0.09	0.10±0.02	8.7	1.10±0.20	0.25±0.05	4.4
Alexa 594-G_{M1}	0.94±0.21	0.10±0.01	9.4	1.39±0.09	0.25±0.04	5.8

To further quantify the partitioning behaviors of biomolecules in two-phase coexistent bilayers, we define the partitioning coefficient, k as the ratio of the concentration in the lipid ordered phase (l_o) region over the concentration in the lipid disordered phase region (l_d) after the system has reached equilibrium, as shown below:

$$k = \frac{C_{lo}}{C_{ld}} \qquad \text{(Eq. A1)}$$

C_{lo} and C_{ld} are the concentration of biomolecules in the lipid ordered phase region and lipid disordered region, respectively. At equilibrium, C_{lo} and C_{ld} should remain constant and the concentration in the transition zone (TZ) varies linearly in this region, as shown in Figure. A1.

The reported *K* values for both Alexa-594 G_{M1} and BODIPY-DHPE are listed in Table A2. The results suggest that both biomolecules present more distinct partitioning in lipid raft/liquid-disorder phase in POPC system, which indicates that order of lipid bilayer is an important factor that decides the extent of biomolecules partitioning in a specific lipid phase.

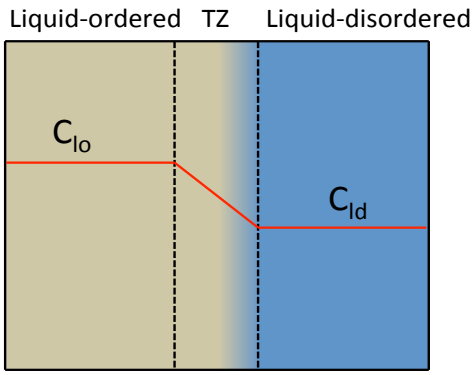

Figure A1. The illustration of concentration (red line) change in the transition zone (TZ) in between bulk raft and bulk liquid-disordered phase. The partitioning coefficient, ***k***, is defined as the ratio of concentration in lipid ordered phase (lipid raft) over liquid-disordered phase.

Table A2. Reported values of partitioning coefficient, *k*, of Alexa-594 G_{M1} and BODIPY-DHPE in both systems.

Partitioning coefficient, *k*	**BODIPY DHPE**	**Alexa 594-G_{M1}**
POPC-based system	0.6	1.96
DOPC-based system	0.81	1.27

Appendix B

1. Materials and Methods.

1.1 QCM-D modeling to detect adsorbed mass on the quartz sensor.

QCM-D is a well-known technique to detect the adsorbed mass, Δm, on the crystal surface[118]. Several models have been developed to investigate mass and viscoelastic properties of the adsorbed film by fitting resonant frequency and dissipation signals:

- Sauerbrey Model

If the adsorbed film is rigid enough, which indicates that ΔD is smaller than $1x10^{-6}$ Hz, the Sauerbrey equation can be applied to obtain the adhered mass, Δm:

$$\Delta m = C_m \frac{\Delta f_z}{z} \qquad (1)$$

Δm is the adsorbed mass on the crystal surface, C_m is a constant (-17.7 $\frac{ng}{cm^2 \cdot Hz}$ for crystal with f = 5 MHz), and Δf_z is the shift of frequency at z overtone (z = 1, 3, 5 , 7, 9, 11, 13). The Sauerbrey equation describes the linear relationship between the adsorbed mass and the change of resonant frequency for rigid adhered layers.

- One-layer Voigt-Voinova model

If the adhered layer is "soft" ($\Delta D > 1\times10^{-6}$Hz), the Sauerbrey equation is no longer valid. Instead, the Voigt-Voinova model is usually used to model the adsorbed mass along with several mechanical properties of the adlayer. The Voigt-Voinova model treats the adlayer and the rigid crystal as a coupling of a spring and a dashpot, with the assumptions of uniform adlayer thickness, uniform adlayer density, homogeneous viscoelastic properties and a no slip, Newtonian liquid in the bulk. The model includes four mechanical effects of the adlayer: thickness, density, shear elasticity and viscosity, and the equations are shown as following:

$$\Delta f \approx -\frac{1}{2\pi\rho_q h_q}\left[h_1\rho_1\omega - 2h_1\left(\frac{\eta_b}{\delta_b}\right)^2\frac{\eta_j\omega^2}{{\mu_1}^2+\omega^2{\eta_1}^2}\right] \quad (2)$$

$$\Delta D \approx \frac{1}{4\pi f\rho_q h_q}\left[2h_1\left(\frac{\eta_b}{\delta_b}\right)^2\frac{\mu_1\omega}{{\mu_1}^2+\omega^2{\eta_1}^2}\right] \quad (3)$$

$$\tan(\delta) = \frac{\omega\eta}{\mu} \quad (4)$$

Where ρ_q, ρ_f are the density of the crystal and film, h_q, h_1 are the thickness of the crystal and film, χ is the ratio of the storage modulus and the loss modulus, and δ is the penetration depth. $\tan(\delta)$ represents the ratio between the viscosity and shear modulus, which reflects the viscoelasticity of material. The smaller value of $\tan(\delta)$ indicates a more rigid material attached on the crystal, and vice versa.

We used the Voigt-Voinova model built in the commercial software, Q-tool, to obtain the adsorbed mass on the sensor since most of the data shown in this study contained the shift of dissipations (ΔD) much greater than $1\times10^{-6}Hz$. Two overtones of frequency shifts and dissipation changes, $(\Delta f_3, \Delta D_3, \Delta f_5, \Delta D_5)$, were fitted to the Voigt-Voinova model to generate the information of thickness (h_1), shear elasticity and viscosity. The parameters used in the software were: film density (ρ_f): 1100 kg/m^3, fluid density: 1000 kg/m^3, fluid viscosity: 0.001 kg m^{-1}s^{-1}. The mass of the adsorbed film is the product of the film thickness and density:

$$\Delta m = h_1\times\rho_f \ \left(\frac{ng}{cm^2}\right) \quad (5)$$

- Two-layer Voigt-Voinova model[282]

If the adhered layer is predominately heterogeneous, a two-layer Voigt-Voinova model can be applied to capture the detailed viscoelastic properties of different layered films (**Fig. 1 (b)**). For two thin viscoelastic adhered layers in a bulk fluid, the changes in frequency and dissipation at various overtones are:

$$\Delta f \approx -\frac{1}{2\pi\rho_q h_q}\left\{\sum_{j=1,2}\left[h_j\rho_j\omega - 2h_j\left(\frac{\eta_b}{\delta_b}\right)^2\frac{\eta_j\omega^2}{{\mu_j}^2+\omega^2{\eta_j}^2}\right]\right\} \quad (6)$$

$$\Delta D \approx \frac{1}{4\pi f\rho_q h_q}\left\{\sum_{j=1,2}\left[2h_j\left(\frac{\eta_b}{\delta_b}\right)^2\frac{\mu_j\omega}{{\mu_j}^2+\omega^2{\eta_j}^2}\right]\right\} \quad (7)$$

By fitting frequency shifts and dissipation changes at various overtones $(\Delta f_3, \Delta D_3 \ldots . \Delta f_{13}, \Delta D_{13})$ to two-layer Voigt-Voinova model, viscoelastic properties $(\eta_1, \eta_2, \mu_1, \mu_2)$ and film thickness (h_1, h_2) of both top and bottom layers can be extracted. The fitting process was performed using an optimization tool of a commercial software package (MATLAB 8.3, The MathWorks Inc., Natick, MA, 2014a). Matlab's *fmincon* function was performed to find the minimum of the following constrained nonlinear multivariable function:

$$F(\eta_1, \eta_2, \mu_1, \mu_2, h_1, h_2) = \sum_{n=3,5\ldots13}\left(\Delta f_n^{exp} - \Delta f_n^{calculated}\right)^2 + \left(\Delta D_n^{exp} - \Delta D_n^{calculated}\right)^2 \quad (8)$$

Due to the nonlinear nature of the *F* function, various sets of fitted parameters were found, indicating the existence of multiple local minimums. To determine the most appropriate solution, we constrained the range of the viscoelastic parameters and film thickness to conform to physical constraints: $8.9\times10^{-4}Pa\cdot s \leq \eta \leq 1\times10^{-1}Pa\cdot s$, $10^4 Pa \leq \mu \leq 5\times10^6 Pa$, $1^{-9}m \leq \mu \leq 1^{-7}m$. Within the range specified, one specific set of fitted parameter was determined by the fitting tool to reach a global minimum. The density for both of the films was assumed to be 1100 kg/m^3.

1.2 OMV size and surface charge characterization.

The size and zeta potential of OMVs and pegylated liposomes in PBS buffer were measured by dynamic light scattering and electrophoresis (Malvern). The size distributions and zeta potential measurements are provided in the Supplementary Information.

1.3 Fluorescent labeling of OMVs and liposomes.

In order to visualize the formation of bacteria-like SLBs and to measure the diffusivities of the subsequent bilayers, OMVs were first fluorescently labeled with Octadecyl Rhodamine (R18). R18 is a red-emitting fluorophore (Molecular Probes, Eugene, OR), which intercalates into membranes. 300 μL of OMV solution was incubated with 1 μL 0.18 mM R18 in a bath sonicator (Model # BD2500A-DTH; VWR) for 15-20 min on the lowest setting. The solutions were then centrifuged (Eppendorf, Centrifuge 5451C, Hauppauge, NY) through a G-25 spin column for 2 min to remove excess free R18.

1.4 Formation of SLB from pure liposomes.

SLBs self-assemble on clean glass by the vesicle fusion method[114]. Liposome solutions were added to a PDMS well and incubated for 10-15 min. PBS buffer was used to rinse the samples after incubation to remove excess lipid vesicles. In order to visualize the SLB formation and measure the mobility of lipids, liposomes (or OMVs) were labeled with R18 prior to bilayer formation, using the labeling procedure described above.

2. OMV size and surface charge characterization

The size and zeta potential of OMVs and pegylated liposomes in PBS buffer were measured by dynamic light scattering and electrophoresis. The size distributions of OMVs and DOPC with 0.5 mol% PEG (5k)-PE liposomes are plotted in Figure B1a, which shows that both vesicles are similar sizes with average hydrodynamic diameters around 70-100 nm. The zeta potential results (Fig. B1b) show that OMVs are more negatively charged than DOPC with 0.5

mol% PEG (5K)-PE liposomes in PBS. The negative charge of OMVs results from negatively-charged lipopolysaccharides, which makes up approximately 30 wt% of bacterial outer membrane, as well as protein content. We also used a ZetaSizerNano (Malvern) to determine concentration of the native OMV samples. Duplicate runs (n>3) were performed on each sample and three samples were measured. We found the correlation of OMV protein content (BCA assay) and particle number to be 1μg protein /10^9 particles. Figure B1c shows an example of concentration measurement using an OMV sample with 1.6 □g/mL protein concentration (BCA assay), with the average particle concentration to be $1.58 \times 10^9 \pm 1.27 \times 10^7$ particles /mL.

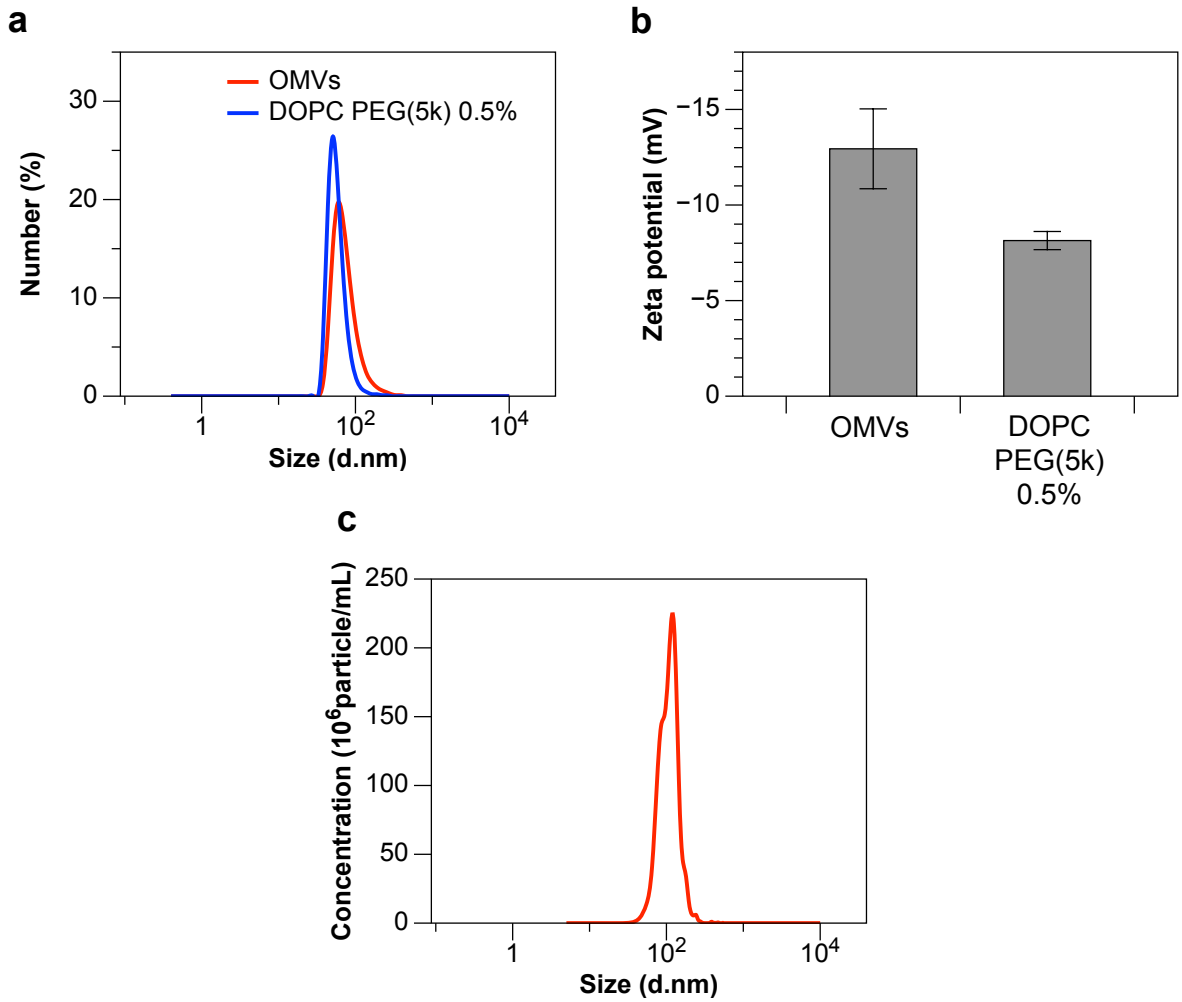

Figure B1. (a) Distribution of particle diameters and (b) zeta potential of OMVs and DOPC with 0.5 mol% PEG(5K)-PE liposomes in PBS buffer solution. Particle size distribution was determined by dynamic light scattering and zeta potential was obtained using electrophoresis. The buffer conditions were 5 mM phosphate buffered saline

(PBS) with 150 mM NaCl at a pH of 7.4. (c) Particle concentration profiles for OMVs with 1.6 □g/mL protein concentration.

3. OMV adsorption measurement using QCM-D

To estimate the surface coverage of OMVs, we formed a saturated monolayer of intact OMVs on the sensor and monitored the adsorption process using QCM-D. The QCM-D measurement and the corresponding mass curve are shown in Figure B2.

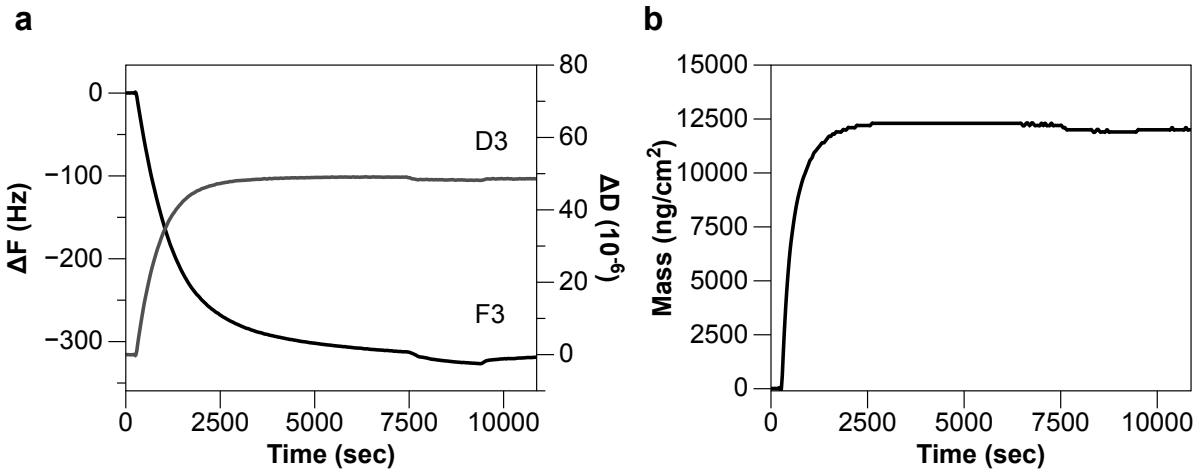

Figure B2. Typical result of a QCMD OMV adsorption experiment. While flowing, OMVs gradually adsorbed on the sensor, indicated by declined frequency and increased dissipation, and formed an unruptured OMV monolayer. The signals of frequency and dissipation were converted to mass curve (b) by fitting with one-film Voigt-Voinova model.

4. OMV surface coverage discussion

The surface coverage calculation performed using eq. (1) in the main text was based on one simple assumption that the acoustic response obtained from QCM-D is proportional to the biomolecule mass. Note that acoustic response from QCM-D (M_{QCM}) is the combination of both dry biomolecule mass (M_d) and the coupled water mass (M_w):

$$M_{QCM} = M_d + M_w \tag{9}$$

By assuming M_{QCM} is proportional to M_d, we are stating that the hydration level, H, remains constant regardless of molecular level of OMV:

$$H = 1 - \frac{M_d}{M_{QCM}} = constant \quad (10)$$

$$\theta_H = \frac{0.54 \times M_{QCM}}{M_{QCM,sat}} \quad \text{(eq. (4.1), Chapter 4)}$$

θ_H denotes the surface coverage calculated based on constant hydration (H) assumption. This assumption provides us a simple way to estimate OMV surface coverage, rupture percentage, and hence, the bacterial contents in OM-SB. However, previous literature has shown that this assumption is not valid under all circumstances. Cho et al. (2009)[286] have used complementary acoustic (QCM-D) and optical (SPR) techniques to monitor the hydration level of lipid vesicles adsorbed on a Au sensor. Their results suggest that the coupled water content per lipid vesicle varies at different adsorption stages. The hydration level stays high at low surface coverage and gradually decreases as more materials adsorbed on the surface. By assuming constant hydration level at all times, we will overestimate the biomolecular mass at low surface coverage, which will effectively distort the OMV rupture percentage calculation.

To further correct the artifacts caused by the assumption (eq (10)), we applied the theoretical model developed by Bingen et al (2008)[287] to describe the solvation of OMV at different surface coverage. Bingen and colleagues developed pyramid models to simulate the adsorption of vesicles on a QCM sensor. By assuming the space occupied by a vesicle with the solvent coupled to it to be a truncated pyramid, they were able to calculate the hydration level (H) as a function of surface coverage and parameters that describe the adsorbed vesicles:

$$H = \frac{v - M_w {\rho_p}^{-1}}{v + M_w({\rho_{H_2O}}^{-1} - {\rho_p}^{-1})} \quad (11)$$

$$v = func(\theta, r, z, l) \quad (12)$$

M_w is the molecular weight of the vesicle, ρ_{H_2O} and ρ_p are the density of buffer and particles, respectively. v is the average volume of the vesicle and its coated solvent, which is a function of

surface coverage (θ) and parameters (z, r, l) describing the dimensions of the adsorbed vesicles. z is the height of the adsorbed vesicle, while r and l are the dimensions characterize the footprint of the truncated pyramid. To apply this theoretical model to describe the adsorption of OMVs, we first need to obtain the following properties for the adsorbed OMVs: M_w, ρ_p, z, r, *and* l. We estimated M_w and ρ_p of the OMV to be 40,000 kDa and 1100 g/cm^3, assuming vesicle size in a range of with 70-100 μm and membrane thickness of 5 nm. We also estimated z, the height of the adsorbed vesicles, to be 110 μm based on the estimated thickness of OMV adsorbed monolayer from the Voigt viscoelastic model. However, we have very limited information on how to predict r and l, the other two dimensions describing the footprint of the adsorbed OMVs. To overcome this barrier, we developed a three-dimensional COMSOL model to simulate OMV adsorption kinetics and further determine the parameters r and l. Note that while COMSOL model can successfully predict OMV surface coverage at different time courses, the model was developed under the assumption that vesicles were uniformly distributed. By not taking into account the random spatial distribution of adsorbed OMVs, we may miss significant OMV adsorption kinetics. This limitation motivates us to first fit the COMSOL simulation result in the "uniform adsorption" pyramid model (model 2 in Bingen et al) to determine parameters r and l. We then fit all the parameters to the modified pyramid model with random adsorbent distribution (model 3 in Bingen et al) to estimate the relationship of hydration level and surface coverage.

4.1 OMVs adsorption on QCM-D sensor simulated using COMSOL

4.1.1 Model development

I. Geometry

In the QCM-D system, the SiO_2 sensor (inner diameter 11 mm) was mounted in the liquid cell

chamber (height 0.4 mm), and the chamber volume is around 40 μL. The geometry of the system is shown in Figure B3.

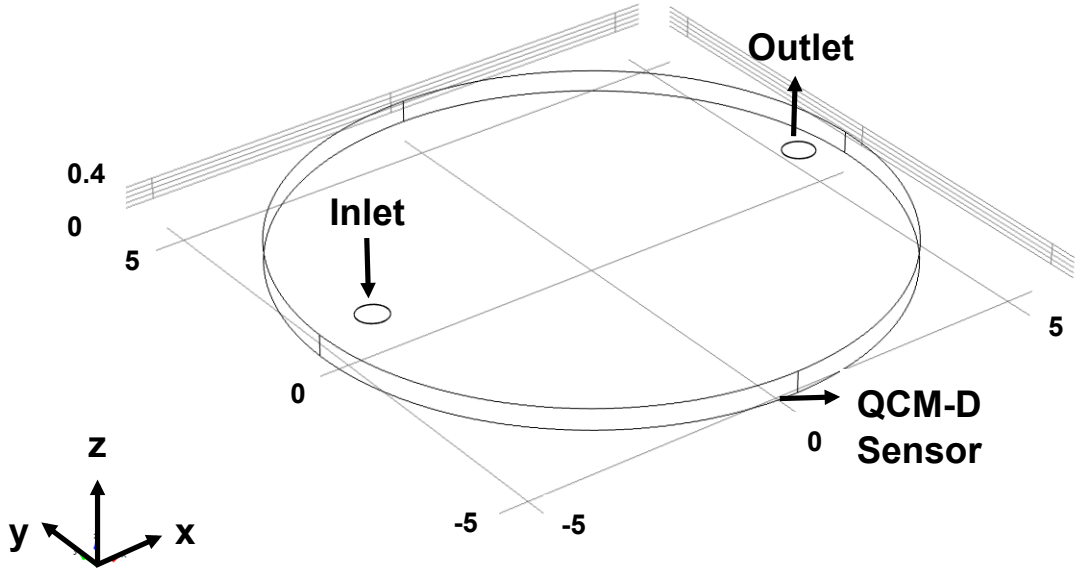

Figure B3: The geometry of the QCM-D flow chamber. The bottom surface is the adsorption surface site that generates frequency and dissipation changes. The OMVs solution were sent to the chamber through inlet and flowed out from outlet.

II. Physical Models

Three physical models were chosen in this study: Laminar flow (3D), transport of diluted species (3D), and surface reaction (2D). First, laminar flow physics was solved with stationary study, and the resulting 3D velocity profiles were input to transport of diluted species and surface reaction physics. The transport and surface reaction physics were solved in a time-dependent manner.

Physics 1: Laminar Fluid Flow

The flow in the chamber is laminar flow ($Re \sim O(1)$) and governed by Navier-Stokes equation:

$$\rho u \cdot \nabla \mathrm{u} = \nabla \cdot \left[-pI + \eta(\nabla \mathrm{u} + (\nabla \mathrm{u})^T) - \left(\frac{2\eta}{3}\right)(\nabla \cdot \mathrm{u})\mathrm{I}\right] \quad (13)$$

$$\nabla \cdot (\rho u) = 0 \quad (14)$$

u is solution velocity $\left(\frac{m}{s}\right)$. ρ (density $\left(\frac{kg}{m^3}\right)$) and η (viscosity $\left(\frac{kg}{m \cdot s}\right)$) are built-in properties of water at 24 ℃. P is the pressure (Pa).

The boundary conditions are: 1) Inlet: constant flow rate, 100 μL/min. 2) Outlet: P = 1 atm. 3) Walls: no flow, and the initial condition is: $u = 0$ (no flow at time zero).

The resulting continuous flow profiles are shown in Figure B4. The solution flowed in and exited out from the chamber at the velocity of 100 μL/min. The simulated results suggest that the flow rate experiences significant drop: 1) from the inlet/outlet to the center and 2) from the top to down along the z direction. This steady-state, unperturbed laminar flow profile was then used in the following studies to simulate OMVs adsorption on the sensor.

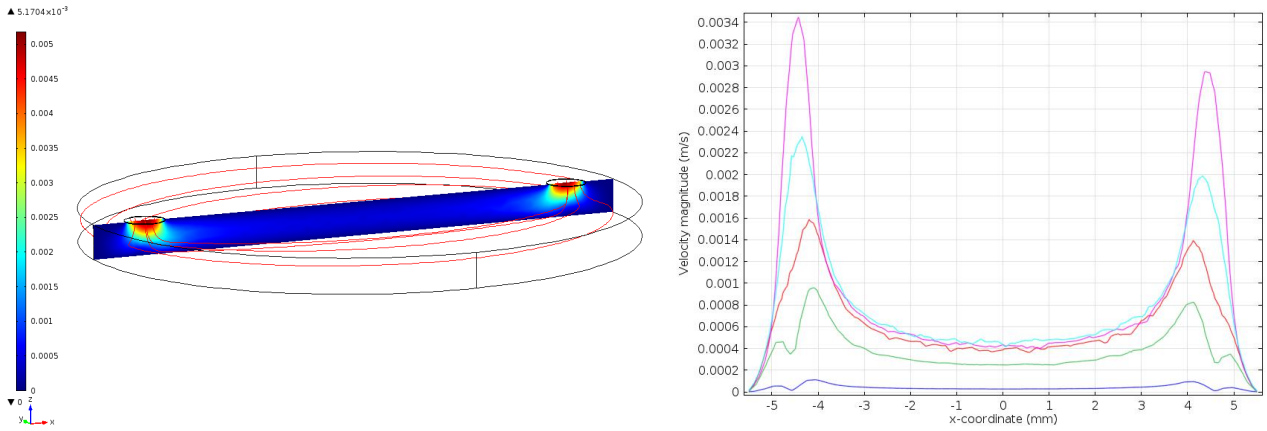

Figure B4. (Left) The magnitude of velocity field of the *zx* surface and the streamlines in the chamber. (Right) The magnitude of velocity field along (*x* = -5.5 mm, *y* = 0 mm) to (*x* = 5.5 mm, *y* = 0 mm) at different *z* slices, which corresponds to the surface showed in Figure 2. *z* ranges from 0.01 mm, 0.1 mm, 0.2 mm, 0.3 mm, and 0.4 mm.

Physics 2: Mass Transport in the stream

The governing equation of the transport of free OMVs (V) in the solution is described as below:

$$\frac{\partial C_V}{\partial t} + \nabla \cdot (-D_V \nabla C_V) + u \cdot \nabla C_V = 0 \quad (15)$$

where D_V is the diffusivity $(\frac{m^2}{s})$ and u is the velocity vector $(\frac{m}{s})$.

The boundary conditions are: 1) Inlet: $C_V = C_{V0}$, where C_{V0} was the solution concentration sent to the chamber. From t = 0 to t = 5 mins, the OMVs solution was fresh (C_{V0} = 0.01 mg/ml). For t > 5 mins, since the OMVs solution was recycled to the chamber, C_{V0} was the outlet concentration, C_{out}. 2) Outlet: $n \cdot (-D_V \nabla C_V) = 0$. 3) Reactive sensor surface: $N_C = -R_{ad}$. 4) Other impenetrable surfaces: $n \cdot (-D_V \nabla C_V + C_V u) = 0$. The initial condition was $C_V = 0$, which means that the concentration of the bulk at the beginning of the process was set to zero.

Physics 3: Surface Reaction

The governing equation for OMVs adsorbed on the surface can be expressed as below, including OMV surface diffusion and the adsorption reaction:

$$\frac{\partial C_s}{\partial t} + \nabla \cdot (-D_s \nabla C_s) = R_{ad} \tag{16}$$

where C_s is the concentration of the adsorbed OMVs, D_s is the surface diffusivity and R_{ad} is OMV adsorption rate. If the surface diffusion was assumed to be zero, the governing equation for the surface concentration can be written as:

$$\frac{\partial C_S}{\partial t} = R_{ad} \tag{17}$$

Free OMVs (V) in the solution could adsorb on the surface site (*S*) on the QCM-D sensor irreversibly:

$$V + S \xrightarrow{K_{on}} VS \tag{18}$$

Where *VS* represents the OMVs adsorbed on the surface. The rate of adsorption can further be defined as:

$$R_{ad} = K_{on} C_V \Gamma_s (1 - \theta) \tag{19}$$

$C_V \left(\frac{mg}{m^3}\right)$ is the concentration of free OMVs in the solution on the surface, Γ_s is the total active binding site for OMVs (mg/m^2), and θ is the surface fraction of VS. Since both K_{on} *and* Γ_s

are unknowns in this study, we further combine these two parameters to one unknown constant A:

$$R_{ad} = AC_V(1-\theta) \tag{20}$$

$$A = K_{on}\Gamma_s$$

By integrating eq. (16) and (20), the material balance for the adsorbed OMVs on the surface can be written as:

$$\frac{\partial C_S}{\partial t} = AC_V(1-\theta) \tag{21}$$

4.1.2 COMSOL Simulation results and discussion

The constraint for the simulation model is that simulated surface coverage should saturate at the same time point as the experimental surface coverage, which is around t = 1600 sec under the given flow rate and solution concentration. By tuning the unknown parameter *A* in eq. 12, we are able to determine the surface coverage profile to reach saturation at the desired time. As shown in Figure B5, the experimental surface coverage data calculated based on the assumption (eq.(2)), θ_H, is higher than the simulated result, θ_{COMSOL}. This finding corresponds well with the proposed mechanism from the literature: the biomolecular mass will be overestimated at low surface coverage if hydration is considered to be constant. Fig. S3 also depicts the deviation of these two coverage profiles over the time course.

By expressing eq. 11 as eq. (22):

$$\theta_{model} = \theta_H \frac{1-H}{1-H_{sat}} \tag{22}$$

we can then fit the relationship of θ_H and θ_{COMSOL} to the "uniform adsorption" pyramid model (model 2 in Bingen et al) to determine the parameters *r* and *l*. The best fits are shown in Figure B5a and *r* and *l* are determined as 35 nm and 24.6 nm respectively. Finally, we fitted *r* and *l* to simulate the adsorption of OMVs by a random sequential adsorption (RSA) following a Monte

Carlo algorithm[299]. The relationship between surface coverage $\theta_{model,\ RSA}$ and θ_H can then be computed (Fig. S5b) and used to correct the artifacts caused by the assumption (eq. (10)).

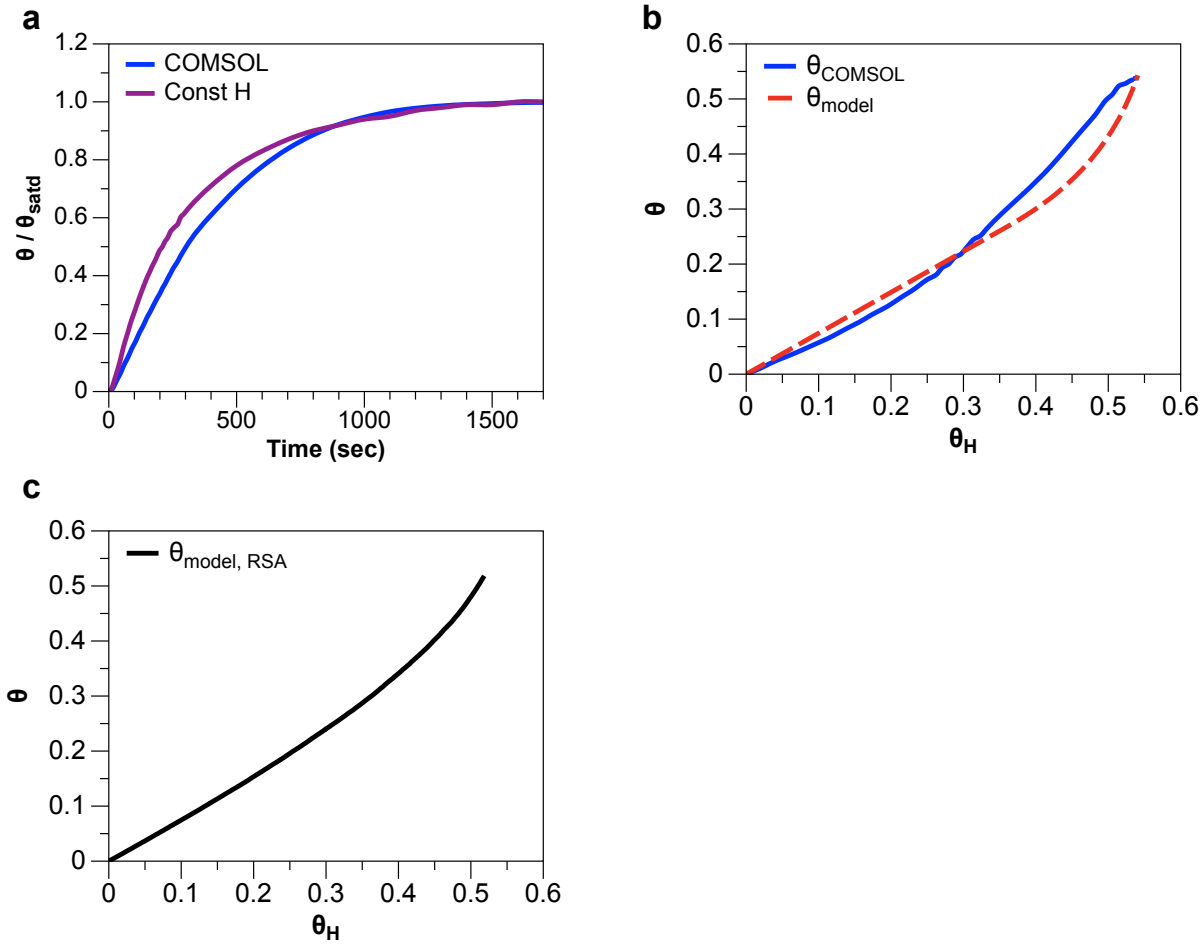

Figure B5. (a) The surface coverage from: (purple) the calculation using the experimental QCM-D data based on the assumption described in eq.10, and (blue) the simulation result using COMSOL model. (b) (blue) The relationship of θ_H versus θ_{COMSOL} and (red) the fitting results showing the relationship of θ_H and θ_{model}. (c) The final correlation curve used to correct the θ_H and $\theta_{model,\ RSA}$.

5. QCM-D responses of all the overtones for OM-SB formation and the following polymyxin B interaction

We performed QCM-D experiments to monitor the interaction of polymyxin B towards OM-SB, ranging from the 3rd to 13th overtones. The QCM-D measurements including OM-SB formation and the following polymyxin B interaction are shown in Figure B7.

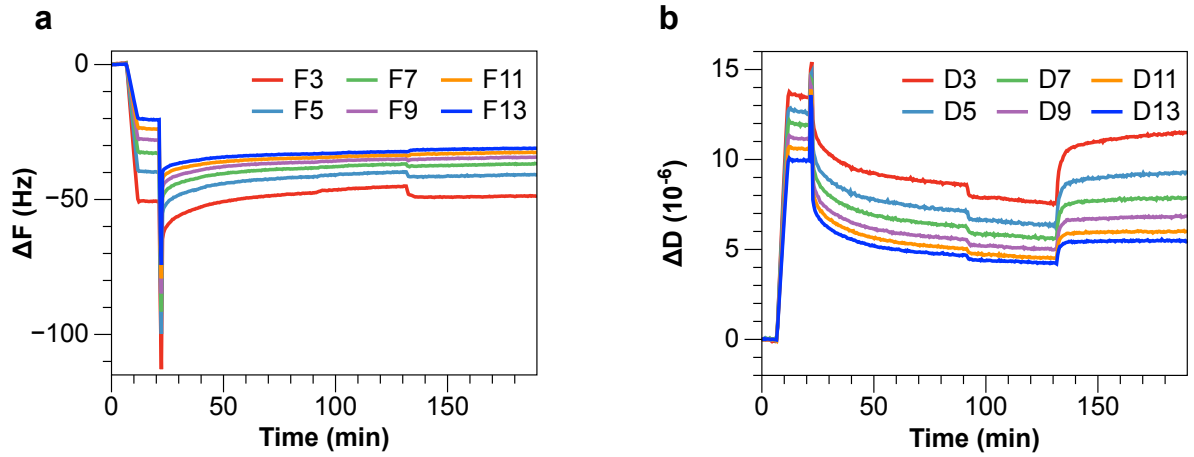

Figure B6. The 3rd to 13th overtones QCM-D responses for OM-SB formation and the following polymyxin B interaction. (Left) Normalized frequency response and (Right) the corresponding dissipation shifts.

B6. The QCM-D control experiment of adding polymyxin B to PEG-SLB

To exclude the possibility that non-specific artifact of polymyxin B to PEG-SLB are present, we performed QCM-D experiments to confirm that no signal was detected with the addition of PMB to PEG-SLB.

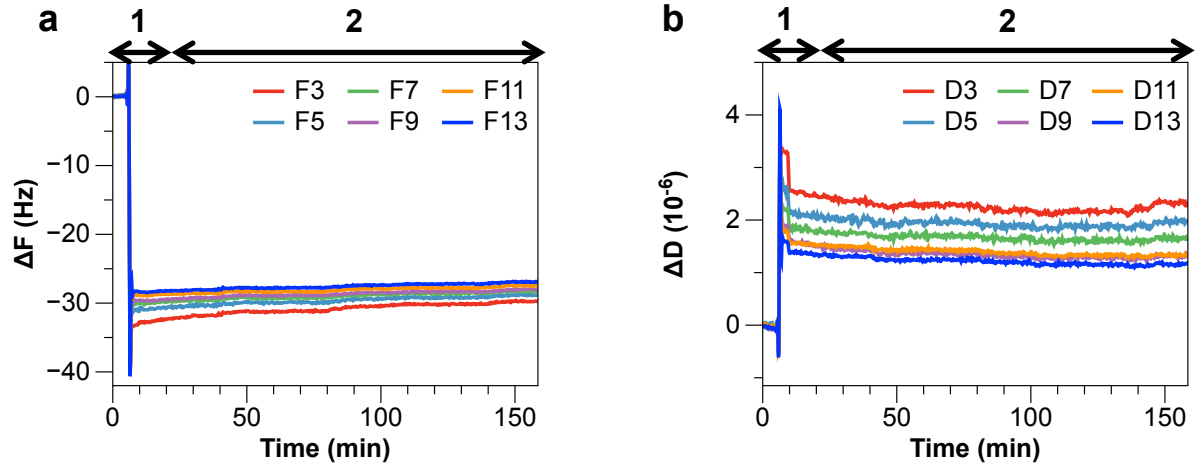

Figure B7. The QCM-D measurement showing PMB has no effect on PEG-SLB at the giving PMB concentrations. PEG-SLB was first formed (1) and PMB solution was then added into the system (2). The PMB concentrations range from: 0.001mg/ml, 0.01mg/ml, 0.05mg/ml, and 0.1mg/ml; each batch of solution was followed for 30 minutes. (a) Normalized frequency response and (b) the corresponding dissipation shifts.

REFERENCES

1. Lundstrom, K. Structural genomics on membrane proteins: mini review. *Comb Chem High Throughput Screen* **7,** 431–439 (2004).

2. Overington, J. P., Al-Lazikani, B. & Hopkins, A. L. How many drug targets are there? *Nat. Rev. Drug Discov.* **5,** 993–996 (2006).

3. Cooper, M. A. Optical biosensors in drug discovery. *Nat. Rev. Drug Discov.* **1,** 515–28 (2002).

4. Amzel, L. M. Structure-based drug design. *Curr. Opin. Biotechnol.* **9,** 366–369 (1998).

5. Seddon, A. M., Curnow, P. & Booth, P. J. Membrane proteins, lipids and detergents: not just a soap opera. *Biochim. Biophys. Acta* **1666,** 105–17 (2004).

6. George, S. R., O'Dowd, B. F. & Lee, S. P. G-protein-coupled receptor oligomerization and its potential for drug discovery. *Nat. Rev. Drug Discov.* **1,** 808–20 (2002).

7. Verlinde, C. & Hol, W. Structure-based drug design: progress, results and challenges. *Structure* 577–587 (1994).

8. Congreve, M. & Marshall, F. The impact of GPCR structures on pharmacology and structure-based drug design. *Br. J. Pharmacol.* **159,** 986–96 (2010).

9. Lee, A. G. How lipids affect the activities of integral membrane proteins. *Biochim. Biophys. Acta* **1666,** 62–87 (2004).

10. Schonenbach, N. S., Hussain, S. & O'Malley, M. A. Structure and function of G protein-coupled receptor oligomers: implications for drug discovery. *Wiley Interdiscip. Rev. Nanomedicine Nanobiotechnology* **7,** 408–427 (2014).

11. Reimhult, E. & Kumar, K. Membrane biosensor platforms using nano- and microporous supports. *Trends in Biotechnology* **26,** 82–89 (2008).

12. Andersson, A.-S., Glasmästar, K., Sutherland, D., Lidberg, U. & Kasemo, B. Cell adhesion on supported lipid bilayers. *J. Biomed. Mater. Res. A* **64,** 622–629 (2003).

13. Benamara, H., Rihouey, C., Jouenne, T. & Alexandre, S. Impact of the biofilm mode of growth on the inner membrane phospholipid composition and lipid domains in Pseudomonas aeruginosa. *Biochim. Biophys. Acta* **1808,** 98–105 (2011).

14. Hancock, J. Lipid rafts: contentious only from simplistic standpoints. *Nat. Rev. Mol. Cell Biol.* **7,** 5658–5659 (2006).

15. Lentz, B. R., Barrow, D. a & Hoechli, M. Cholesterol-phosphatidylcholine interactions in multilamellar vesicles. *Biochemistry* **19,** 1943–1954 (1980).

16. Ipsen, J. H., Karlström, G., Mouritsen, O. G., Wennerström, H. & Zuckermann, M. J. Phase equilibria in the phosphatidylcholine-cholesterol system. *Biochim. Biophys. Acta* **905,** 162–172 (1987).

17. Lingwood, D. & Simons, K. Lipid rafts as a membrane-organizing principle. *Science* **327,** 46–50 (2010).

18. Brown, D. A. & Rose, J. K. Sorting of GPI-anchored proteins to glycolipid-enriched membrane subdomains during transport to the apical cell surface. *Cell* **68,** 533–544 (1992).

19. Harder, T., Scheiffele, P., Verkade, P. & Simons, K. Lipid domain structure of the plasma membrane revealed by patching of membrane components. *J. Cell Biol.* **141,** 929–942 (1998).

20. Fujiwara, T., Ritchie, K., Murakoshi, H., Jacobson, K. & Kusumi, A. Phospholipids undergo hop diffusion in compartmentalized cell membrane. *J. Cell Biol.* **157,** 1071–1081 (2002).

21. Kusumi, A., Koyama-Honda, I. & Suzuki, K. Molecular dynamics and interactions for creation of stimulation-induced stabilized rafts from small unstable steady-state rafts. *Traffic* **5,** 213–230 (2004).

22. Gidwani, A., Holowka, D. & Baird, B. Fluorescence anisotropy measurements of lipid order in plasma membranes and lipid rafts from RBL-2H3 mast cells. *Biochemistry* **40,** 12422–12429 (2001).

23. Ge, M. *et al*. Ordered and disordered phases coexist in plasma membrane vesicles of RBL-2H3 mast cells. An ESR study. *Biophys. J.* **85,** 1278–1288 (2003).

24. Richter, M., Hedegaard, M., Deckert-Gaudig, T., Lampen, P. & Deckert, V. Laterally resolved and direct spectroscopic evidence of nanometer-sized lipid and protein domains on a single cell. *Small* **7,** 209–214 (2011).

25. Henriques, R. & Mhlanga, M. M. PALM and STORM: What hides beyond the Rayleigh limit? *Biotechnol. J.* **4,** 846–857 (2009).

26. Owen, D. M., Magenau, A., Williamson, D. & Gaus, K. The lipid raft hypothesis revisited - new insights on raft composition and function from super-resolution fluorescence microscopy. *BioEssays* **34,** 739–747 (2012).

27. Owen, D. M. *et al*. PALM imaging and cluster analysis of protein heterogeneity at the cell surface. *J. Biophotonics* **3,** 446–454 (2010).

28. Wu, J. *et al*. High-efficiency localization of Na(+)-K(+) ATPases on the cytoplasmic side by direct stochastic optical reconstruction microscopy. *Nanoscale* **5,** 11582–11586 (2013).

29. Mueller, V. *et al*. STED nanoscopy reveals molecular details of cholesterol- and cytoskeleton-modulated lipid interactions in living cells. *Biophys. J.* **101,** 1651–1660 (2011).

30. Kellner, R. R., Baier, C. J., Willig, K. I., Hell, S. W. & Barrantes, F. J. Nanoscale organization of nicotinic acetylcholine receptors revealed by stimulated emission depletion microscopy. *Neuroscience* **144,** 135–143 (2007).

31. Selvaraj, V. *et al*. GM1 dynamics as a marker for membrane changes associated with the process of capacitation in murine and bovine spermatozoa. *J. Androl.* **28,** 588–599 (2007).

32. Paulick, M. M. G. & Bertozzi, C. R. C. The Glycosylphosphatidylinositol Anchor: A Complex Membrane-Anchoring Structure for Proteins†. *Biochemistry* **47,** 6991–7000 (2008).

33. Asano, A., Nelson, J. L., Zhang, S. & Travis, A. J. Characterization of the proteomes associating with three distinct membrane raft sub-types in murine sperm. *Proteomics* **10,** 3494–3505 (2010).

34. Legler, D., Doucey, M. & Schneider, P. Differential insertion of GPI-anchored GFPs into lipid rafts of live cells. *FASEB J.* **19,** 73–75 (2005).

35. Gupta, N. & DeFranco, A. Visualizing lipid raft dynamics and early signaling events during antigen receptor-mediated B-lymphocyte activation. *Mol. Biol. Cell* **14,** 432–444 (2003).

36. Chiantia, S., Kahya, N., Ries, J. & Schwille, P. Effects of ceramide on liquid-ordered domains investigated by simultaneous AFM and FCS. *Biophys. J.* **90,** 4500–4508 (2006).

37. Lin, W.-C., Blanchette, C. D., Ratto, T. V & Longo, M. L. Lipid domains in supported lipid bilayer for atomic force microscopy. *Methods Mol. Biol.* **400,** 503–13 (2007).

38. Ratto, T. & Longo, M. Obstructed diffusion in phase-separated supported lipid bilayers: a combined atomic force microscopy and fluorescence recovery after photobleaching. *Biophys. J.* **83,** 3380–3392 (2002).

39. Dietrich, C., Bagatolli, L. & Volovyk, Z. Lipid rafts reconstituted in model membranes. *Biophys. J.* **80,** (2001).

40. Stottrup, B. L., Veatch, S. L. & Keller, S. L. Nonequilibrium behavior in supported lipid membranes containing cholesterol. *Biophys. J.* **86,** 2942–50 (2004).

41. Dietrich, C., Volovyk, Z. N., Levi, M., Thompson, N. L. & Jacobson, K. Partitioning of Thy-1, GM1, and cross-linked phospholipid analogs into lipid rafts reconstituted in supported model membrane monolayers. *Proc. Natl. Acad. Sci.* **98 ,** 10642–10647 (2001).

42. Lichtenberg, D., Goñi, F. M. & Heerklotz, H. Detergent-resistant membranes should not be identified with membrane rafts. *Trends Biochem. Sci.* **30,** 430–436 (2005).

43. Kusumi, A. & Suzuki, K. Toward understanding the dynamics of membrane-raft-based molecular interactions. *Biochim. Biophys. Acta - Mol. Cell Res.* **1746,** 234–251 (2005).

44. Selvaraj, V. *et al.* Segregation of micron-scale membrane sub-domains in live murine sperm. *J. Cell. Physiol.* **206,** 636–646 (2006).

45. Foster, L. J. & Chan, Q. W. T. Lipid raft proteomics: more than just detergent-resistant membranes. *Subcell. Biochem.* **43,** 35–47 (2007).

46. Soubias, O. & Gawrisch, K. *Rhodopsin-lipid interactions studied by NMR. Methods in Enzymology* **522,** (Elsevier Inc., 2013).

47. Bechara, C. *et al.* A subset of annular lipids is linked to the flippase activity of an ABC transporter. *Nat. Chem.* **7,** 255–262 (2015).

48. Lee, A. G. Lipid-protein interactions in biological membranes: A structural perspective. *Biochim. Biophys. Acta - Biomembr.* **1612,** 1–40 (2003).

49. Contreras, F., Ernst, A. M. & Wieland, F. Specificity of Intramembrane Protein – Lipid Interactions Specificity of Intramembrane Protein – Lipid Interactions. *Cold Spring Harb. Perspect. Biol.* (2011). doi:10.1101/cshperspect.a004705

50. Marius, P., De Planque, M. R. R. & Williamson, P. T. F. Probing the interaction of lipids with the non-annular binding sites of the potassium channel KcsA by magic-angle spinning NMR. *Biochim. Biophys. Acta - Biomembr.* **1818,** 90–96 (2012).

51. Gimpl, G., Wiegand, V., Burger, K. & Fahrenholz, F. Cholesterol and steroid hormones: Modulators of oxytocin receptor function. *Prog. Brain Res.* **139,** 43–55 (2002).

52. Pucadyil, T. J. & Chattopadhyay, A. Cholesterol modulates ligand binding and G-protein coupling to serotonin1A receptors from bovine hippocampus. *Biochim. Biophys. Acta - Biomembr.* **1663,** 188–200 (2004).

53. Levental, I., Lingwood, D., Grzybek, M., Coskun, U. & Simons, K. Palmitoylation regulates raft affinity for the majority of integral raft proteins. *Proc. Natl. Acad. Sci. U. S. A.* **107,** 22050–22054 (2010).

54. Diaz-Rohrer, B. B., Levental, K. R., Simons, K. & Levental, I. Membrane raft association is a determinant of plasma membrane localization. *Proc. Natl. Acad. Sci. U. S. A.* **111,** 8500–8505 (2014).

55. Kabouridis, P. S., Janzen, J., Magee, A. L. & Ley, S. C. Cholesterol depletion disrupts lipid rafts and modulates the activity of multiple signaling pathways in T lymphocytes. *Eur. J. Immunol.* **30,** 954–963 (2000).

56. Hao, M., Mukherjee, S. & Maxfield, F. R. Cholesterol depletion induces large scale domain segregation in living cell membranes. *Proc. Natl. Acad. Sci. U. S. A.* **98,** 13072–13077 (2001).

57. Zidovetzki, R. & Levitan, I. Use of cyclodextrins to manipulate plasma membrane cholesterol content: Evidence, misconceptions and control strategies. *Biochim. Biophys. Acta - Biomembr.* **1768,** 1311–1324 (2007).

58. Asano, S. *et al.* Regulation of Cell Migration by Sphingomyelin Synthases: Sphingomyelin in Lipid Rafts Decreases Responsiveness to Signaling by the CXCL12/CXCR4 Pathway. *Mol. Cell. Biol.* **32,** 3242–3252 (2012).

59. Sonnleitner, A., Schütz, G. J. & Schmidt, T. Free Brownian Motion of Individual Lipid Molecules in Biomembranes. *Biophys. J.* **77,** 2638–2642 (1999).

60. Head, B. P., Patel, H. H. & Insel, P. A. Interaction of membrane/lipid rafts with the cytoskeleton: Impact on signaling and function: Membrane/lipid rafts, mediators of cytoskeletal arrangement and cell signaling. *Biochim. Biophys. Acta - Biomembr.* **1838,** 532–545 (2014).

61. Levitan, I. & Gooch, K. J. Lipid rafts in membrane-cytoskeleton interactions and control of cellular biomechanics: actions of oxLDL. *Antioxid. Redox Signal.* **9,** 1519–1534 (2007).

62. Kok, J. W., Klappe, K. & Hummel, I. The role of the actin cytoskeleton and lipid rafts in the localization and function of the ABCC1 transporter. *Adv. Biol.* **2014,** DOI: 10.1155/2014/105898 (2014).

63. Ritchie, K., Iino, R., Fujiwara, T., Murase, K. & Kusumi, A. The fence and picket structure of the plasma membrane of live cells as revealed by single molecule techniques (Review). *Mol. Membr. Biol.* **20,** 13–18 (2003).

64. Iino, R., Koyama, I. & Kusumi, A. Single molecule imaging of green fluorescent proteins in living cells: E-cadherin forms oligomers on the free cell surface. *Biophys. J.* **80,** 2667–2677 (2001).

65. Weigel, A. V., Simon, B., Tamkun, M. M. & Krapf, D. Ergodic and nonergodic processes coexist in the plasma membrane as observed by single-molecule tracking. *Proc. Natl. Acad. Sci. U. S. A.* **108,** 6438–6443 (2011).

66. Türkcan, S., Richly, M. U., Alexandrou, A. & Masson, J. B. Probing Membrane Protein Interactions with Their Lipid Raft Environment Using Single-Molecule Tracking and Bayesian Inference Analysis. *PLoS One* **8,** e53073 (2013).

67. Douglass, A. D. & Vale, R. D. Single-molecule microscopy reveals plasma membrane microdomains created by protein-protein networks that exclude or trap signaling molecules in T cells. *Cell* **121,** 937–950 (2005).

68. Magenau, A. *et al*. Discreet and distinct clustering of five model membrane proteins revealed by single molecule localization microscopy. *Mol Membr Biol* 1–8 (2015). doi:10.3109/09687688.2014.990997

69. Shi, Y. Review a glimpse of structural biology through X-Ray crystallography. *Cell* **159,** 995–1014 (2014).

70. Cherezov, V. *et al*. High resolution crystal structure of an engineered human beta2-adrenergic G protein-coupled receptor. *Science (80-.).* **318,** 1258–1265 (2007).

71. Hanson, M. A. *et al*. A specific cholesterol binding site is established by the 2.8 Å structure of the human β2 -adrenergic receptor in an alternate crystal form. *Structure* **16,** 897–905 (2009).

72. Caffrey, M., Li, D. & Dukkipati, A. Membrane protein structure determination using crystallography and lipidic mesophases: Recent advances and successes. *Biochemistry* **51,** 6266–6288 (2012).

73. Caffrey, M. A comprehensive review of the lipid cubic phase or in meso method for crystallizing membrane and soluble proteins and complexes. *Acta Crystallogr. Sect. F Struct. Biol. Commun.* **71,** 3–18 (2015).

74. Wisedchaisri, G., Reichow, S. L. & Gonen, T. Advances in structural and functional analysis of membrane proteins by electron crystallography. *Structure* **19,** 1381–1393 (2011).

75. Gonen, T. *et al*. Lipid-protein interactions in double-layered two-dimensional AQPO crystals. *Nature* **438,** 633–638 (2005).

76. Kowal, J. *et al*. Ligand-induced structural changes in the cyclic nucleotide-modulated potassium channel MloK1. *Nat. Commun.* **5,** (2014).

77. Levy, D., Chami, M. & Rigaud, J. L. Two-dimensional crystallization of membrane proteins: The lipid layer strategy. *FEBS Lett.* **504,** 187–193 (2001).

78. Berman, H. M. *et al*. The Protein Data Bank. *Nucleic Acids Res.* **28,** 235–242 (2000).

79. Tycko, R. BIOMOLECULAR SOLID STATE NMR : Advances in Structural Methodology and Applications to Peptide and Protein Fibrils 1. *Annu. Rev. Phys. Chem.* **52,** 575–606 (2001).

80. Huster, D. Solid-state NMR spectroscopy to study protein-lipid interactions. *Biochim. Biophys. Acta* **1841,** 1146–1160 (2014).

81. Valiyaveetil, F. I., Zhou, Y. & MacKinnon, R. Lipids in the structure, folding, and function of the KcsA K+ channel. *Biochemistry* **41,** 10771–10777 (2002).

82. East, J. M., Melville, D. & Lee, A. G. Exchange rates and numbers of annular lipids for the calcium and magnesium ion dependent adenosinetriphosphatase. *Biochemistry* **24,** 2615–2623 (1985).

83. Smith, A. W. Lipid-protein interactions in biological membranes: a dynamic perspective. *Biochim. Biophys. Acta* **1818,** 172–177 (2012).

84. Marsh, D. Protein modulation of lipids, and vice-versa, in membranes. *Biochim. Biophys. Acta - Biomembr.* **1778,** 1545–1575 (2008).

85. Shaul, M. Mutidimensional femtosecond correlation spectroscopies of electronic and vibrational excitations. *Annu. Rev. Phys. Chem.* **51,** 691–729 (2000).

86. Mukherjee, P., Kass, I., Arkin, I. T. & Zanni, M. T. Picosecond dynamics of a membrane protein revealed by 2D IR. *Proc. Natl. Acad. Sci. U. S. A.* **103,** 3528–3533 (2006).

87. Volkov, V. V., Chelli, R., Muniz-Miranda, F. & Righini, R. Structural properties of a membrane associated anchor dipeptide. *J. Phys. Chem. B* **115,** 5294–5303 (2011).

88. Leser, G. P. & Lamb, R. a. Influenza virus assembly and budding in raft-derived microdomains: A quantitative analysis of the surface distribution of HA, NA and M2 proteins. *Virology* **342,** 215–227 (2005).

89. Hong, M. & DeGrado, W. F. Structural basis for proton conduction and inhibition by the influenza M2 protein. *Nature* **451,** 596–599 (2008).

90. Schnell, J. R. & Chou, J. J. Structure and Mechanism of the M2 Proton Channel of Influenza A Virus. *Nature* **451,** 591–595 (2008).

91. Rossman, J. S. *et al*. Influenza virus m2 ion channel protein is necessary for filamentous virion formation. *J. Virol.* **84,** 5078–5088 (2010).

92. Popot, J.-L. Amphipols, nanodiscs, and fluorinated surfactants: three nonconventional approaches to studying membrane proteins in aqueous solutions. *Annu. Rev. Biochem.* **79,** 737–775 (2010).

93. Merkle, D., Kahya, N. & Schwille, P. Reconstitution and anchoring of cytoskeleton inside giant unilamellar vesicles. *Chembiochem* **9,** 2673–2681 (2008).

94. Sezgin, E. *et al*. Elucidating membrane structure and protein behavior using giant plasma membrane vesicles. *Nature Protocols* **7,** 1042–1051 (2012).

95. Baumgart, T. *et al*. Large-scale fluid / fluid phase separation of proteins and lipids in giant plasma membrane vesicle. *Proc. Natl. Acad. Sci. U. S. A.* **104,** 3165–3170 (2007).

96. Sezgin, E. *et al*. Partitioning, diffusion, and ligand binding of raft lipid analogs in model and cellular plasma membranes. *Biochim. Biophys. Acta - Biomembr.* **1818,** 1777–1784 (2012).

97. Veatch, S. L. & Keller, S. L. Separation of liquid phases in giant vesicles of ternary mixtures of phospholipids and cholesterol. *Biophys. J.* **85,** 3074–3083 (2003).

98. Veatch, S. L. & Keller, S. L. Miscibility phase diagrams of giant vesicles containing sphingomyelin. *Phys. Rev. Lett.* **94,** 3–6 (2005).

99. Štefl, M. *et al*. Dynamics and size of cross-linking-induced lipid nanodomains in model membranes. *Biophys. J.* **102,** 2104–2113 (2012).

100. Keyes, T. *et al*. The lateral diffusion and fibrinogen induced clustering of platelet integrin αIIbβ3 reconstituted into physiologically mimetic GUVs. *Integr. Biol.* **7,** 402–411 (2015).

101. Hammond, A. T. *et al*. Crosslinking a lipid raft component triggers liquid ordered-liquid disordered phase separation in model plasma membranes. *Proc. Natl. Acad. Sci. U. S. A.* **102,** 6320–6325 (2005).

102. Veatch, S. L. *et al*. Critical fluctuations in plasma membrane vesicles. *ACS Chem. Biol.* **3,** 287–293 (2008).

103. Levental, I., Grzybek, M. & Simons, K. Raft domains of variable properties and compositions in plasma membrane vesicles. *Proc. Natl. Acad. Sci. U. S. A.* **108,** 11411–11416 (2011).

104. Girard, P. *et al*. A new method for the reconstitution of membrane proteins into giant unilamellar vesicles. *Biophys. J.* **87,** 419–429 (2004).

105. Rigaud, J. & Lévy, D. Reconstitution of membrane proteins into liposomes. *Methods Enzymol.* **372,** 65–86 (2003).

106. Kreir, M., Farre, C., Beckler, M., George, M. & Fertig, N. Rapid screening of membrane protein activity: electrophysiological analysis of OmpF reconstituted in proteoliposomes. *Lab Chip* **8,** 587–595 (2008).

107. Aimon, S. *et al*. Functional reconstitution of a voltage-gated potassium channel in giant unilamellar vesicles. *PLoS One* **6,** e25529 (2011).

108. Garten, M., Aimon, S., Bassereau, P. & Toombes, G. E. S. Reconstitution of a transmembrane protein, the voltage-gated ion channel, KvAP, into giant unilamellar vesicles for microscopy and patch clamp studies. *J. Vis. Exp.* **95,** e52281 (2015).

109. Kalvodova, L. *et al*. Lipids as modulators of proteolytic activity of BACE: Involvement of cholesterol, glycosphingolipids, and anionic phospholipids in vitro. *J. Biol. Chem.* **280,** 36815–36823 (2005).

110. Cordy, J. M., Hussain, I., Dingwall, C., Hooper, N. M. & Turner, A. J. Exclusively targeting beta-secretase to lipid rafts by GPI-anchor addition up-regulates beta-site processing of the amyloid precursor protein. *Proc. Natl. Acad. Sci. U. S. A.* **100,** 11735–11740 (2003).

111. Sesana, S. *et al*. Membrane features and activity of GPI-anchored enzymes: alkaline phosphatase reconstituted in model membranes. *Biochemistry* **47,** 5433–5440 (2008).

112. Saslowsky, D. E. *et al*. Placental Alkaline Phosphatase Is Efficiently Targeted to Rafts in Supported Lipid Bilayers *. *J. Biol. Chem.* **277,** 26966–26970 (2002).

113. Diaz, O. *et al*. Disruption of lipid rafts stimulates phospholipase d activity in human lymphocytes: implication in the regulation of immune function. *J. Immunol.* **175,** 8077–8086 (2005).

114. Richter, R., Bérat, R. & Brisson, A. Formation of solid-supported lipid bilayers: an integrated view. *Langmuir* **22,** 3497–3505 (2006).

115. Tamm, L. & McConnell, H. Supported phospholipid bilayers. *Biophys. J.* **47,** 105–113 (1985).

116. Watts, T., Gaub, H. & McConnell, H. T-cell-mediated association of peptide antigen and major histocompatibility complex protein detected by energy transfer in an evanescent wave-field. *Nature* **320,** 179–181 (1986).

117. Chiantia, S., Ries, J., Kahya, N. & Schwille, P. Combined AFM and two-focus SFCS study of raft-exhibiting model membranes. *Chemphyschem* **7,** 2409–2418 (2006).

118. Cho, N.-J., Frank, C. W., Kasemo, B. & Höök, F. Quartz crystal microbalance with dissipation monitoring of supported lipid bilayers on various substrates. *Nat. Protoc.* **5,** 1096–106 (2010).

119. Kaufmann, S. *et al*. Supported lipopolysaccharide bilayers. *Langmuir* **28,** 12199–208 (2012).

120. Terrettaz, S., Stora, T., Duschl, C. & Vogel, H. Protein binding to supported lipid membranes: investigation of the cholera toxin-ganglioside interaction by simultaneous impedance spectroscopy and surface plasmon resonance. *Langmuir* **9,** 1361–1369 (1993).

121. Im, H., Wittenberg, N. J., Lesuffleur, A., Lindquist, N. C. & Oh, S.-H. Membrane protein biosensing with plasmonic nanopore arrays and pore-spanning lipid membranes. *Chem. Sci.* **1,** 688 (2010).

122. Dahlin, A. B., Wittenberg, N. J., Höök, F. & Oh, S.-H. Promises and challenges of nanoplasmonic devices for refractometric biosensing. *Nanophotonics* **2,** 83–101 (2013).

123. Evans, E. & Sackmann, E. Translational and rotational drag coefficients for a disk moving in a liquid membrane associated with a rigid substrate. *J. Fluid Mech.* **194,** 553–561 (1988).

124. Camley, B. A. & Brown, F. L. H. Contributions to membrane-embedded-protein diffusion beyond hydrodynamic theories. *Phys. Rev. E - Stat. Nonlinear, Soft Matter Phys.* **85,** 06192 (2012).

125. Deverall, M. A. *et al.* Membrane lateral mobility obstructed by polymer-tethered lipids studied at the single molecule level. *Biophys. J.* **88,** 1875–1886 (2005).

126. König, B., Krueger, S., Orts, W. & Majkrzak, C. Neutron reflectivity and atomic force microscopy studies of a lipid bilayer in water adsorbed to the surface of a silicon single crystal. *Langmuir* **12,** 1343–1350 (1996).

127. Nam, H.-J., Han, S. K., Bowie, J. U. & Kim, S. Rampant exchange of the structure and function of extramembrane domains between membrane and water soluble proteins. *PLoS Comput. Biol.* **9,** e1002997 (2013).

128. Martinez, K. L. K., Meyer, B. B. H., Hovius, R., Lundstrom, K. & Vogel, H. Ligand binding to G protein-coupled receptors in tethered cell membranes. *Langmuir* **19,** 10925–10929 (2003).

129. Tanaka, M. & Sackmann, E. Polymer-supported membranes as models of the cell surface. *Nature* **437,** 656–663 (2005).

130. Wagner, M. L. & Tamm, L. K. Tethered polymer-supported planar lipid bilayers for reconstitution of integral membrane proteins: silane-polyethyleneglycol-lipid as a cushion and covalent linker. *Biophys. J.* **79,** 1400–1414 (2000).

131. Goennenwein, S., Tanaka, M. & Hu, B. Functional incorporation of integrins into solid supported membranes on ultrathin films of cellulose: impact on adhesion. *Biophys. J.* **85,** 646–655 (2003).

132. Poudel, K. R., Keller, D. J. & Brozik, J. a. Single particle tracking reveals corralling of a transmembrane protein in a double-cushioned lipid bilayer assembly. *Langmuir* **27,** 320–327 (2011).

133. Cremer, P. S., Daniel, S., Albertorio, F. & Diaz, A. J. Double cushions preserve transmembrane protein mobility in supported bilayer systems. *Langmuir* **24,** 6820–6826 (2008).

134. Kaufmann, S., Papastavrou, G., Kumar, K., Textor, M. & Reimhult, E. A detailed investigation of the formation kinetics and layer structure of poly(ethylene glycol) tether supported lipid bilayers(1) Kaufmann, S.; Papastavrou, G.; Kumar, K.; Textor, M.; Reimhult, E. Soft Matter 2009, 5, 2804. *Soft Matter* **5,** 2804 (2009).

135. Ye, Q., Konradi, R., Textor, M. & Reimhult, E. Liposomes tethered to omega-functional PEG brushes and induced formation of PEG brush supported planar lipid bilayers. *Langmuir* **25,** 13534–13539 (2009).

136. Kaufmann, S., Borisov, O., Textor, M. & Reimhult, E. Mechanical properties of mushroom and brush poly(ethylene glycol)-phospholipid membranes. *Soft Matter* **7,** 9267 (2011).

137. Kenworthy, A. K., Hristova, K., Needham, D. & McIntosh, T. J. Range and magnitude of the steric pressure between bilayers containing phospholipids with covalently attached poly(ethylene glycol). *Biophys. J.* **68,** 1921–1936 (1995).

138. De Gennes, P. G. *Scaling Concepts in Polymer Physics*. (Cornell University Press, 1979).

139. Watkins, E. B. *et al*. Structure and thermodynamics of lipid bilayers on polyethylene glycol cushions: Fact and fiction of PEG cushioned membranes. *Langmuir* **27,** 13618–13628 (2011).

140. Albertorio, F., Daniel, S. & Cremer, P. S. Supported lipopolymer membranes as nanoscale filters: Simultaneous protein recognition and size-selection assays. *J. Am. Chem. Soc.* **128,** 7168–7169 (2006).

141. Klibanov, A. L., Maruyama, K., Beckerleg, A. M., Torchilin, V. P. & Huang, L. Activity of amphipathic poly(ethylene glycol) 5000 to prolong the circulation time of liposomes depends on the liposome size and is unfavorable for immunoliposome binding to target. *Biochim. Biophys. Acta* **1062,** 142–148 (1991).

142. Burridge, K. A., Figa, M. A. & Wong, J. Y. Patterning adjacent supported lipid bilayers of desired composition to investigate receptor-ligand binding under shear flow. *Langmuir* **20,** 10252–10259 (2004).

143. Ziemba, B. P. & Falke, J. J. Lateral diffusion of peripheral membrane proteins on supported lipid bilayers is controlled by the additive frictional drags of (1) bound lipids

and (2) protein domains penetrating into the bilayer hydrocarbon core. *Chem. Phys. Lipids* **172-173,** 67–77 (2013).

144. Casuso, I. *et al*. Characterization of the motion of membrane proteins using high-speed atomic force microscopy. *Nat. Nanotechnol*. **7,** 525–529 (2012).

145. Fidorra, M., Garcia, A., Ipsen, J. H., Härtel, S. & Bagatolli, L. A. Lipid domains in giant unilamellar vesicles and their correspondence with equilibrium thermodynamic phases: A quantitative fluorescence microscopy imaging approach. *Biochim. Biophys. Acta - Biomembr*. **1788,** 2142–2149 (2009).

146. Crane, J. M. & Tamm, L. K. Role of cholesterol in the formation and nature of lipid rafts in planar and spherical model membranes. *Biophys. J*. **86,** 2965–2979 (2004).

147. Lin, W.-C., Blanchette, C. D., Ratto, T. V & Longo, M. L. Lipid asymmetry in DLPC/DSPC-supported lipid bilayers: a combined AFM and fluorescence microscopy study. *Biophys. J*. **90,** 228–237 (2006).

148. Morales-Penningston, N. F. *et al*. GUV preparation and imaging: Minimizing artifacts. *Biochim. Biophys. Acta - Biomembr*. **1798,** 1324–1332 (2010).

149. Orth, R., Wu, M., Holowka, D., Craighead, H. & Baird, B. Mast cell activation on patterned lipid bilayers of subcellular dimensions. *Langmuir* **19,** 1599–1605 (2003).

150. Dustin, M. & Bromley, S. Antigen receptor engagement delivers a stop signal to migrating T lymphocytes. *Proc. Natl. Acad. Sci. U. S. A*. **94,** 3909–3913 (1997).

151. Spycher, P. R., Hall, H., Vogel, V. & Reimhult, E. Patterning of supported lipid bilayers and proteins using material selective nitrodopamine-mPEG. *Biomater. Sci*. **3,** 94–102 (2015).

152. Majd, S. & Mayer, M. Hydrogel stamping of arrays of supported lipid bilayers with various lipid compositions for the screening of drug-membrane and protein-membrane interactions. *Angew. Chem. Int. Ed. Engl*. **44,** 6697–700 (2005).

153. Kung, L. A., Kam, L., Hovis, J. S. & Boxer, S. G. Patterning hybrid surfaces of proteins and supported lipid bilayers. *Langmuir* **16,** 6773–6776 (2000).

154. Boxer, S. Molecular transport and organization in supported lipid membranes. *Curr. Opin. Chem. Biol*. **4,** 704–709 (2000).

155. Ilic, B. & Craighead, H. Topographical patterning of chemically sensitive biological materials using a polymer-based dry lift off. *Biomed. Microdevices* 317–322 (2000).

156. Moran-Mirabal, J. M. *et al*. Micrometer-sized supported lipid bilayer arrays for bacterial toxin binding studies through total internal reflection fluorescence microscopy. *Biophys. J.* **89,** 296–305 (2005).

157. Chao, L. & Daniel, S. Measuring the partitioning kinetics of membrane biomolecules using patterned two-phase coexistant lipid bilayers. *J. Am. Chem. Soc.* **133,** 15635–15643 (2011).

158. Kam, L. & Boxer, S. G. Formation of supported lipid bilayer composition arrays by controlled mixing and surface capture. *J. Am. Chem. Soc.* **122,** 12901–12902 (2000).

159. Kraft, M. L. *et al*. Quantitative analysis of supported membrane composition using the NanoSIMS. *Appl. Surf. Sci.* **252,** 6950–6956 (2006).

160. Munro, S. Lipid rafts: elusive or illusive? *Cell* **115,** 377–388 (2003).

161. Kiessling, V., Crane, J. M. & Tamm, L. K. Transbilayer effects of raft-like lipid domains in asymmetric planar bilayers measured by single molecule tracking. *Biophys. J.* **91,** 3313–26 (2006).

162. Devaux, P. F. & Morris, R. Transmembrane asymmetry and lateral domains in biological membranes. *Traffic* **5,** 241–246 (2004).

163. Feng, Z. V., Spurlin, T. A. & Gewirth, A. A. Direct visualization of asymmetric behavior in supported lipid bilayers at the gel-fluid phase transition. *Biophys. J.* **88,** 2154–2164 (2005).

164. Garg, S., Rühe, J., Lüdtke, K., Jordan, R. & Naumann, C. A. Domain registration in raft-mimicking lipid mixtures studied using polymer-tethered lipid bilayers. *Biophys. J.* **92,** 1263–1270 (2007).

165. Hussain, N. F., Siegel, A. P., Ge, Y., Jordan, R. & Naumann, C. a. Bilayer asymmetry influences integrin sequestering in raft-mimicking lipid mixtures. *Biophys. J.* **104,** 2212–2221 (2013).

166. Anglin, T. C., Liu, J. & Conboy, J. C. Facile lipid flip-flop in a phospholipid bilayer induced by gramicidin A measured by sum-frequency vibrational spectroscopy. *Biophys. J.* **92,** L01–L03 (2007).

167. Gurtovenko, A. A. & Vattulainen, I. Molecular mechanism for lipid flip-flops. *J. Phys. Chem. B* **111,** 13554–13559 (2007).

168. Liu, J. & Conboy, J. C. Direct measurement of the transbilayer movement of phospholipids by sum-frequency vibrational spectroscopy. *J. Am. Chem. Soc.* **126,** 8376–8377 (2004).

169. Subramaniam, A. B., Guidotti, G., Manoharan, V. N. & Stone, H. a. Glycans pattern the phase behaviour of lipid membranes. *Nat. Mater.* **12,** 128–33 (2013).

170. Hsia, C.-Y., Richards, M. J. & Daniel, S. A review of traditional and emerging methods to characterize lipid–protein interactions in biological membranes. *Anal. Methods* **7,** 7076–7094 (2015).

171. Loll, P. J. Membrane protein structural biology: the high throughput challenge. *J. Struct. Biol.* **142,** 144–153 (2003).

172. Sachs, J. N. & Engelman, D. M. Introduction to the membrane protein reviews: the interplay of structure, dynamics, and environment in membrane protein function. *Annu. Rev. Biochem.* **75,** 707–712 (2006).

173. Sprenger, R. R. & Horrevoets, A. J. G. The ins and outs of lipid domain proteomics. *Proteomics* **7,** 2895–903 (2007).

174. Zheng, Y. Z. & Foster, L. J. Biochemical and proteomic approaches for the study of membrane microdomains. *Journal of Proteomics* **72,** 12–22 (2009).

175. Joshi, M. K., Dracheva, S., Mukhopadhyay, A. K., Bose, S. & Hendler, R. W. Importance of specific native lipids in controlling the photocycle of bacteriorhodopsin. *Biochemistry* **37,** 14463–14470 (1998).

176. Carlson, R. O., Masco, D., Brooker, G. & Spiegel, S. Endogenous ganglioside GM1 modulates L-type calcium channel activity in N18 neuroblastoma cells. *J. Neurosci.* **14,** 2272–2281 (1994).

177. Daniel, S. *et al.* Separation of membrane-bound compounds by solid-supported bilayer electrophoresis. *J. Am. Chem. Soc.* **129,** 8072–8073 (2007).

178. Weng, K. C., Kanter, J. L., Robinson, W. H. & Frank, C. W. Fluid supported lipid bilayers containing monosialoganglioside GM1: A QCM-D and FRAP study. *Colloids Surfaces B Biointerfaces* **50,** 76–84 (2006).

179. Groves, J. T. & Dustin, M. L. Supported planar bilayers in studies on immune cell adhesion and communication. *Journal of Immunological Methods* **278,** 19–32 (2003).

180. Sumino, A. *et al.* Selective assembly of photosynthetic antenna proteins into a domain-structured lipid bilayer for the construction of artificial photosynthetic antenna systems: Structural analysis of the assembly using surface plasmon resonance and atomic force microscopy. *Langmuir* **27,** 1092–1099 (2011).

181. Burns, A. R., Frankel, D. J. & Buranda, T. Local mobility in lipid domains of supported bilayers characterized by atomic force microscopy and fluorescence correlation spectroscopy. *Biophys. J.* **89,** 1081–1093 (2005).

182. Shreve, A. P., Howland, M. C., Sapuri-Butti, A. R., Allen, T. W. & Parikh, A. N. Evidence for leaflet-dependent redistribution of charged molecules in fluid supported phospholipid bilayers. *Langmuir* **24,** 13250–13253 (2008).

183. Richter, R. P. & Brisson, A. R. Following the formation of supported lipid bilayers on mica: a study combining AFM, QCM-D, and ellipsometry. *Biophys. J.* **88,** 3422–33 (2005).

184. Tokumasu, F., Jin, A. J., Feigenson, G. W. & Dvorak, J. A. Nanoscopic lipid domain dynamics revealed by atomic force microscopy. *Biophys. J.* **84,** 2609–2618 (2003).

185. Cheetham, M. R. *et al*. Concentrating membrane proteins using asymmetric traps and AC electric fields. *J. Am. Chem. Soc.* **133,** 6521–6524 (2011).

186. Cremer, P. S., Groves, J. T., Kung, L. A. & Boxer, S. G. Writing and erasing barriers to lateral mobility into fluid phospholipid bilayers. *Langmuir* **15,** 3893–3896 (1999).

187. Stelzle, M., Miehlich, R. & Sackmann, E. Two-dimensional microelectrophoresis in supported lipid bilayers. *Biophys. J.* **63,** 1346–1354 (1992).

188. Van Oudenaarden, A. & Boxer, S. G. Brownian ratchets: molecular separations in lipid bilayers supported on patterned arrays. *Science* **285,** 1046–1048 (1999).

189. Nabika, H., Takimoto, B. & Murakoshi, K. Molecular separation in the lipid bilayer medium: Electrophoretic and self-spreading approaches. *Analytical and Bioanalytical Chemistry* **391,** 2497–2506 (2008).

190. Jönsson, P., Beech, J. P., Tegenfeldt, J. O. & Höök, F. Shear-driven motion of supported lipid bilayers in microfluidic channels. *J. Am. Chem. Soc.* **131,** 5294–5297 (2009).

191. Jönsson, P., Gunnarsson, A. & Höök, F. Accumulation and separation of membrane-bound proteins using hydrodynamic forces. *Anal. Chem.* **83,** 604–11 (2011).

192. Paulick, M. & Bertozzi, C. The Glycosylphosphatidylinositol Anchor: A Complex Membrane-Anchoring Structure for Proteins†. *Biochemistry* 6991–7000 (2008).

193. Veatch, S. L., Gawrisch, K. & Keller, S. L. Closed-loop miscibility gap and quantitative tie-lines in ternary membranes containing diphytanoyl PC. *Biophys. J.* **90,** 4428–4436 (2006).

194. Veatch, S. L., Polozov, I. V, Gawrisch, K. & Keller, S. L. Liquid domains in vesicles investigated by NMR and fluorescence microscopy. *Biophys. J.* **86,** 2910–2922 (2004).

195. Ionova, I. V., Livshits, V. A. & Marsh, D. Phase diagram of ternary cholesterol/palmitoylsphingomyelin/ palmitoyloleoyl-phosphatidylcholine mixtures: Spin-label EPR study of lipid-raft formation. *Biophys. J.* **102,** 1856–1865 (2012).

196. Jönsson, P. & Höök, F. Effects of surface pressure and internal friction on the dynamics of shear-driven supported lipid bilayers. *Langmuir* **27,** 1430–1439 (2011).

197. Granéli, A., Rydström, J., Kasemo, B. & Höök, F. Formation of supported lipid bilayer membranes on SiO2 from proteoliposomes containing transmembrane proteins. *Langmuir* 842–850 (2003).

198. Soumpasis, D. M. Theoretical analysis of fluorescence photobleaching recovery experiments. *Biophys. J.* **41,** 95–97 (1983).

199. Axelrod, D., Koppel, D. E., Schlessinger, J., Elson, E. & Webb, W. W. Mobility measurement by analysis of fluorescence photobleaching recovery kinetics. *Biophys. J.* **16,** 1055–1069 (1976).

200. Jonsson, P., Beech, J. P., Tegenfeldt, J. O. & Hook, F. Mechanical Behavior of a Supported Lipid Bilayer under External Shear Forces. *Langmuir* **25,** 6279–6286 (2009).

201. Merkel, R., Sackmann, E. & Evans, E. Molecular friction and epitactic coupling between monolayers in supported bilayers. *Journal de Physique* **50,** 1535–1555 (1989).

202. Simonsson, L., Gunnarsson, A., Wallin, P., Jönsson, P. & Höök, F. Continuous lipid bilayers derived from cell membranes for spatial molecular manipulation. *J. Am. Chem. Soc.* **133,** 14027–14032 (2011).

203. Tanaka, M., Rossetti, F. F. & Kaufmann, S. Native supported membranes: creation of two-dimensional cell membranes on polymer supports (Review). *Biointerphases* **3,** FA12–FA16 (2008).

204. Costello, D. A., Millet, J. K., Hsia, C.-Y. Y., Whittaker, G. R. & Daniel, S. Single particle assay of coronavirus membrane fusion with proteinaceous receptor-embedded supported bilayers. *Biomaterials* **34,** 7895–904 (2013).

205. Wong, W. & Schlichter, L. C. Differential Recruitment of Kv1.4 and Kv4.2 to Lipid Rafts by PSD-95. *J. Biol. Chem.* **279,** 444–452 (2004).

206. Chao, L., Richards, M. J., Hsia, C.-Y. Y. & Daniel, S. Two-dimensional continuous extraction in multiphase lipid bilayers to separate, enrich, and sort membrane-bound species. *Anal. Chem.* **85,** 6696–6702 (2013).

207. Castellana, E. T. & Cremer, P. S. Solid supported lipid bilayers: From biophysical studies to sensor design. *Surf. Sci. Rep.* **61,** 429–444 (2006).

208. Matkó, J. & Szöllősi, J. Regulatory aspects of membrane microdomain (raft) dynamics in live cells. *Membr. Microdomain Signal.* 15–46 (2005).

209. Chan, Y.-H. M. & Boxer, S. G. Model membrane systems and their applications. *Curr. Opin. Chem. Biol.* **11,** 581–587 (2007).

210. Cho, N.-J., Frank, C. W., Kasemo, B. & Höök, F. Quartz crystal microbalance with dissipation monitoring of supported lipid bilayers on various substrates. *Nat. Protoc.* **5,** 1096–1106 (2010).

211. Tan, S., Tan, H. T. & Chung, M. C. M. Membrane proteins and membrane proteomics. *Proteomics* **8,** 3924–32 (2008).

212. Cordwell, S. J. & Thingholm, T. E. Technologies for plasma membrane proteomics. *Proteomics* **10,** 611–27 (2010).

213. Simeonov, P., Werner, S., Haupt, C., Tanabe, M. & Bacia, K. Membrane protein reconstitution into liposomes guided by dual-color fluorescence cross-correlation spectroscopy. *Biophys. Chem.* **184,** 37–43 (2013).

214. Helenius, A. R. I. & Simons, K. A. I. Solubilization of Membranes by Detergents. *Biochim. Biophys. Acta* **415,** 29–79 (1975).

215. Erb, E. M. & Engel, J. Reconstitution of functional integrin into phospholipid vesicles and planar lipid bilayers. *Methods Mol. Biol.* **139,** 71–82 (2000).

216. Pace, H. P. *et al.* Preserved Transmembrane Protein Mobility in Polymer-Supported Lipid Bilayers Derived from Cell Membranes. *Anal. Chem.* 150813052141007 (2015). doi:10.1021/acs.analchem.5b01449

217. Dogterom, M. & Koenderink, G. Cell-membrane mechanics: Vesicles in and tubes out. *Nat. Mater.* **10,** 561–562 (2011).

218. Holowka, D. & Baird, B. Structural studies on the membrane-bound immunoglobulin E-receptor complex. 1. Characterization of large plasma membrane vesicles from rat basophilic leukemia. *Biochemistry* 3466–3474 (1983).

219. Costello, D. A., Hsia, C.-Y. Y., Millet, J. K., Porri, T. & Daniel, S. Membrane fusion-competent virus-like proteoliposomes and proteinaceous supported bilayers made directly from cell plasma membranes. *Langmuir* **29,** 6409–6419 (2013).

220. Sharom, F. J. & Lehto, M. T. Glycosylphosphatidylinositol-anchored proteins: structure, function, and cleavage by phosphatidylinositol-specific phospholipase C. *Biochem. Cell Biol.* **80,** 535–549 (2002).

221. Li, M. *et al.* Mesothelin is a malignant factor and therapeutic vaccine target for pancreatic cancer. *Mol. Cancer Ther.* **7,** 286–296 (2008).

222. Khakh, B. S. & North, R. A. P2X receptors as cell-surface ATP sensors in health and disease. *Nature* **442,** 527–532 (2006).

223. North, R. A. Molecular physiology of P2X receptors. *Physiol. Rev.* **82,** 1013–67. (2002).

224. Fuhrmans, M. & Müller, M. Mechanisms of vesicle spreading on surfaces: coarse-grained simulations. *Langmuir* (2013).

225. Kawate, T., Michel, J. C., Birdsong, W. T. & Gouaux, E. Crystal structure of the ATP-gated P2X(4) ion channel in the closed state. *Nature* **460,** 592–598 (2009).

226. Smith, M. B. *et al*. Interactive, computer-assisted tracking of speckle trajectories in fluorescence microscopy: application to actin polymerization and membrane fusion. *Biophys. J.* **101,** 1794–804 (2011).

227. Poudel, K. R., Jones, J. P. & Brozik, J. A. A Guide to Tracking Single Transmembrane Proteins in Supported Lipid Bilayers. **974,** 233–252 (2013).

228. Vrljic, M., Nishimura, S. Y. & Moerner, W. E. Single-molecule tracking. *Methods Mol. Biol.* **398,** 193–219 (2007).

229. Saxton, M. Single-particle tracking: the distribution of diffusion coefficients. *Biophys. J.* **72,** (1997).

230. Ferrari, R., Manfroi, A. J. & Young, W. R. Strongly and weakly self-similar diffusion. *Phys. D Nonlinear Phenom.* **154,** 111–137 (2001).

231. Sbalzarini, I. F. & Koumoutsakos, P. Feature point tracking and trajectory analysis for video imaging in cell biology. *J. Struct. Biol.* **151,** 182–195 (2005).

232. Kaufmann, S., Papastavrou, G., Kumar, K., Textor, M. & Reimhult, E. A detailed investigation of the formation kinetics and layer structure of poly(ethylene glycol) tether supported lipid bilayers. *Soft Matter* **5,** 2804 (2009).

233. Weiß, K. *et al*. Quantifying the diffusion of membrane proteins and peptides in black lipid membranes with 2-focus fluorescence correlation spectroscopy. *Biophys. J.* **105,** 455–462 (2013).

234. Ramadurai, S. *et al*. Lateral diffusion of membrane proteins. *J Am Chem Soc* **131,** 12650–12656 (2009).

235. Zhang, F. *et al*. Lateral diffusion of membrane-spanning and glycosylphosphatidylinositol- linked proteins: toward establishing rules governing the lateral mobility of membrane proteins. *J. Cell Biol.* **115,** 75–84 (1991).

236. Türkcan, S., Richly, M. U., Alexandrou, A. & Masson, J. B. Probing Membrane Protein Interactions with Their Lipid Raft Environment Using Single-Molecule Tracking and Bayesian Inference Analysis. *PLoS One* **8,** e53073 (2013).

237. Foley, M. *et al*. The lateral diffusion of lipid probes in the surface membrane of Schistosoma mansoni. *J. Cell Biol.* **103,** 807–18 (1986).

238. Wang, T., Smith, E. a., Chapman, E. R. & Weisshaar, J. C. Lipid Mixing and Content Release in Single-Vesicle, SNARE-Driven Fusion Assay with 1–5 ms Resolution. *Biophys. J.* **96,** 4122–4131 (2009).

239. Kusumi, A., Sako, Y. & Yamamoto, M. Confined lateral diffusion of membrane receptors as studied by single particle tracking (nanovid microscopy). Effects of calcium-induced differentiation in cultured epithelial cells. *Biophys. J.* **65,** 2021–2040 (1993).

240. Lorenz, H., Hailey, D. W., Wunder, C. & Lippincott-Schwartz, J. The fluorescence protease protection (FPP) assay to determine protein localization and membrane topology. *Nat. Protoc.* **1,** 276–279 (2006).

241. Al-Nedawi, K. *et al*. Intercellular transfer of the oncogenic receptor EGFRvIII by microvesicles derived from tumour cells. *Nat. Cell Biol.* **10,** 619–624 (2008).

242. Antonyak, M. A. *et al*. Cancer cell-derived microvesicles induce transformation by transferring tissue transglutaminase and fibronectin to recipient cells. *Proc Natl Acad Sci U S A* **108,** 4852–4857 (2011).

243. Sengupta, P., Baird, B. & Holowka, D. Lipid rafts, fluid/fluid phase separation, and their relevance to plasma membrane structure and function. *Semin. Cell Dev. Biol.* **18,** 583–590 (2007).

244. Weerasekera, R. *et al*. Interactome and interface protocol (2IP): A novel strategy for high sensitivity topology mapping of protein complexes. *Proteomics* **7,** 3835–3852 (2007).

245. Vasilescu, J., Guo, X. & Kast, J. Identification of protein-protein interactions using in vivo cross-linking and mass spectrometry. *Proteomics* **4,** 3845–3854 (2004).

246. Martinez, K., Meyer, B. & Hovius, R. Ligand binding to G protein-coupled receptors in tethered cell membranes. *Langmuir* 10925–10929 (2003).

247. McCabe, I. & Forstner, M. Polymer supported lipid bilayers. *Open J. Biophys.* **3,** 59–69 (2013).

248. Zijlstra, N., Blum, C., Segers-Nolten, I. M. J., Claessens, M. M. A. E. & Subramaniam, V. Molecular composition of sub-stoichiometrically labeled alpha-synuclein oligomers determined by single-molecule photobleaching. *Angew. Chemie - Int. Ed.* **51,** 8821–8824 (2012).

249. Richards, M. J. *et al*. Membrane protein mobility and orientation preserved in supported bilayers created directly from cell plasma membrane blebs. **32,** 2963–2974 (2016).

250. Nikaido, H. & Vaara, M. Molecular Basis of Bacterial Outer Membrane Permeability. *Microbiol. Rev*. **49,** 1–32 (1985).

251. Silhavy, T. J., Kahne, D. & Walker, S. The bacterial cell envelope. *Cold Spring Harb. Perspect. Biol*. **2,** 1–17 (2010).

252. Smit, J., Kamio, Y. & Nikaido, H. Outer membrane of Salmonella typhimurium: chemical analysis and freeze-fracture studies with lipopolysaccharide mutants. *J. Bacteriol*. **124,** 942–58 (1975).

253. Kamio, Y. & Nikaido, H. Outer membrane of Salmonella typhimurium: accessibility of phospholipid head groups to phospholipase c and cyanogen bromide activated dextran in the external medium. *Biochemistry* **15,** 2561–2570 (1976).

254. Takeuchi, Y. & Nikaido, H. Persistence of segregated phospholipid domains in phospholipid--lipopolysaccharide mixed bilayers: studies with spin-labeled phospholipids. *Biochemistry* **20,** 523–529 (1981).

255. Koebnik, R., Locher, K. P. & Van Gelder, P. Structure and function of bacterial outer membrane proteins: barrels in a nutshell. *Mol. Microbiol*. **37,** 239–253 (2000).

256. Welch, R. A. MicroReview Pore-forming cytolysins of Gram-negative bacteria. **5,** 521–528 (1991).

257. Mangenot, S., Hochrein, M., Rädler, J. & Letellier, L. Real-Time Imaging of DNA Ejection from Single Phage Particles. *Curr. Biol*. **15,** 430–435 (2005).

258. Silver, L. L. Challenges of Antibacterial Discovery. *Clin. Microbiol. Rev*. **24,** 71–109 (2011).

259. Henderson, L. C., Li, J., Nation, R. L., Velkov, T. & Pfeffer, F. M. Developing an anion host for lipid A binding and antibacterial activity. *Chem. Commun. (Camb)*. **46,** 3197–3199 (2010).

260. Brian, A. & McConnell, H. Allogeneic stimulation of cytotoxic T cells by supported planar membranes. *Proc. Natl. Acad. Sci*. **81,** 6159–6163 (1984).

261. McConnell, H. M., Watts, T. H., Weis, R. M. & Brian, A. A. Supported planar membranes in studies of cell-cell recognition in the immune system. *BBA - Rev. Biomembr*. **864,** 95–106 (1986).

262. Sackmann, E. Supported membranes: Scientific and practical applications. *Science (80-.)*. **271,** 43–48 (1996).

263. Thomas, C. J., Surolia, N. & Surolia, A. Surface plasmon resonance studies resolve the enigmatic endotoxin neutralizing activity of polymyxin B. *J. Biol. Chem.* **274,** 29624–29627 (1999).

264. Tong, J. & McIntosh, T. J. Structure of Supported Bilayers Composed of Lipopolysaccharides and Bacterial Phospholipids: Raft Formation and Implications for Bacterial Resistance. *Biophys. J.* **86,** 3759–3771 (2004).

265. Merz, C., Knoll, W., Textor, M. & Reimhult, E. Formation of supported bacterial lipid membrane mimics. *Biointerphases* **3,** FA41 (2008).

266. Lind, T. K. *et al*. Formation and Characterization of Supported Lipid Bilayers Composed of Hydrogenated and Deuterated Escherichia coli Lipids. *PLoS One* **10,** e0144671 (2015).

267. Dodd, C. E. *et al*. Native E. coli inner membrane incorporation in solid-supported lipid bilayer membranes. *Biointerphases* **3,** FA59 (2008).

268. Kulp, A. & Kuehn, M. J. Biological Functions and Biogenesis of Secreted Bacterial Outer Membrane Vesicles. *Annu Rev Microbiol.* **64,** 163–184 (2012).

269. Baker, J. L., Chen, L., Rosenthal, J. A., Putnam, D. & DeLisa, M. P. Microbial biosynthesis of designer outer membrane vesicles. *Curr. Opin. Biotechnol.* **29,** 76–84 (2014).

270. McBroom, A. J. & Kuehn, M. J. Release of outer membrane vesicles by Gram-negative bacteria is a novel envelope stress response. *Mol. Microbiol.* **63,** 545–558 (2007).

271. Gankema, H., Wensink, J. & Witholt, B. Some Characteristics of the Outer Membrane Material Released by Growing Enterotoxigenic Escherichia coli Some Characteristics of the Outer Membrane Material Released by Growing Enterotoxigenic Escherichia coli. **29,** 704–713 (1980).

272. Kato, S., Kowashi, Y. & Demuth, D. R. Outer membrane-like vesicles secreted by Actinobacillus actinomycetemcomitans are enriched in leukotoxin. *Microb. Pathog.* **32,** 1–13 (2002).

273. Kesty, N. C., Mason, K. M., Reedy, M., Miller, S. E. & Kuehn, M. J. Enterotoxigenic Escherichia coli vesicles target toxin delivery into mammalian cells. *EMBO J.* **23,** 4538–4549 (2004).

274. Kobayashi, H., Uematsu, K., Hirayama, H. & Horikoshi, K. Novel toluene elimination system in a toluene-tolerant microorganism. *J. Bacteriol.* **182,** 6451–6455 (2000).

275. Manning, A. J. & Kuehn, M. J. Contribution of bacterial outer membrane vesicles to innate bacterial defense Contribution of bacterial outer membrane vesicles to innate bacterial defense. **258,** 605–619 (2011).

276. Loeb, M. R. Bacteriophage T4-mediated release of envelope components from *Escherichia coli*. *J. Virol.* **13,** 631–41 (1974).

277. Loeb, M. R. & Kilner, J. Release of a special fraction of the outer membrane from both growing and phage T4-infected Escherichia coli B. *BBA - Biomembr.* **514,** 117–127 (1978).

278. Domingues, M. M. *et al*. Biophysical characterization of polymyxin b interaction with LPS aggregates and membrane model systems. *Biopolymers* **98,** 338–344 (2012).

279. Chen, D. J. *et al*. Delivery of foreign antigens by engineered outer membrane vesicle vaccines. *Proc. Natl. Acad. Sci.* **107,** 3099–3104 (2010).

280. Bernadac, A. *et al*. Escherichia coli tol-pal Mutants Form Outer Membrane Vesicles Escherichia coli tol-pal Mutants Form Outer Membrane Vesicles. *J. Bacteriol.* **180,** 4872–4878 (1998).

281. Sauerbrey, G. Verwendung von Schwingquarzen zur Wagungdiinner Schichten und zur Mikrowagung. *Zeitschrift fur Phys.* **155,** 206–222 (1959).

282. Voinova, M. V., Rodahl, M., Jonson, M. & Kasemo, B. Viscoelastic acoustic response of layered polymer films at fluid-solid interfaces: Continuum mechanics approach. **59,** 391–396 (1999).

283. Mechler, A. *et al*. Specific and selective peptide-membrane interactions revealed using quartz crystal microbalance. *Biophys. J.* **93,** 3907–16 (2007).

284. Marsh, D., Bartucci, R. & Sportelli, L. Lipid membranes with grafted polymers: Physicochemical aspects. *Biochim. Biophys. Acta - Biomembr.* **1615,** 33–59 (2003).

285. Kim, J.-Y. *et al*. Engineered bacterial outer membrane vesicles with enhanced functionality. *J. Mol. Biol.* **380,** 51–66 (2008).

286. Cho, N.-J. *et al*. Alpha-helical peptide-induced vesicle rupture revealing new insight into the vesicle fusion process as monitored in situ by quartz crystal microbalance-dissipation and reflectometry. *Anal. Chem.* **81,** 4752–61 (2009).

287. Bingen, P., Wang, G., Steinmetz, N. F., Rodahl, M. & Richter, R. P. Solvation effects in the QCM-D response to biomolecular adsorption - a phenomenological approach. *Anal. Chem.* **80,** 8880–8890 (2008).

288. Cremer, P. S. & Boxer, S. G. Formation and Spreading of Lipid Bilayers on Planar Glass Supports. *J. Phys. Chem. B* **103,** 2554–2559 (1999).

289. Morrison, D. C. & Jacobs, D. M. Binding of polymyxin B to the lipid A portion of bacterial lipopolysaccharides. *Immunochemistry* **13,** 813–818 (1976).

290. Hancock, R. E. W. & Chapple, D. S. Peptide Antibiotics. *Antimicrob. Agents Chemother.* **43,** 1317–1323 (1999).

291. Velkov, T., Thompson, P. E., Nation, R. L. & Li, J. Structure-activity relationships of polymyxin antibiotics. *J. Med. Chem.* **53,** 1898–1916 (2010).

292. Velkov, T., Roberts, K. D., Nation, R. L., Thompson, P. E. & Li, J. Pharmacology of polymyxins: new insights into an 'old' class of antibiotics. *Futur. Microbiol* **8,** 1–20 (2013).

293. Clausell, A. *et al.* Gram-negative outer and inner membrane models: Insertion of cyclic cationic lipopeptides. *J. Phys. Chem. B* **111,** 551–563 (2007).

294. Thomas, C. J., Gangadhar, B. P., Surolia, N. & Surolia, A. Kinetics and mechanism of the recognition of endotoxin by polymyxin B. *J. Am. Chem. Soc.* **120,** 12428–12434 (1998).

295. Thomas, C. J. & Surolia, A. Kinetics of the interaction of endotoxin with polymyxin B and its analogs: A surface plasmon resonance analysis. *FEBS Lett.* **445,** 420–424 (1999).

296. Joshi, T., Voo, Z. X., Graham, B., Spiccia, L. & Martin, L. L. Real-time examination of aminoglycoside activity towards bacterial mimetic membranes using Quartz Crystal Microbalance with Dissipation monitoring (QCM-D). *Biochim. Biophys. Acta* **1848,** 385–391 (2014).

297. Wang, K. F., Nagarajan, R. & Camesano, T. A. Differentiating antimicrobial peptides interacting with lipid bilayer: Molecular signatures derived from quartz crystal microbalance with dissipation monitoring. *Biophys. Chem.* **196C,** 53–67 (2014).

298. Jimison, L. H. *et al.* Measurement of Barrier Tissue Integrity with an Organic Electrochemical Transistor. *Adv. Mater.* **24,** 5919–5923 (2012).

299. Adamczyk, Z., Weroński, P. & Musiał, E. Colloid particle adsorption at random site (heterogeneous) surfaces. *J. Colloid Interface Sci.* **248,** 67–75 (2002).